Delft University of Technology

Faculty of EEMCS & Faculty of Applied Sciences
BSc program Applied Mathematics & Physics

A numerical and experimental study of a reverberation chamber

Author:
Gijs Mast, 4693655

Supervisors:
Dr.ir. M.D. Verweij
Dr. D.J.P. Lahaye

July 10, 2020

Contents

Abstract

This thesis produces a pre-characterization numerical model capable of handling and calculating electromagnetic fields within a rectangular reverberation chamber near its lowest usable frequency at 200 MHz. As reverberation chambers strive to have high electric field uniformity to meet field uniformity standards, high electric fields, having the property of being naturally more uniform, are out of the scope of interest. Additionally high frequencies require more computational memory and CPU time.

The model is made using a finite element method based modelling software called Comsol Multiphysics. The modelled reverberation chamber consisting of an antenna, a reflective shielded chamber and a Z-fold mode-stirrer is gradually build up. This means that first an analysis of only the antennas will be made, thereafter the antennas will be put into a reflective shielded chamber environment and finally the antennas are put into a reflective shielded chamber environment with a z-fold mode stirrer. Furthermore, an extra situation will be considered in which a dielectric object will be added to a shielded chamber environment excited by an antenna without mode stirrer. The effect of an added dielectric object will be studied because of physical interest and completeness and not as added intermediate step to build a reverberation chamber environment. As all situations have similar difficulties in modelling and measuring, the gradual development of the reverberation chamber will allow for the best error analysis of the model. The model replicates the setup of a real reverberation chamber located at Comtest, Zoeterwoude. The reliability and accuracy of the model is studied by comparing the modelled electric field to the measured one. It was found that all models showed a good resemblance between simulated and measured electric fields above 60 MHz except the most complex reverberation chamber model. The simulated field uniformity expressed as standard deviation is twice as high as measurements suggest. The model can therefore only be used as worst-case scenario prediction for the field uniformity.

Two kinds of antennas are used during the modelling and measuring phase, a 3104c biconical antenna used in the frequency range 25-200 MHz and the 3146a log-periodic dipole array antenna in the frequency range 200-1000 MHz. The electromagnetic radiation pattern in the far field domain was modelled and corresponded to the expected omni-directional and directional field pattern respectively.
Next the antennas were placed in a highly reflective shielded chamber with dimensions
(4.05 m $\times$ 2.55 m $\times$ 2.925 m). By taking data in specific slices from the model and comparing these to the measurements at the same points it was concluded that the model does not accurately predict the electric fields below 60 MHz. Above 60 MHz the model does predict the general electric field pattern in the chamber. It however does not predict local maxima or minima of the electric field.
The same comparison was done for the situation in which a dielectric object was added to the setup. The dielectric object was chosen to be a container filled with water
(0.27 m $\times$ 0.565 m $\times$ 0.269 m). This container is placed in the formerly empty shielded chamber to change the inner electric field. Water was used due to its favourable properties for reflectivity. The same behaviour of the model was observed with this added dielectric object.
Finally the electric field in the reverberation chamber at Comtest (5.03 m $\times$ 3.97 m $\times$ 2.85 m) was modelled and solved using a GMRES algorithm with geometric multigrid preconditioning. The preconditioning in the GMRES allows for faster convergence. The field uniformity was computed for both the model and the measurements as outlined by IEC 61000-4-21. This was done for 4 and 12 stirrer rotation positions. Both showed that the model had a less uniform field

compared to the Comtest reverberation chamber. The Comtest reverberation chamber complied with the electromagnetic compatibility requirements for measurements using 12 stirrer positions whereas the model did not. However the 4 stirrer position model, which made use of perfect electric conductor boundary conditions, showed a maximum of 13% increase in field uniformity when steel walls were used instead.

To show a glimpse of an innovation that put the Delft University of Technology on the map, the shifted laplacian preconditioner is briefly discussed. As an intermediate step in solving a problem with little to no damping, a complex preconditioning matrix is used. It is shown that for an increasing imaginary shift in the Helmholtz problem, expressed as an increasing electrical conductivity σ, the number of iterations needed to reach a relative tolerance smaller than 0.01 decreases. At last, the effect of a shifted laplacian contribution to a multigrid preconditioning on the convergence speed is studied for an non-damped pressure acoustic Helmholtz problem. It is shown that the added contribution slows convergence in a simple geometry, while a more complex geometry cannot be solved without this contribution.

1 Introduction

Over the last few years, the use of wireless applications has grown exponentially. New wireless products like charging stations, airpods or cell phones will experience stress from electric fields throughout their lifetime. To guarantee correct operation for these devices there are certain electromagnetic compatibility (emc) requirements that the devices have to meet. As the demand for wireless products has risen, so has the need for accurate and efficient test facilities called reverberation chambers.

Electromagnetic compatibility measurements are done in an environment with uniform electromagnetic behaviour. Reverberation chambers can provide these conditions by incorporating a reflecting mode-stirrer. Due to high reflectance of both the stirrer and the exterior walls, high electric field strengths can be generated as well. To ensure reliable testing of the equipment under test (EUT), the reverberation chambers also have requirements that have to be met. How these calibration tests should be performed and what requirements have to be met is captured in an international standard, IEC 61000-4-21 (International Electrotechnical Commission & Technical Committee 77, 2011).

To keep up with test facility demand it would be of great use to be able to speed up the design process. This can be done by accurately predicting reverberation chamber compatibility results beforehand. At low frequencies, electric field uniformity is more difficult to obtain. The lowest frequency for which the chamber reaches the emc requirements is called the lowest usable frequency (LUF). Being able to predict emc results near this frequency is therefore a very attractive opportunity.

Solving the electromagnetic wave equations in a modelled reverberation chamber with a complex geometry is analytically impossible. Therefore numerical methods are used to obtain an accurate approximation for the electric field inside the reverberation chamber. An increasingly popular numerical method for electromagnetic reverberation chamber modelling is the finite element method (FEM). This method which performs well for complex geometries, divides the complex geometry into simpler sub domains where it can solve the electromagnetic wave equations. Additionally, the finite element method produces a highly sparse matrix after discretization implying savings in computer memory and CPU time (Cangellaris, 1996). Due to the good documentation of the finite element method and its advantages as stated before, its use has rapidly increased in popularity for emc modelling.

To study the accuracy and reliability of using models to predict emc results, we will aim to produce a pre-characterization numerical model capable of handling and calculating electromagnetic fields within a rectangular reverberation chamber near its lowest usable frequency at 200 MHz. The model will replicate the shielded and reverberation chambers located at Comtest, Zoeterwoude. This company, with high expertise in emc testing, builds the "best-in class" shielded and reverberation chambers. Measurements done in these test facilities will be compared to the electric field calculated by the FEM based modelling software Comsol Multiphysics.

To most accurately contain the electromagnetic field behaviour in a model it is important to describe the theory behind this behaviour. This is elaborated on in chapter 2. In solving the problem of electromagnetic waves in a complex geometry, we need to specify solvers that solve the set of matrix equations supplied by the finite element method. These solvers have to be chosen carefully to cope with memory and CPU time limitations on personal computers. Chapter 3 will explain the considerations in the used numerical method along with the choice

of the solver for the pre-characterization model. The chosen solver is the GMRES method with geometric multigrid preconditioning and SOR vector pre-and postsmoothing. This solver has low memory requirements and has an robustness advantage over the traditional GMRES solver due to its ability to change preconditioning. The end of this chapter will briefly introduce the complex shifted laplacian, an innovation that put the Delft University of Technology on the map.

The pre-characterization model of a reverberation chamber has a complex geometry to be modelled. For this reason this model is gradually build up. First a model of just the antenna is created to test its performance. Thereafter this antenna will be put into a reflective shielded chamber, a reverberation chamber without mode stirrer. This chamber is also found at Comtest and will be used for measurements to test the accuracy of the model. This makes it possible to filter out errors before adding the complexity of the mode-stirrer. Additionally we shall consider an added dielectric object in the shielded chamber with antenna to test the effect of adding a dielectric object on the electric field inside the chamber. At last, the we will create a pre-characterization numerical model of the reverberation chamber with z-fold wall stirrer. All model-setups and meshes will be explained in chapter 4. Also, chapter 4 shows the general setup of the Comsol Multiphysics models. Finally this chapter discusses the comparison method that is used in the results.

The results from the models and the measurements will be shown in chapter 5. This will be done by comparing the electric field pattern acquired from the model to the measured electric field pattern in the shielded chamber environments. The pre-characterization numerical model for the reverberation chamber will be compared to the real reverberation chamber at Comtest by looking at the field uniformity as explained in chapter 4. The hypothesized behaviour of the introduced shifted laplacian preconditioner is checked using convergence results at the end of this chapter. All results are thereafter discussed in chapter 6 which will also propose explanations for any discrepancies of the model with respect to the measurements. A conclusion about the performance of the FEM based model will be drawn in chapter 7 based on the creation of the model and a comparison of the results. Along with a conclusion on the results revolving around the shifted laplacian preconditioner. At last it will include a proposition for future work to improve pre-characterization models of reverberation chambers.

2 Theory

To better understand the behaviour of electromagnetic waves in rectangular reverberation chambers, their properties will be described. We will consider four situations. One purely theoretical situation in which we consider a two-dimensional room described by x and y coordinates, and an electromagnetic field only having an electric field component in the z-direction. Tangential boundary conditions will be considered. The other three more realistic situations are: an empty rectangular metal chamber, a rectangular metal chamber loaded with a dielectric object and a rectangular metal chamber with a good conducting object acting as mode stirrer.

2.1 Mathematical Preliminaries

Before delving into the theory it is important to understand some mathematical concepts prevalent in the area of electromagnetic waves.

The gradient of a differentiable function (∇f) is an operator which returns the partial derivatives of the function it works on with respect to the considered variable. Throughout this thesis the usual Cartesian coordinate system with x,y and z will be considered. The mathematical definition of the gradient is:

$$\nabla f : \mathcal{R}^3 \to \mathcal{R}^3 \qquad s.t. \qquad \nabla f = \begin{bmatrix} \frac{\partial f}{\partial x} \\ \frac{\partial f}{\partial y} \\ \frac{\partial f}{\partial z} \end{bmatrix} \tag{1}$$

Divergence is an operator that works on a vector field $\overrightarrow{F}$. The divergence of the vector field $\left(\nabla \cdot \overrightarrow{F}\right)$ returns a scalar value signifying the rate of change of the vector field in a specific point. As can be seen from the operator it is the inner product of the gradient operator and the vector field. More precisely:

$$\nabla \cdot \overrightarrow{F} : \mathcal{R}^3 \to \mathcal{R} \qquad s.t. \qquad \nabla \cdot \overrightarrow{F} = \frac{\partial \overrightarrow{F}_x}{\partial x} + \frac{\partial \overrightarrow{F}_y}{\partial y} + \frac{\partial \overrightarrow{F}_z}{\partial z} \tag{2}$$

The curl operator describes the rotation of the vector field. The curl of a vector field $\left(\nabla \times \overrightarrow{F}\right)$ in a point returns a vector whose length and direction specify the rotation at that point. The curl in the Cartesian coordinates is given by:

$$\nabla \times \overrightarrow{F} = \left(\frac{\partial F_z}{\partial y} - \frac{\partial F_y}{\partial z}\right)\hat{x} + \left(\frac{\partial F_x}{\partial z} - \frac{\partial F_z}{\partial x}\right)\hat{y} + \left(\frac{\partial F_y}{\partial x} - \frac{\partial F_x}{\partial y}\right)\hat{z} \tag{3}$$

Finally we have the differential operator which is often seen in partial differential equations like the electromagnetic wave equation. The differential operator ($\mathcal{L}$) is a function of the differentiation operators. Examples of differential operators are the ∇ operator, as seen in the gradient and the Laplace operator $\Delta = \nabla^2$. Linearity is an important property of the differential operator. So $\mathcal{L}(af + bg) = a\mathcal{L}(f) + b\mathcal{L}(g)$, where a, b are constants and f, g are functions.

2.2 Governing wave equation

To fully define the properties of electromagnetic waves we would like to know the differential equation that governs them and the relevant boundary conditions. Electromagnetic waves are described by second-order wave equations derived from the Maxwell equations. These are:

$$\nabla \cdot D = \rho_f, \qquad \text{Gauss's law} \tag{4a}$$
$$\nabla \cdot B = 0 \tag{4b}$$
$$\nabla \times E = -\frac{\partial B}{\partial t}, \qquad \text{Faraday's law} \tag{4c}$$
$$\nabla \times H = J_f + \frac{\partial D}{\partial t}, \qquad \text{Maxwell-Ampere's law} \tag{4d}$$

in which D is the displacement electric field, ρ_f is the free charge, so the charges that can move around freely. B is the magnetic field, E is the electric field, H is the auxiliary magnetic field and J_f is the free current density. To derive the second-order wave equation for the electric field as used in Comsol Multiphysics we assume that the material is linear and time-invariant. We will use the auxiliary magnetic field as it is called in (Griffiths, 2013). H defined by $B = \mu H$ with $\mu = \mu_0 \mu_r$ being the total magnetic permeability of a material. This is the same for the total permittivity of a material $\epsilon = \epsilon_0 \epsilon_r$. the displacement electric field D is defined as $D = \epsilon E$ in linear and time-invariant media. μ_0 is the permeability of free space and ϵ_0 is the permittivity of free space. These are better known as magnetic and electric constant respectively.

Taking the curl of the adapted Faraday's law we get:

$$\nabla \times \left(\mu^{-1} \nabla \times E\right) = -\frac{\partial \left(\nabla \times H\right)}{\partial t} \tag{5}$$

Using the assumptions of a linear and time-invariant media and considering no charges, the Maxwell-Ampere's law turns into:

$$\nabla \times H = \sigma E + \epsilon \frac{\partial E}{\partial t} \tag{6}$$

The second-order wave equation follows from filling in this new Maxwell-Ampere equation, 6.

$$\nabla \times \left(\mu^{-1} \nabla \times E\right) = -\sigma \frac{\partial E}{\partial t} - \epsilon \frac{\partial^2 E}{\partial t^2} \tag{7}$$

We convert this equation to the frequency domain using the Fourier transform. We get the equation as used by Comsol Multiphysics:

$$\nabla \times \left(\mu_r^{-1} \nabla \times E\right) - k_0^2 \left(\epsilon_r - \frac{j\sigma}{\omega \epsilon_0}\right) E = 0 \tag{8}$$

where μ_r is the relative magnetic permeability with respect to the permeability in free space, ϵ_r is the relative permittivity with respect to the permittivity in free space, j is the imaginary unit, ω is the angular frequency and k_0 is the wavenumber in vacuum. k_0 follows from our use of the dispersion relation in vacuum $k_0 = \omega \sqrt{\mu_0 \epsilon_0}$.

This equation used by Comsol Multiphysics can still be simplified as we will see in the next two subsections. These subsections will show the Helmholtz equation, the wave equation in the frequency domain. This equation has a general solution of the form:

$$\mathbf{E}(\mathbf{r}, t) = E_0 e^{j(\mathbf{k} \cdot \mathbf{r} - \omega t + \delta)} \hat{\mathbf{n}} \tag{9}$$

Here E_0 is a constant specifying the amplitude of the propagating wave. $\boldsymbol{k}$ is the wave vector, which specifies the propagation direction. Its length is the wave number $k = \omega/v$, where v is the propagation speed. $\boldsymbol{r}$ specifies the propagation direction, t is the time in seconds, δ is a phase factor and $\hat{\mathbf{n}}$ is the polarization direction which is the direction in which the oscillations take place.

2.3 Electromagnetic waves in vacuum

Considering electromagnetic waves in vacuum is the simplest case. The relative permittivity and permeability are then 1 thus the total permittivity and permeability are equal to that of free space. Also the conductivity σ is 0, therefore we can omit the second part in brackets in the equation 8. This equation then reduces to

$$\nabla \times \nabla \times E - k_0^2 E = 0 \tag{10}$$

To get the Helmholtz equation we use the curl of curl vector identity $\nabla \times \nabla E = \nabla(\nabla \cdot E) - \nabla^2 E$. Where $\nabla \cdot E = 0$ without free charges. The Helmholtz equation is given by:

$$(\nabla^2 + k_0^2)E = 0 \tag{11}$$

From this equation and the dispersion relation we can see that the wave speed in vacuum is given by $v = \frac{1}{\sqrt{\mu_0 \epsilon_0}} = c$. Thus in vacuum electromagnetic waves travel at light speed.

Electromagnetic waves are oscillations in the electric and magnetic field. Like waves in water at a water surface, they are transverse waves meaning that the oscillation direction of the electric and magnetic fields are perpendicular to the propagation path. Mathematically this is specified as $\hat{\mathbf{n}} \cdot \hat{\mathbf{k}} = 0$.

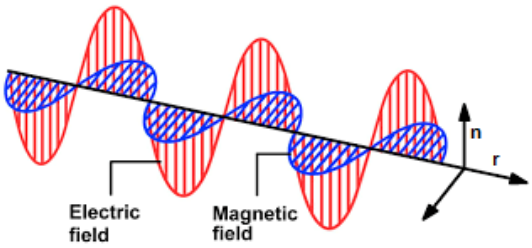

Figure 1: Electromagnetic wave propagating in the **r** direction with an electric field component polarized in the **n** direction (Saleh, 2017).

Additionally electromagnetic waves can interfere due to the fact that they have a phase δ as shown in the general solution 9. Interference can cause two overlapping waves to superpose forming a wave with a greater, smaller or same amplitude. Whenever the phase difference between waves is $\Delta\delta = 2\pi n$ we call the waves in phase. The waves then superpose to interfere constructively. The opposite is also possible when two waves are out of phase, $\Delta\delta = (2n + 1)\pi$, therefore destructively interfering. The superposition of all waves form an electromagnetic radiation pattern.

2.4 Electromagnetic waves in matter

In analyzing the behaviour of electromagnetic waves in matter we assume that the medium is linear and homogeneous, thus ϵ and μ do not vary for different points in the same medium.

To evaluate the velocity of the electromagnetic wave in matter we still consider a conductivity of 0. However we replace k_0^2 in equation 10 by k^2. The removal of the subscript signifies that we are talking about the more general $\sqrt{\epsilon\mu}$ instead of their respective counterparts in vacuum. Replacing this in the formula for the velocity we get

$$v = \frac{1}{\sqrt{\epsilon\mu}} = \frac{c}{n}$$

in which n is the index of refraction of the material. The index of refraction is defined by $n \equiv \sqrt{\frac{\epsilon\mu}{\epsilon_0\mu_0}} = \sqrt{\epsilon_r\mu_r}$. The refractive index can also be related to the wavenumber with the formula $k = \frac{\omega n}{c} = k_0 n$. Most materials have a relative permeability close to 1 and a relative permittivity greater than 1 thus in general electromagnetic waves travel more slowly through matter (Griffiths, 2013).

Before, we assumed zero conductivity, though this is unrealistic as no material is a perfect dielectric. To better describe behaviour of electromagnetic waves in matter we need to consider non-zero conductivity, complex permittivity and permeability. We will focus on the conductivity and complex permittivity. The complex relative permittivity ϵ is defined as $\epsilon_r = \epsilon_r' - j\epsilon_r$" with ϵ_r' being the real part of the relative permittivity and ϵ_r'' the imaginary part. The conductivity can be defined as $\sigma = \omega\epsilon''$. We can now re-write the term in brackets in the general wave equation 8 to $k_0^2(\epsilon_r' - j\epsilon_r'')$. Although not used in Comsol Multiphysics, by multiplying by the relative permeability we now see that we can simplify equation 8 to:

$$\nabla \times \nabla \times E - k^2 E = 0 \tag{12}$$

which can again be written similar to the Helmholtz equation without charges:

$$(\nabla^2 + k^2)E = 0 \tag{13}$$

This has the same general solution as before in 9 but now the wavenumber k has a complex value. To be more exact we shall continue to call this wavenumber $\tilde{k} = k + i\kappa$. Using that $\tilde{k}^2 = \mu\epsilon\omega^2 + j\mu\sigma\omega$ we can write $\tilde{k}$ in terms of permittivity and permeability:

$$k \equiv \omega\sqrt{\frac{\epsilon\mu}{2}}\left(\sqrt{1 + \left(\frac{\epsilon"}{\epsilon}\right)} + 1\right)^{1/2} \qquad \text{Real part of the wavenumber} \tag{14a}$$

$$\kappa \equiv \omega\sqrt{\frac{\epsilon\mu}{2}}\left(\sqrt{1 + \left(\frac{\epsilon"}{\epsilon}\right)} - 1\right)^{1/2} \qquad \text{Imaginary part of the wavenumber} \tag{14b}$$

To show the absorption due to a complex permittivity we write the general solution as:

$$\mathbf{E}(\mathbf{r}, t) = E_0 e^{-\boldsymbol{\kappa}\cdot\mathbf{r}} e^{i(\mathbf{k}\cdot\mathbf{r} - \omega t + \delta)}\hat{\mathbf{n}} \tag{15}$$

This solution shows that amplitude of the electromagnetic wave decreases for increasing imaginary part of the wavenumber. In other words, the absorption increases as the imaginary part of the wavenumber is increased. By definition 14b we see that this happens for increasing imaginary part of the permittivity. Additionally the absorption rises for increasing permeability. The distance that an electromagnetic wave needs to travel through a material to decrease its amplitude by a factor of $\frac{1}{e}$ is called the skin depth $d \equiv \frac{1}{\kappa}$.

2.5 Electromagnetic waves at an interface

At the interface between two media, like an added dielectric object, the electric field will generally be discontinuous. These discontinuities can be deduced from Maxwell's equations in integral form:

$$\oint_{\partial\Omega} \mathbf{D} \cdot d\mathbf{a} = Q_{fencl} \qquad \text{Gauss's law} \tag{16a}$$

$$\oint_{\partial S} \mathbf{E} \cdot d\mathbf{l} = -\frac{d}{dt} \int_S \mathbf{B} \cdot d\mathbf{a} \qquad \text{Maxwell-Faraday equation} \tag{16b}$$

Equation 16a is taken over the surface boundary $\partial\Omega$ of an arbitrary volume Ω. $\mathbf{D}$ represents the electric displacement field defined as $\mathbf{D} = \epsilon\mathbf{E}$ in a linear homogeneous media. Q_{fencl} represents the free charge enclosed by the volume Ω. $\mathbf{a}$ is the surface on the infinitely thin boundary wafer over which is integrated. $\mathbf{a}$ is defined as positive going from domain 2 to 1. Applying Gauss's law to the pillbox volume as shown in figure 2 and letting the thickness go to zero, we get that the component of $\mathbf{D}$ perpendicular to the surface is discontinuous by an amount equal to the surface charge σ_f. In equations this is:

$$\mathbf{a} \cdot (\mathbf{D}_1 - \mathbf{D}_2) = \mathbf{D}_1^{\perp} - \mathbf{D}_2^{\perp} = \sigma_f \tag{17}$$

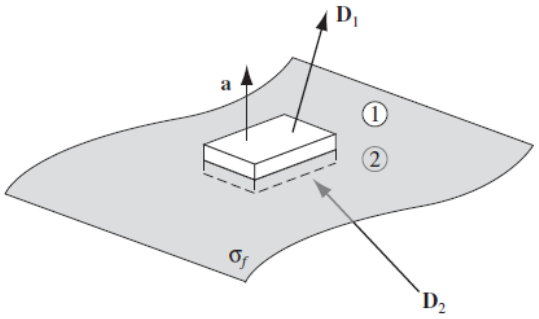

Figure 2: An infinitely thin wafer specifying the boundary between media 1 & 2 with surface charge σ_f. $\mathbf{D}$ is the displacement field in pillbox shaped volume. $\mathbf{a}$ is assumed to be normal on the surface and pointing away from domain 2 (Griffiths, 2013).

Equation 16b is defined on surface S perpendicular to the interface surface. ∂S is the closed boundary line of surface S often referred to as Amperian loop. The normal $\hat{\mathbf{n}}$ points away from domain 2. We apply the Maxwell-Faraday equation to the Amperian loop as shown in figure 3 and let the sides perpendicular to interface shrink to 0. This tells us that the parallel components of $\mathbf{E}$ are continuous across the boundary. In equations this is:

$$\hat{n} \times (\mathbf{E}_1 - \mathbf{E}_2) = \mathbf{E}_1^{\parallel} - \mathbf{E}_2^{\parallel} = 0 \tag{18}$$

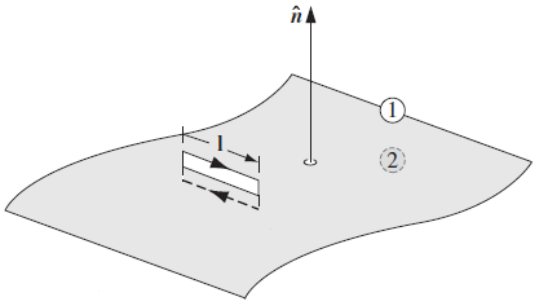

Figure 3: An infinitely thin wafer specifying the boundary between media 1 & 2. The line $\mathbf{l}$ is the surface line of the perpendicular surface S. is the normal of the boundary surface pointing away from domain 2 (Griffiths, 2013).

The effect of these interface conditions is a shift in the propagation direction of the electromagnetic waves between two media. A wave hitting a boundary at oblique incidence also has a reflected and transmitted part. We have:

$$\mathbf{E}_I(\mathbf{r}, t) = \mathbf{E}_{0,I} e^{j(\mathbf{k}_I \cdot \mathbf{r} - \omega t)} \tag{19a}$$

$$\mathbf{E}_R(\mathbf{r}, t) = \mathbf{E}_{0,R} e^{j(\mathbf{k}_R \cdot \mathbf{r} - \omega t)} \tag{19b}$$

$$\mathbf{E}_T(\mathbf{r}, t) = \mathbf{E}_{0,T} e^{j(\mathbf{k}_T \cdot \mathbf{r} - \omega t)} \tag{19c}$$

In these incident, reflected and transmitted wave solutions, the subscripts indicate the respective amplitudes $\mathbf{E_0}$ and wavevectors $\mathbf{k}$ as shown in figure 4. The angular frequency ω is the same for all three waves. The three wavenumbers are related by $k_I = k_R = \frac{n_1}{n_2} k_T$.

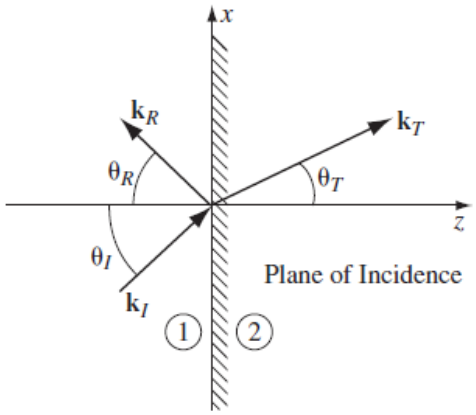

Figure 4: The incident, reflected and transmitted wave at a boundary in the xy-plane with their respective wavenumber k and angle θ (Griffiths, 2013).

The direction of the reflected and transmitted waves can be calculated making use of the law of reflection and the law of refraction also known as Snell's law. The law of reflection gives us that the angle of incidence θ_I and the angle of reflection θ_R are the same, so $\theta_I = \theta_R$. Snell's law gives an expression for the transmitted angle θ_T, being $\frac{sin(\theta_T)}{sin(\theta_I)} = \frac{n_1}{n_2}$.

After some algebraic computations using the interface equations, we find the amplitudes of the reflected and transmitted waves given by the Fresnel equations:

$$\mathbf{E}_{0,R} = \left(\frac{1-\alpha\beta}{1+\alpha\beta}\right)\mathbf{E}_{0,I}, \tag{20a}$$

$$\mathbf{E}_{0,T} = \left(\frac{2}{1+\alpha\beta}\right)\mathbf{E}_{0,I} \tag{20b}$$

α is defined as $\alpha \equiv \frac{cos(\theta_T)}{cos(\theta_I)}$ and β is defined as $\beta \equiv \frac{\mu_1 n_2}{\mu_2 n_1}$ (K. Zhang & Li, 2008). Note that these equations are given for transverse electric modes, so for perpendicular polarization as we will consider in our purely theoretical 2D wave problem.

We can then define the power reflection coefficient R and power transmission coefficient T as:

$$R \equiv \left(\frac{1-\alpha\beta}{1+\alpha\beta}\right)^2 \tag{21a}$$

$$T \equiv \alpha\beta\left(\frac{2}{1+\alpha\beta}\right)^2 \tag{21b}$$

These coefficients signify the fraction of the incident energy that is reflected and transmitted. For the power reflection at a conducting surface we have to consider complex wavenumber $\tilde{k}$. The Fresnel equations at normal incidence then become:

$$E_{0,R} = \left(\frac{1 - \tilde{\beta}}{1 + \tilde{\beta}} \right) \tag{22a}$$

$$E_{0,T} = \left(\frac{2}{1 + \tilde{\beta}} \right) \tag{22b}$$

where $\tilde{\beta} = \frac{\mu_1 v_1}{\mu_2 \omega} \tilde{k_2}$ with v being the wave velocity in medium 1 and $\tilde{k_2}$ the complex wavenumber in medium 2. As conductivity, or imaginary part of the permittivity, rises the wavenumber rises and therefore so does the reflectance. This is why metals are very reflective. For high permeability in domain 2, $\tilde{\beta}$ goes to zero so the reflection also goes to zero. Therefore absorbers wants high permeability to transmit as much electromagnetic radiation radiation as possible combined with a high imaginary part of the permittivity to absorb the radiation.

2.6 Boundary Conditions

Similarly to the interface conditions as defined in 17 & 18, we must also define boundary conditions at the boundary of the domain of our second-order wave equation. We need boundary conditions to find an unique solution to the evaluated problem on the domain of interest as many functions satisfy the second-order wave equation without boundary conditions. Boundary conditions are not to be confused with interface conditions and specify an exterior boundary used in calculations, thus no calculations are performed behind these boundaries. As the name suggests it defines the boundary between the domain of interest and the rest of space. This restriction to the domain of interest should be both physically correct and ensure that the problem is solvable in finite time. Throughout this thesis we will require boundary conditions for metal objects specifically the perfect electrical conductor boundary condition and the impedance boundary condition.

Metals conduct electricity well and have high reflectively. This is due to their non-zero conductivity. As seen before in subsection 2.3 this means that there will be absorption. We call metals lossy materials (Frei, 2015).

The perfect electric conductor boundary condition considers a surface with infinite conductivity. Therefore the entire incident wave is reflected and the skin depth is 0. Perfect conductors cannot have an interior electric field as the interior charges will immediately cancel the effect of the electric field. If domain 2 is a perfect conductor in equation 18 we then get:

$$\hat{n} \times \mathbf{E} = 0 \tag{23}$$

where $\mathbf{E}$ is the electric field in domain 1 and $\hat{n}$ is the normal point away from the conductor like figure 3.

The impedance boundary condition is used for imperfect conducting objects which have a size much larger than the skin depth. These objects will have currents running through them, however we approximate these currents as running on the surface. This approximation is allowed since the skin depth is much smaller than the size of the object. In this way the domain behind the impedance boundary is considered to be infinitely large exempting them from the region of interest. The electric field on the surface of the object with impedance boundaries is given by:

$$\sqrt{\frac{\mu_0 \mu_r}{\epsilon_0 \epsilon_r - j\sigma/\omega}} \hat{n} \times \mathbf{H} + \mathbf{E} - (\hat{n} \cdot \mathbf{E}) \hat{n} = (\hat{n} \cdot \mathbf{E}_S) \hat{n} - \mathbf{E}_S \tag{24}$$

where $\hat{n}$ is again the normal pointing away from the conductor, $\mathbf{E}$ and $\mathbf{H}$ are the electric and magnetic field in domain 1 respectively. $\mathbf{E}_S$ is the source electric field which can be used to specify a source surface current on the boundary (M. Comsol, 2020e).

2.7 Reverberation Chamber

A reverberation chamber is essentially a chamber with high reflectivity. This reflectivity is both due to highly conductive exterior walls, but additionally a mode stirrer is added to the chamber. This mode-stirrer is made from a metal and can rotate 360 degrees. The reflactance in the chamber is an effect of the high reflectivity of the used metals as seen in sub-section 2.4. In a numerical model the low transmittance of metals can be converted to boundary conditions as seen the previous sub-section. The exterior boundaries will be regarded as perfect conductors and the interior rotating mode-stirrer will have impedance boundary conditions. As an effect the domain interior of the stirrer is not considered. The goal of a reverberation chamber is to have an electric field that is as uniform as possible (Serra et al., 2017). Figure 5 shows the general setup of a reverberation chamber.

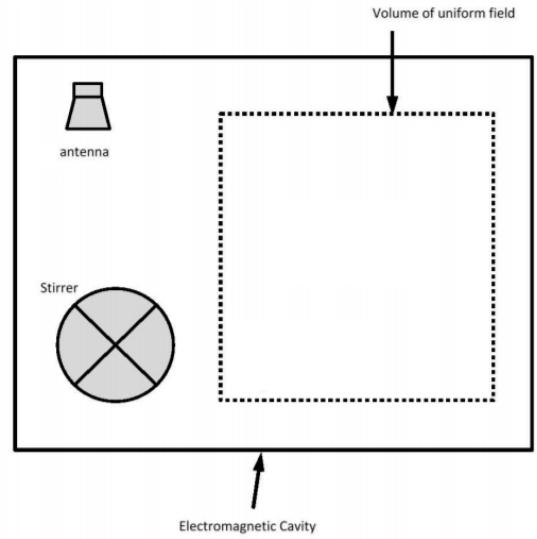

Figure 5: Typical reverberation chamber setup with the stirrer in one corner, an antenna pointed to the corner behind the stirrer and the working volume (Serra et al., 2017)

In practice, statistical field uniformity is considered to characterize reverberation chambers. This means that instead of an electric field that is "the same everywhere at every moment in time", the electric field is "on average and within uncertainty the same at different spatial locations" (Serra et al., 2017). The spatial locations are the 8 corners of the working volume. The working volume is the volume inside a reverberation chamber such that it is at least one fourth of a wavelength from the nearest object as defined in IEC 61000-4-21. The electric field is considered statistically uniform whenever the statistical parameters, like mean and standard deviation, are below a limit set by IEC 61000-4-21 after a full rotation cycle of the stirrer. The limit on the standard deviation set by the IEC 61000-4-21 is 4 dB at 100 MHz decreasing linearly to 3 dB at 400 MHz (International Electrotechnical Commission & Technical Committee 77, 2011).

The article (Liu, Chang, & Ma, 1983) discusses the amount of propagating modes in a rectangular cavity. They found that for increasing frequency there is an increasing amount of propagating modes inside the cavity. This means that for low frequencies the observed electric field in the reverberation chamber will be a superposition of few propagating modes. For higher frequencies the electric field is a superposition of many propagating modes. Therefore the field is likely to be more complex for high frequencies. The lowest frequency for which the electric field in the working volume complies with the IEC 61000-4-21 requirements is called the lowest usable frequency (LUF). The wavelength increases as the frequency decreases, therefore the wavelength at LUF is used to define the working volume. Additionally, the lowest usable frequency can be lowered by increasing the size of the mode stirrer. Intuitively a larger mode-stirrer can reflect more electromagnetic waves and therefore improve statistical field uniformity. This does go at the cost of a smaller working volume as this has to be one fourth of a wavelength separated from the nearest object.

2.8 Analytic solution

Ideally we would like to solve the second-order wave equation with its boundary conditions without approximations. This requires some assumptions simplifying the problem. Let us consider a 2D rectangular reverberation room domain with dimensions $(a \times b)$ in respectively the x and y direction. The room is infinitely long in the z-direction and is excited by a current-line source of magnitude I_0 located at (x_0, y_0) as shown in figure 6. We will use the results of this analytical problem later in subsection 3.7 to be able to describe a numerical preconditioning method.

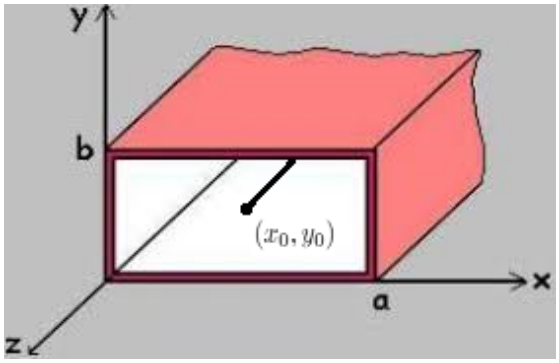

Figure 6: The rectangular reverberation room has dimensions $(a \times b)$ in respectively the x and y direction and is infinitely long in the z-direction. A line source is located at (x_0, y_0) (Aksun, 2020)

Moreover, we assume that the electric field only has a transverse component in the vertical z-direction. Consequently when talking about E we are actually talking about E_z, so $E = E_z$. The reverberation room is filled with a material of arbitrary conductivity and unit relative permittivity and permeability. Additionally we assume perfect conducting boundary conditions. The second-order wave equation 8 then becomes:

$$\left(\nabla^2 + k^2\right) E = j\omega\mu_0 I_0 \delta(x - x_0)\delta(y - y_0) \tag{25}$$

This problem can be solved using the eigenfunction expansion method. We write $L(u) = Q$ with homogeneous boundary conditions. In which u(x,y) is used instead of $E_z(x, y)$ throughout the calculations as this is convention (Haberman, 2013). L is the wave operator defined as

$L = \left(\nabla^2 + k^2\right)$ and Q is the source term. We also have $L(\phi_{nm}) = -\lambda_{nm}\sigma\phi_{nm}$ in which ϕ are the eigenfunctions, λ are the eigenvectors and σ is the appropriate orthogonality factor. This has the same boundary conditions as above. The solution u(x,y) can be written as $u(x,y) = \sum_{m=-\infty}^{\infty}\sum_{n=-\infty}^{\infty} A_{nm}\phi_{nm}$ due to the superposition principle in which A_{nm} are the amplitude coefficients and ϕ_{nm} are the eigenfunctions. Using the orthogonality condition we get:

$$A_{nm} = -\frac{1}{\lambda_{nm}}\frac{\int_0^b\int_0^a Q\phi_{nm}dxdy}{\int_0^b\int_0^a \phi_{nm}^2\sigma dxdy} \tag{26}$$

To solve this we need to calculate the eigenvalues and eigenfunctions. These can be acquired solving equation 25 disregarding the source term. The equation then is:

$$\nabla^2 E + k^2 E = -\lambda_{nm}E \tag{27}$$

In this equation λ_{nm} are the eigenvalues and $k^2 = k_x^2 + k_y^2$. The equation is linear and homogeneous so it may be solved using separation of variables. Using this method we get eigenfunctions equal to $\phi_{nm} = \sin(\frac{\pi nx}{a})\sin(\frac{\pi my}{b})$ and the eigenvalues equal to $\lambda_{nm} = \left(\frac{n\pi}{a}\right)^2 + \left(\frac{m\pi}{b}\right)^2 - k^2$. Using this to calculate A_{nm} we get the final result:

$$u(x,y) = \frac{4j\omega\mu_0 I_0}{ab}\sum_{m=1}^{\infty}\sum_{n=1}^{\infty}\frac{\sin(\frac{\pi nx_0}{a})\sin(\frac{\pi my_0}{b})\sin(\frac{\pi nx}{a})\sin(\frac{\pi my}{b})}{k^2 - \left(\frac{n\pi}{a}\right)^2 - \left(\frac{m\pi}{b}\right)^2} \tag{28}$$

3 Numerical Solution

Unlike the problem seen in subsection 2.8, many realistic equations are not analytically solvable. Due to the complexity of our geometry this also holds for rectangular reverberation rooms excited by an antenna. Even though the problems are impossible to solve analytically, an approximate solution is still of interest in such problems. We derive these approximate solutions using numerical methods. The GMRES solver with multigrid preconditioning and SOR vector smoothing will be discussed as this is the solver used to calculate the electric field from the acquired system of equations. At the end, a shifted laplacian preconditioner, an innovation of the Delft University of Technology, will briefly be discussed.

3.1 General Numerical Solution

A numerical solution is the approximation of the exact solution of the considered problem. We continue the convention of calling the exact solution u. The numerical solution is given by u_h. It is an approximation thus $u - u_h = \zeta$, where ζ is used to express the numerical error instead of the conventional ϵ to avoid confusion with the permittivity constant.

Vital to numerical methods is the fact that the exact solution can be written as a linear combination of basis functions N_j thereby satisfying:

$$u = \sum_{j=1}^{\infty} u_j N_j \tag{29}$$

Where u_j specifies the unknown solution at point j. They are also called expansion coefficients for each basis function. As we cannot work with an infinite number of terms, we approximate the exact solution with a N number of them. The numerical solution is therefore given by:

$$u_h = \sum_{j=1}^{N} u_j N_j \tag{30}$$

Basis functions can be chosen arbitrarily and are therefore known. Some frequently used examples are powers, sines and cosines. We would like to known the expansion coefficients c_j thereby knowing the solution to our problem.

3.2 General FEM

There is a plethora of numerical methods, all having their respective advantages and disadvantages. The finite element will be discussed further as this method will be implemented later in the model.

The finite element method is a numerical method that divides the domain of a boundary value problem Ω into smaller sub-domains Ω^e called finite elements. All elements of the spatial discretization together is called the mesh.

The finite element method is divided in 5 steps.

1. Defining the geometry or domain of the considered boundary value problem

2. Define the physics on the domain. This includes choosing the partial differential equation, boundary conditions and initial conditions that apply to the considered boundary value problem

3. Define the mesh on the considered domain. This includes choosing the amount of elements, their shape and their distribution. A domain with many fluctuations of the function of interest requires denser meshing than a domain that is constant

4. Discretize the boundary value problem based on the predefined mesh to form a system of algebraic equations

5. Solve the system using direct or iterative solvers

Step 1 up and until 3 will be discussed in the next chapter about the implementation of the finite element method. We will continue with step 4 by outlining the general discretization process of the finite element method.

3.3 Discretization of Space

During discretization, the domain of interest Ω is split up into sub-domains or elements Ω^e $(e = 1, 2, 3, \ldots, N)$ with N denoting the total amount of elements. These elements can have different shapes. In 1D they are a straight line between two nodes at the endpoints of the line segment. In 2D and 3D the elements are triangular and rectangular shapes or composites of these. They have nodes at their vertices as shown in 7&8.

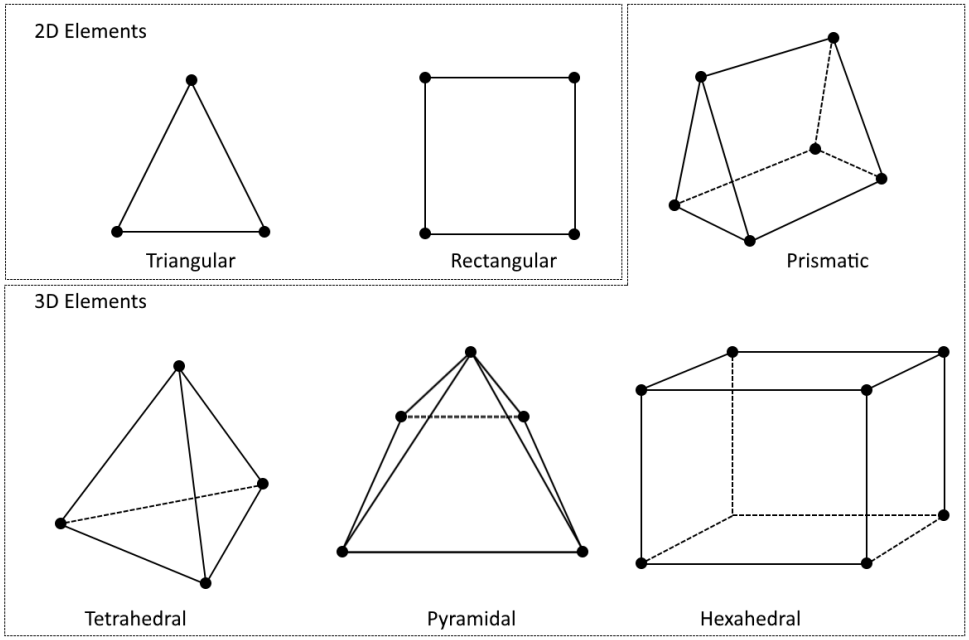

Figure 7: The different element shapes in 2D and 3D along with their node placement for first-order elements (Comsol, 2017)

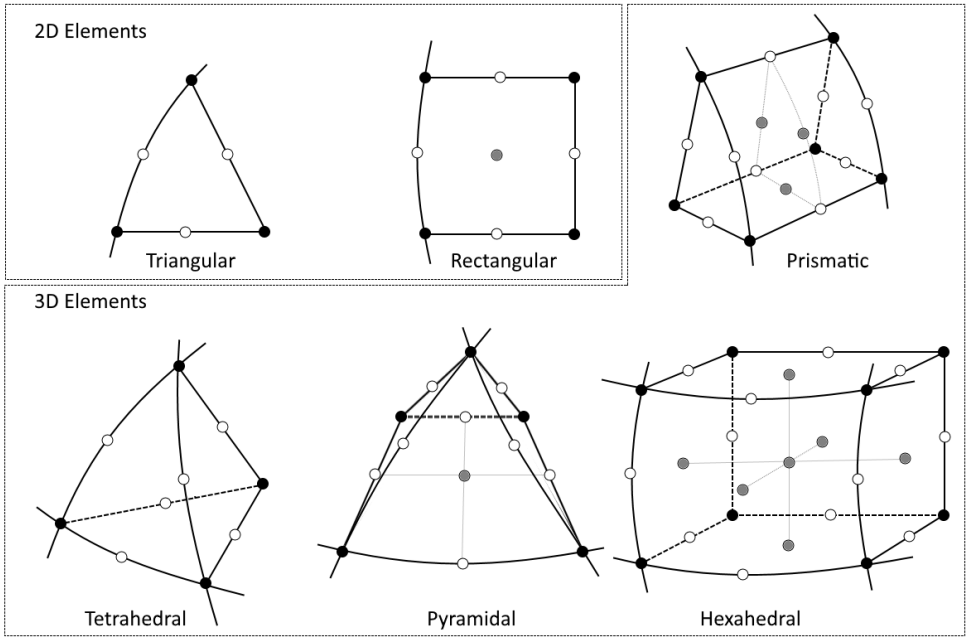

Figure 8: The different element shapes in 2D and 3D along with their node placement for second-order elements (Comsol, 2017)

Boundaries do not have to be perfectly straight. Second order elements are often used for boundary conditions that are curved and interior domains having straight lines or surfaces. This significantly improves the accuracy of the modelled domain. However more nodes are used to model second-order elements therefore requiring more memory and converging more slowly (Frei, 2016).

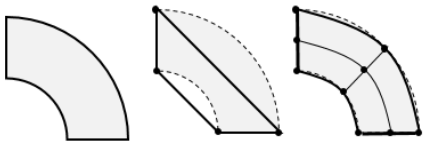

Figure 9: A curved domain approximated by a first-order element: middle and a second-order quadrilateral element: right (Frei, 2016)

Conventionally the finite element method using node elements was used. This method assigns the unknown electric field coefficients to the vertices of the elements like the vertices in figure 7. Using the node elements and the corresponding basis functions could be used for electric field calculations. Though, this method has three major problems. There is occurrence of non-physical solutions, the boundary conditions on material interfaces are difficult to impose and it is difficult to define edges and corners of a geometry (Jin, 2015). Instead edge-elements will be used in what is called vector finite element analysis. These elements are shown in figure 10. The unknown electric field values are assigned to the edges of the of an element instead of the nodes.

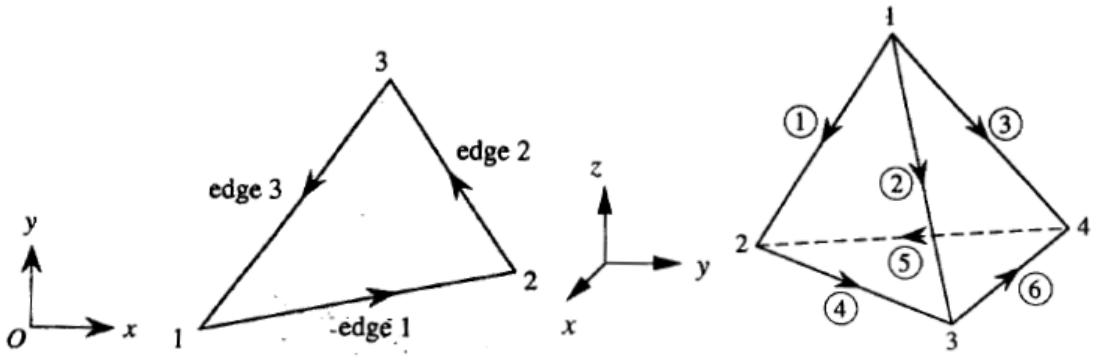

(a) (b)

Figure 10: The edge-elements used in the discretization of 2D and 3D geometries respectively. Subfigure (a) shows the triangular edge element and subfigure (b) shows the tetrahedral edge element

The problem that was formerly formulated on the entire domain can now be formulated as u at the edges of the respective elements. After this discretization of the domain Ω into elements Ω^e we select the vector basis functions. These provide an approximation of the unknown solution in each element Ω^e. The expression has the following form similar to 30:

$$u_h^e = \sum_{j=1}^{M} = u_j^e N_j^e \tag{31}$$

Here u^e is the unknown approximated solution in element e, M is the total number of edges in element e, u_j^e is the unknown value of u at edge j of element e and N_j^e is the vector basis function for edge j. Note that the order of the element corresponds to the order of the function used in the vector basis function N_j^e. Additionally, the vector basis functions are only nonzero within their respective element.

Before proceeding to the interpolation function for edge elements, we will define simplex coordinates using the conventional nodal elements. Similarly to equation 31 we can approximate the unknown solution in each element using nodal elements. If we consider a linear triangular node element then the solution is approximated as $u_h^e = a^e + b^e x + c^e y$, where a^e, b^e and c^e are constant coefficients in element e which are to be determined. At the three nodes the approximation will be:

$$\begin{aligned} u_{h,1}^e &= a^e + b^e x_1 + c^e y_1 \\ u_{h,2}^e &= a^e + b^e x_2 + c^e y_2 \\ u_{h,3}^e &= a^e + b^e x_3 + c^e y_3 \end{aligned}$$

where x_j^e and y_j^e denote the coordinate values at the j-th node at the e-th element.
We can now define the simplex coordinates (L_1^e, L_2^e, L_3^e). They are given by:

$$L_j^e = \frac{1}{\Delta^e}\left(a_j^e + b_j^e x + c_j^e y\right) \qquad j = 1, 2, 3 \tag{32}$$

in which

$$\begin{array}{lll} a_1^e = x_2^e y_3^e - y_2^e x_3^e & b_1^e = y_2^e - y_3^e & c_1^e = x_3^e - x_2^e \\ a_2^e = x_3^e y_1^e - y_3^e x_1^e & b_2^e = y_3^e - y_1^e & c_2^e = x_1^e - x_3^e \\ a_3^e = x_1^e y_2^e - y_1^e x_2^e & b_3^e = y_1^e - y_2^e & c_3^e = x_2^e - x_1^e \end{array}$$

and the area of the e-th element:

$$\Delta^e = \frac{1}{2}\begin{vmatrix} 1 & x_1^e & y_1^e \\ 1 & x_2^e & y_2^e \\ 1 & x_3^e & y_3^e \end{vmatrix}$$

The simplex coordinates (L_1^e, L_2^e, L_3^e) are also the linear interpolation functions of the nodal elements.

3.4 Interpolation functions

To calculate the unknown electric field value in element e we need interpolation functions. Whitney- 1-form basis functions will be considered for the triangular edge element shown in figure 10a. The Whitney vector basis functions are denoted by $\mathbf{W_i^e}$, where i is the edge element, or $\mathbf{W_{ij}^e}$, where the edge between node i and j is used as discussed in (Nentchev, 2008). We define the length of the edges intuitively as $l_1 = |\mathbf{r_1}|, l_2 = |\mathbf{r_2}|, l_3 = |\mathbf{r_3}|$.The Whitney basis-function for edge 1 is given by:

$$\mathbf{W_1} = L_1^e \nabla L_2^e - L_2^e \nabla L_1^e \tag{33}$$

The divergence and curl of the Whitney function are given by:

$$\nabla \cdot \mathbf{W_1^e} = \nabla L_1^e \cdot L_2^e - \nabla L_2^e \cdot \nabla L_1^e = 0$$
$$\nabla \times \mathbf{W_1^e} = \nabla L_1^e \times \nabla L_2^e - \nabla L_2^e \times \nabla L_1^e = 2\nabla L_1^e \times \nabla L_2^e$$

The Whitney function $\mathbf{W_i^e}$ has a constant tangential component in the direction of edge i. To show this for edge 1 we consider the unit vector $\mathbf{e_1}$ pointing from node 1 to node 2. L_1^e is a linear function that varies from 1 at node 1 to 0 at node 2 and L_2^e is a linear function being 1 at node 2 and 0 at node 1. Therefore we have $\mathbf{e_1} \cdot \nabla L_1^e = -\frac{1}{l_1^e}$ and $\mathbf{e_1} \cdot \nabla L_2^e = \frac{1}{l_2^e}$. We now show that the Whitney function for edge 1 has a constant tangential component in the direction of edge 1 as done in (Jin, 2015):

$$\mathbf{e_1} \cdot \mathbf{W_1^e} = \frac{(L_1^e + L_2^e)}{l_1^e} = \frac{1}{l_1^e}$$

By definition of the simplex coordinates L_1^e vanishes moving from node 2 to 3 and L_2^e vanishes moving from node 3 to 1. Therefore Whitney basis function $\mathbf{W_i^e}$ is a well defined vector basis function for edge 1.

Following the same derivation for edges 2 and 3 we get the interpolation functions:

$$N_1^e = \mathbf{W_1^e} l_1^e = (L_1^e \nabla L_2^e - L_2^e \nabla L_1^e)\, l_1^e \tag{34a}$$
$$N_2^e = \mathbf{W_2^e} l_2^e = (L_2^e \nabla L_3^e - L_3^e \nabla L_2^e)\, l_2^e \tag{34b}$$
$$N_3^e = \mathbf{W_3^e} l_3^e = (L_3^e \nabla L_1^e - L_1^e \nabla L_3^e)\, l_3^e \tag{34c}$$

where the lengths of the edges are used to normalise the interpolation functions. Note that the procedure for the tetrahedral edge element is entirely analogous, though more algebraically cumbersome.

3.5 Galerkin's Method of weighted residuals

To derive a system of equations for the discretized boundary value probelm we will use Galerkin's method of weighted residuals. We start by defining a general boundary value problem as:

$$\mathcal{L}u = f \tag{35}$$

Here $\mathcal{L}$ is the differential operator, u is the exact solution and f is a excitation or source function. In electromagnetics this differential operator is defined as in equation 12. Galerkin's method makes use of weighted residuals of the differential equation to find a solution to the boundary value problem. If we take the approximated solution u_h instead of the exact solution u we get:

$$r = \mathcal{L}u_h - f \neq 0 \tag{36}$$

where r indicates the residual. To optimize the approximation of the exact solution, the residual should be minimized on all point in our domain Ω. Weighted residual methods therefore make use of the following condition:

$$R_i = \int_\Omega w_i r d\Omega = 0 \tag{37}$$

This condition shows that the weighted residual integrals should be zero for every edge i because of the minimization of the residual. w_i are the weighting functions which can be chosen in various ways. In the Galerkin's method, the weighting functions are the same as the vector basis functions used to approximate the exact solution $w_i = N_i$ (Jin, 2015).

To form a system of algebraic equations we use the discretization discussed in the previous subsection. Equation 37 then becomes:

$$R_i^e = \int_{\Omega_e} N_i^e \left(\mathcal{L}u_h^e - f\right) d\Omega \qquad i = 1, 2, 3, \ldots, M \tag{38}$$

Which is the same weighted residual problem but now discretized per element e. The approximate solution u_h^e from equation 31 can now be substituted into 38. We get:

$$R_i^e = \int_{\Omega_e} N_i^e \mathcal{L} \sum_{j=1}^{M} u_j^e N_j^e d\Omega - \int_{\Omega_e} f N_i^e d\Omega \qquad i = 1, 2, 3, \ldots, M \tag{39}$$

Using the residual condition 37 we get the system of matrix equations:

$$\{K^e\}\{u_{h,i}^e\} = \{b^e\} \tag{40}$$

where $\{K^e\}$ is the M×M stiffness matrix and b^e is a M×1 column given by $K_{ij}^e = \int_{\Omega_e} N_i^e \mathcal{L} N_j^e d\Omega$ and $b_i^e = \int_{\Omega_e} f N_i^e d\Omega$ respectively. Since the basis functions give a non-zero value only for adjacent elements, the stiffness matrix only has non-zero elements for the set of adjacent elements. This leads to sparsity of the matrix since most elements are zero.

From (Cangellaris, 1996) we obtain the stiffness matrix and excitation vector for the electromagnetic wave equation as in equation 12. They have the following form:

$$K_{ij} = \int_\Omega \left(\frac{1}{\mu_r} \nabla \times N_i \right) \cdot (\nabla \times N_j)\, d\Omega + \int_\Omega k^2 N_i \cdot N_j d\Omega \tag{41a}$$

$$b_j = - \oint_{\partial\Omega} \frac{1}{\mu_r} \hat{n} \times (\nabla \times E) \cdot N_j ds \tag{41b}$$

Like before, k is complex wavevector, $\partial\Omega$ is the closed boundary of domain Ω, $\hat{n}$ is the normal vector pointing out of the domain and $N_{i,j}$ are the chosen vector basis functions.

3.6 Solutions of Discrete Problem

To calculate the electric field in all elements we have to solve the system of equations as shown above. This is done with the help of computer algorithms. As the aim is to solve the problem as accurately and fast as possible, it is important how the set of equations are handled. Due to the sparsity of the matrix, only the non-zero elements have to be stored. This reduces the storage requirement from $\mathcal{O}(N^2)$ to $\mathcal{O}(N)$ (Jin, 2011). Based on the properties of the matrix a the most efficient solver can be chosen.

There are two types of matrix solvers. The first type are the direct solvers which are mainly applied to full matrices, but some versions can also be used for sparse matrices. These methods are often more robust but require more memory. The second type are the iterative solvers who assume an approximate initial solution which is iterated to reach an approximation of the exact solution within a predefined acceptable error bound. These methods may require a large number of iterations to converge depending on the locations of the eigenvalues of the matrix. The amount of iterations is decreased by the use of a preconditioner.

As the number of edges increases, so do the dimensions of the matrix and thus the degrees of freedom that we need to solve for. As the memory of a personal working computer is limited, an iterative method will be considered. To be more exact the generalized minimum residual method (GMRES) will be discussed preconditioned with a geometric multigrid preconditioner. The GMRES allows different preconditioning methods to be used, this allows for higher efficiency and robustness (Saad, 1993). We shall also discuss the use of a smoother which are iterations used on the initial value to improve the initial approximation.

Suppose a large set of linear equations is considered like equation 40. This can be solved using the GMRES method with right preconditioning. The GMRES uses arnoldi iterations. These basically create an orthogonal basis using a modified Gram-Schmidt process (Saad, 1993). In the algorithm m is the amount of degrees of freedom of the system of equations. u_j is the approximated solution at step j of the algorithm so u_0 signifies the initial value. r_j is the residual at step j. v_j are the basis vectors which are orthogonalized and M is the preconditioning matrix. y_n is to be calculated in the algorithm using the linear least squares method.

Algorithm 1: GMRES with right preconditioning

Start : Choose u_0 and define an $(m+1) \times m$ matrix $\tilde{H_m}$ and initialize all its entries $h_{i,j}$ to zero.
Arnoldi process:
Compute $r_0 = b - Ku_0$, $\beta = ||r_0||_2$ and $v_1 = r_0/\beta$;
for *j=1,...,m* **do**
  Compute $z_j \coloneqq M^{-1}v_j$;
  Compute $w \coloneqq Kz_j$;
  for *i=1,...,j* **do**
    $h_{i,j} \coloneqq (w, v_i)$;
    $w \coloneqq w - h_{i,j}v_i$;
  end
  Compute $h_{j+1,j} = ||w||_2$ and $v_{j+1} = w/h_{j+1,j}$;
end
Define $V_m \coloneqq [v_1, \ldots, v_m]$.
From approximation solution:
Compute $u_m = u_0 + V_m y_m$ where $y_m = argmin_y ||\beta e_1 - \tilde{H_m} y||_2$ and $e_1 = [1, 0, \ldots, 0]^T$
if *satisfied* **then**
  stop;
else
  set $u_0 \leftarrow u_m$ and repeat Arnoldi iteration;
end

In the last step of finding the approximation solution, the solution is calculated as a linear combination of the preconditioned vectors z_i. Algorithm 1 computes these in the step $z_j \coloneqq M^{-1}v_j$. Actually this means to solve the preconditioning system:

$$Mz_j = v_j \tag{42}$$

In the Comsol Multiphysics model this is done using a geometric multigrid. If a multigrid has N levels, then the multigrid level with number 0 is the finest level of the multigrid, the level at which the solution is sought. Level N is the coarsest grid. The preconditioning matrix per level is given as M_i and is generated using a coarsening algorithm (M. Comsol, 2020d). The geometric multigrid method has to compute so called prolongation matrices P_i that map the solution z_i of level i to the solution vector $P_i z_i$ on the next finer level $i-1$. The prolongation matrices use plain interpolation from one level to another. Keep in mind that the indices i now specify the multigrid level and not the iteration step in the GMRES. We will consider a two level multigrid so N=1.

In the multigrid algorithm M_i is the precondition matrix at level i, $z_{j,i}$ is the approximation at level i. In the algorithm the term $z_{j,1}$ is known as the coarse grid correction as this is the correction added to the initial iterate $z_{j,0s}$ after solving the coarser grid.

Algorithm 2: The Geometric Multigrid algorithm

1. Choose an initial solution $z_{j,0}$ to the system $M_0 z_j = v_j$
2. Apply a few iterations of presmoother to the linear system $M_0 z_j = v_j$ starting with initial solution $z_{j,0}$ to obtain a more accurate iterate $z_{j,0s}$. This can be done using the simple iterative algorithm SOR.
3. Compute the residual $r_0 = v_j - M_0 z_{j,0s}$
4. Project the residual onto level 1 by $r_1 = P_1^T r_0$
5. Solve $M_1 z_{j,1} = r_1$. Typically a direct solver is used, we will consider MUMP.
6. Map $z_{j,1}$ to level 0: $z_{j,0c} = z_{j,0s} + P_1 z_{j,1}$
7. Apply a few iterations of postsmoother to the system $M_0 z_j = v_j$ starting with $z_{j,0c}$ to obtain a more accurate iterate $z_{j,0mg}$. This is again done with the SOR iteration method

In the last line the output of the multigrid algorithm $z_{j,0mg}$ is obtained. In the algorithm the direct solver MUMPS is used. The MUMPS method is conveniently used to solve the system of equations on a coarser grid. The decreased amount of degrees of freedom make the direct solver more efficient. The MUMPS method is a frontal solver meaning that it handles sparse matrices efficiently by avoiding operations involving zero terms.

Also the iterative succesive over-relaxation (SOR) method is mentioned working as a pre- and postsmoother. Essentially, a presmoother improves the initial solution and the postsmoother improves the final approximated solution. The SOR iterative method is a modification of the general iterative method. Suppose we have the system $Ax = b$ with $A = M - N$. Then the general iterative method is defined as:

$$x^{k+1} = M^{-1} N x^k + M^{-}1b \tag{43}$$

M is not the preconditioning matrix but an easily invertible matrix. M is used by convention. If we split matrix A as $A = D + L + U$ where D is the diagonal matrix, L is the lower triangle matrix and U is the upper triangle matrix. The SOR iterative scheme then becomes:

$$x^{k+1} = (D + \omega L)^{-1} \left(\omega b - [\omega U - (\omega - 1)D] x^k\right) \tag{44}$$

where $\omega > 1$ is the relaxation factor.

3.7 Shifted laplacian preconditioner

To show a glimpse of an innovation that put the Delft University of Technology on the map, we would like to briefly mention the shifted laplacian preconditioner. The idea is that a problem with no or slight damping with the system of equations $Ku = b$ will be preconditioned with a preconditioning matrix M which has more damping. A problem with damping converges faster. The shifted laplacian preconditioner uses the discretization of the Helmholtz equation, like equation 11, with a complex shift defined as:

$$(\nabla^2)E + (k^2 + j\eta)E = 0 \tag{45}$$

Where η is the added complex shift. Note that this equation is similar to the Helmholtz equation 13 in a material with non-zero conduction, and so damping. We would have $\tilde{k}^2 = k^2 + j\eta$, where $\tilde{k}^2 = \mu\epsilon\omega^2 + j\mu\sigma\omega$.

Now instead of solving the system of equations $Ku = b$, we will solve $M^{-1}Ku = M^{-1}b$, where the shifted laplacian preconditioning matrix M is in left-precondition mode. The GMRES works well for this problem whenever $||I - M^{-1}K||_2$ is sufficiently small, where I is the identity matrix. M^{-1} is usually replaced with an approximation that is easy to compute, say M_e^{-1}. We then have the system of equations:

$$M_e^{-1}Ku = M_e^{-1}b \tag{46}$$

For an efficiently working GMRES we then require $||I - M_e^{-1}K||_2$ to be small. $I - M_e^{-1}K = I - M_e^{-1}M + M_e^{-1}M(I - M^{-1}K)$, so we require both $||I - M_e^{-1}M||_2$ and $||I - M^{-1}K||_2$ to be small. Essentially, M^{-1} should be a good preconditioner for K and M_e^{-1} should be a good preconditioner for M. These two conditions have somewhat conflicting interests. The first preconditioner would be optimal whenever $M^{-1} = K^{-1}$. In this situation there is zero conductivity σ, so no imaginary shift. The second condition requires an efficient preconditioner of M. This raises the need for a non-zero conductivity σ. A larger non-zero conductivity has the effect of low oscillatory behaviour of the shifted problem, thereby being cheaper to create a good approximation for (Gander, Graham, & Spence, 2015).

As intermediate step of showing the effectiveness of the shifted laplacian preconditioner, we will illustrate a why a damped problem is more easily solvable (faster GMRES convergence). The fast convergence of the GMRES is due to the effectivity of introducing an imaginary shift to the Helmholtz equation. To show this effectivity, we will make use of the analytical solution of the 2D problem considered in subsection 2.8. We found an exact expression for the solution of the problem combining the calculated eigenfunctions and eigenvalues. We found that the eigenvalues are given by $\lambda_{nm} = \left(\frac{n\pi}{a}\right)^2 + \left(\frac{m\pi}{b}\right)^2 - (\tilde{k})^2$.

The value of k is a real number for zero conductivity. For non-zero conductivity however, it is a complex number which again we will denote with $\tilde{k}$. $\tilde{k}$ is defined as $\tilde{k}^2 = \mu\epsilon\omega^2 + j\mu\sigma\omega$, where μ and ϵ are the relative permeability and relative permittivity respectively. ω is the angular frequency, j is the imaginary unit $\sqrt{-1}$ and σ is the electrical conductivity.

The eigenvalues for the solution of the problem described in subsection 2.8 are plotted in figure 59 in the appendix. In plotting the eigenvalues, we assume dimensions $(a \times b) = (\pi, \pi)$ m and $\epsilon = \mu = \omega = 1$. The eigenvalues are then given by:

$$\lambda_{nm} = n^2 + m^2 - (1 + j\sigma) \tag{47}$$

In the plot we let n and m go from from 1 to 10 as increasing these will only show an increase in real part of the eigenvalue. Furthermore, the analytical solution which consists of infinite eigenvalues will have a decreasing contribution from the eigenfunctions corresponding to eigenvalues of increasing magnitude, large n and m, as shown by equation 28. The eigenvalues are plotted for multiple values of the electrical conduction σ.

The electrical conductivity, directly proportional to the imaginary total permittivity, signifies an added damping to the domain. σ of zero is a situation without damping, and non-zero conductivity will have damping. This is an important property, because figure 59 shows us that

the eigenvalues shift away from the origin as damping is increased. The origin in the complex plane signifies resonance, an important physical phenomena which is difficult to simulate. In the analytical solution an eigenvalue near the origin would increase the contribution of the corresponding eigenfunction significantly. Increasing the damping by increasing σ would therefore increase banality of the problem making it easier to simulate. So, the added imaginary shift in the Helmholtz equation makes it easier to solve.

4 Implementation

Comsol Multiphysics, a finite-element based modelling environment, will be used to produce a proper pre-characterization numerical model capable of calculating the electric field within a rectangular reverberation chamber at low-end frequencies. To explore the accuracy of such model it is important to gradually build up this complex system. In this way, errors in the model can be more easily detected thereby increasing reliability of the results. A reverberation chamber is a complex system containing a rectangular reflective room, a mode-stirrer and an antenna exciting the chamber. The first model will contain just an antenna. This model will thereafter be extended to an antenna inside a reflective shielded chamber. The shielded chamber at Comtest will be reconstructed for this. At last the model will be modified and expanded to represent the reverberation chamber at Comtest with a Z-fold stirrer as mode-stirrer. For physical completeness the shielded chamber model will be considered with an added dielectric object to study the behaviour of electromagnetic waves in an environment with a dielectric object. To explore the convergence with shifted laplacian precconditioning, the setup for this model will also be discussed at the end of this chapter.

4.1 General Model properties

To create a model in Comsol Multiphysics it is important to know about the possibilities and the way it works. For this purpose we used Comsol Multiphysics tutorials to get acquaintances with the solver. These tutorials will not be explicitly described but can be found on (M. Comsol, 2020a).

Comsol Multiphysics has divided the modelling process into 4 major nodes. These are again divided into sub-nodes as shown in figure 11. The major nodes are: Global Definitions, Component 1, Study 1 and Results. The first node is used for global definitions and parameters that are to be used throughout the model. These can be called on everywhere in the model.

The next node is where the modelling starts. The node called Component 1 contains all information about the shape, material, physics and mesh of the created geometry. In Geometry 1 the entire geometry of the model is defined. In this thesis those will be an antenna, an antenna in a shielded chamber with and without an extra dielectric object and a reverberation chamber with antenna and z-fold stirrer. Comsol Multiphysics has a wide range of options for creating a geometry. These include basic geometrical entities like blocks, cones, cylinders, etc but it also includes options like importing objects, automatic reparation and extruding 2D objects. A material can be defined on a domain, boundary, edge or point in the modelled geometry. This is done under the corresponding material sub-node. The sub-node Electromagnetic Waves, Frequency Domain applies the physics to the modelled geometry. It asks for the to be solved partial differential equation on the modelled domain, which in this case is the electromagnetic wave equation. Furthermore, it allows you specify the order of discretization for the problem which is by default quadratic. This is also the place to specify boundary conditions to specific surfaces, edges and points. In this thesis the perfect electrical conductor, impedance boundary, lumped port and lumped element are considered. The last two will be discussed below in subsections 4.2 and 4.3. Lastly the initial values can be set in this sub-node.

Additionally, the Component 1 node includes the Mesh 1 sub-node. As expected from the name, this is where the mesh is generated for the modelled geometry. One can choose for the mesh to be modelled automatically by Comsol based on the included physics and the geometry, but one can also build the mesh himself. A physics-induced mesh will work, but a user-defined

mesh can be optimized for efficiency and accuracy to the users liking. There are many options for the mesh like mesh size, shape, distribution, etc. For mesh size it is important to keep in mind that the maximum element size is automatically set to 1/5 of the vacuum wavelength of the highest studied frequency. This is used to ensure uniqueness of the solution. Different sizes can be enforced on different domains or surfaces to increase detail in places of interest and to decrease detail in less important places for efficiency. As model shape, the model uses free tetrahedral elements for the interior and triangular elements on the boundary. The element order was already defined as quadratic in the Electromagnetic Waves, Frequency Domain sub-node. Examples of the used elements are shown in figure 10.

The third node is the study node. Here the user can again choose for a solver chosen automatically by Comsol Multiphysics but he can also create a solver sequence himself. The chosen solver for the model is chosen to be a GMRES solver with geometric multigrid preconditioning, pre- and post-smoothed by the SOR method. As coarse solver the MUMPS method is used. These are explained in section 3.6. Additionally for the reverberation chamber model there is a parametric sweep sub-node. This makes it possible to solve the problem for different parameter values. In this thesis rotation angles of the mode-stirrer is the parameter. The system is solved for each parameter step in the supplied rotation angle list. Each step of the parametric sweep the new geometry is re-meshed using the supplied meshing requirements and solved using the supplied solver options.

The final node is the Result node. Here all solutions of the study node are saved in data files. In this node the solutions can also be processed to show the required results in tables and plots. Parts of the solution data can be saved as a copy to be able to plot solutions only on this partitioned data set.

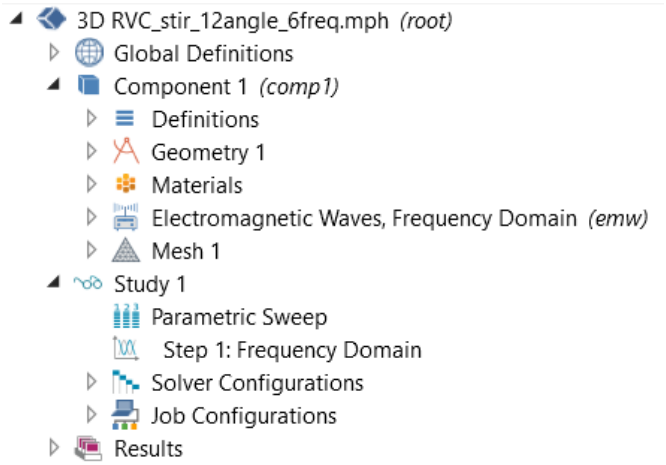

Figure 11: The modelling window as found in Comsol Multiphysics. Component 1 describes the shape, materials, physics and mesh of the created geometry. The study node allows the user to define the domain in which the physics is studied. The parametric sweep subnode allows for the change of a variable during the solve process of the study. The results node is where all solution data sets are stored and where the derived values and plots can be created.

4.2 Biconical antenna

The first model is used to test the antenna properties. More specifically a 3104C Biconical Antenna is modelled. This broadband antenna is omni-directional and operates at lower frequencies (25-200 MHz) (ETS-Lindgren, 2019). As explained in the theory of section 2.7, low frequencies have a lower amount of propagating modes. This makes low frequency environments easier for analysis and are therefore a logical starting point for the model.

The model of the Biconical antenna uses aluminium materials. Figure 13a shows the two conical shaped conductive object connected by a metal rod called a balun. In Comsol Multiphysics a balun is modelled by two conductive rods with a small surface in between. On this surface a lumped port boundary condition is applied. The 2D surface acts as reference plane connecting two conductive surfaces. On this reference plane a uniform potential difference and impedance can be specified from which the current can be calculated. This in turn excites an electric field (H. Zhang, Krooswyk, & Ou, n.d.). The reference plane with the lumped port boundary condition is shown in figure 12.

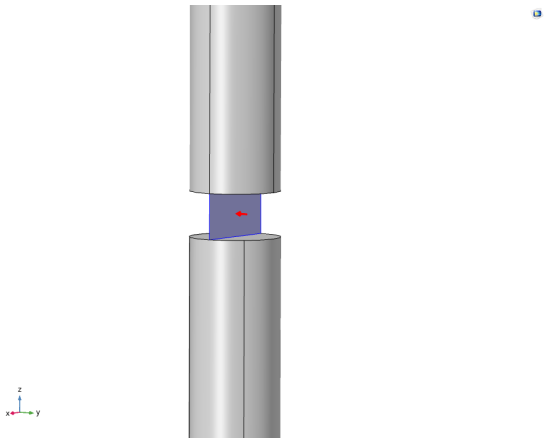

Figure 12: The lumped port boundary condition on the reference plane (Blue) between two conducting rods

Another important concept is the perfectly matched layer environment surrounding the antenna as shown in figure 13b. To model the behaviour of an antenna in the far-field it should not observe any interference by other objects. Yet, it is impossible to model an infinite domain. The solution is to create perfectly matched layers around the antenna. Boundary conditions then ensure that the waves act as if they would go to infinity. This way the behaviour in the far-field can be studied.

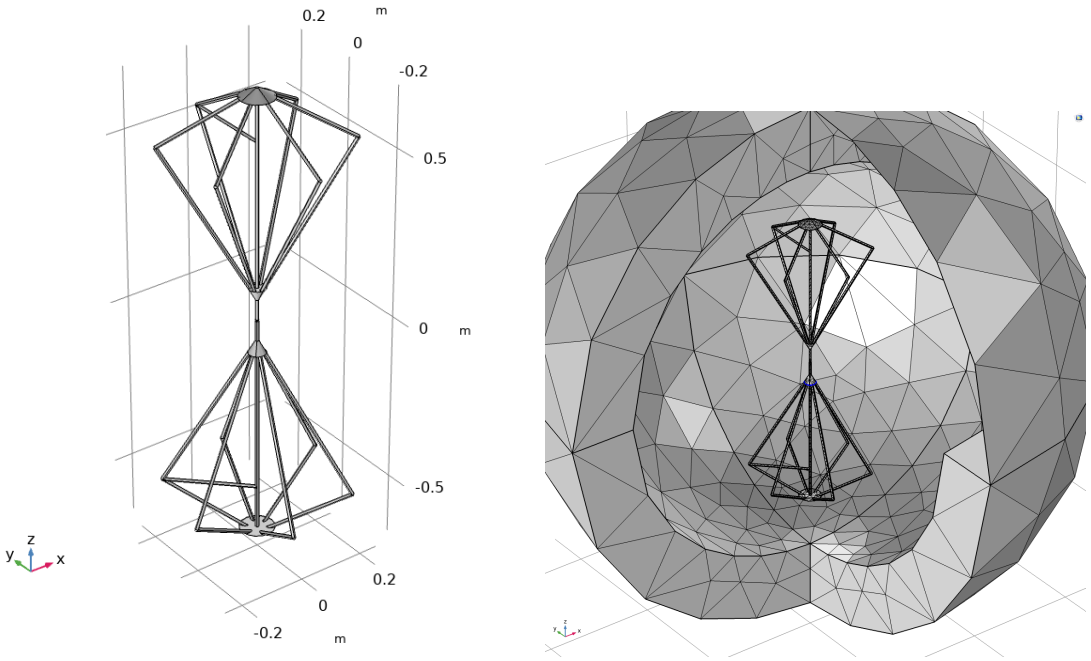

(a) (b)

Figure 13: The modelled 3104c Biconical antenna. Subfigure (a) shos a schematic overview of the antenna and subfigure (b) shows the used mesh for the modelled 3104c Biconical antenna surrounded by perfectly matched layers to model an infinite domain. Note that a part of the perfectly matched layer environment is suppressed in the plot

4.3 Log-periodic dipole array antenna

In reverberation chambers one measures at frequencies above the lowest usable frequency of 200 MHz and higher. This cannot be done with the biconical antenna. Therefore a new model is created of a log-periodic dipole array antenna, LPDA antenna for short. The antenna used in measurements is the 3146a Log-Periodic antenna (ETS-Lindgren, 2010). The antenna operates in the frequency range 200-1000 MHz. The model of the log-periodic antenna is recreated from a model supplied by Comsol Multiphysics and is based on the LPDA antenna used in the measurements (M. Comsol, 2020c).

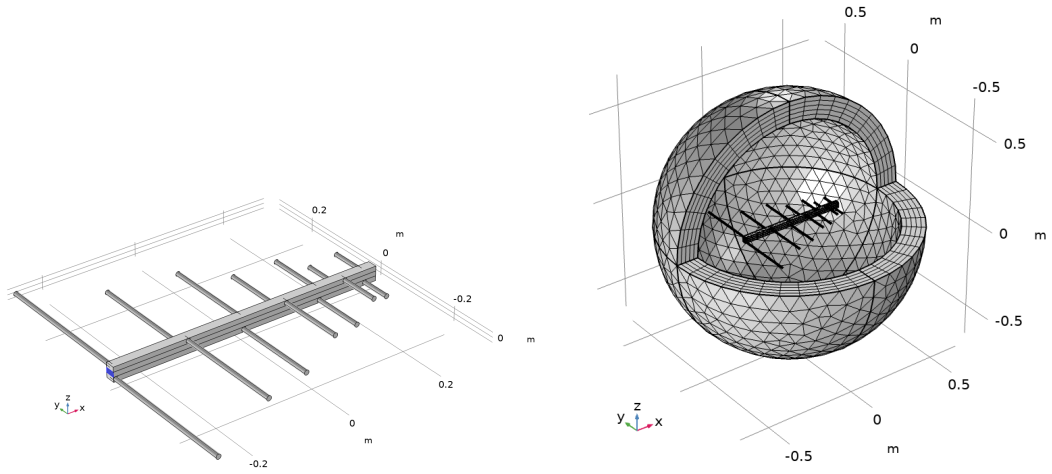

(a) (b)

Figure 14: The modelled 3146a log-periodic dipole array antenna. Subfigure (a) shows a schematic overview of the antenna with in blue the lumped element boundary condition. Subfigure (b) shows the used mesh for the modelled 3146a log-periodic dipole array antenna surrounded by perfectly matched layers to model an infinite domain. Note that a part of the perfectly matched layer environment is suppressed in the plot

Again the perfectly matched layer method is used to model an infinite domain. Also the lumped port boundary condition is used to excite an electric field (figure 15). This time on the exact opposite side of the LPDA a lumped element boundary condition is added. The lumped element acts as a resistor terminating the excitation of the lumped port.

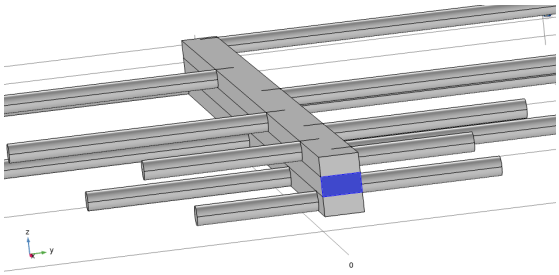

Figure 15: The lumped port boundary condition in Comsol Multiphysics applied on the blue surface. It is located in between two aluminum bars (above and below). The bar in between is modelled as air. On the exact opposite side the lumped element boundary condition terminates the excitation

The next step is modelling the respective antennas in a shielded chamber with the dimensions (4.05 m $\times$ 2.55 m $\times$ 2.925 m). These dimensions correspond to the shielded chamber located at Comtest, Zoeterwoude. A shielded chamber is essentially a reverberation chamber without incorporated mode-stirrer, so a simple metal cavity. The shielded chamber models and measurements are used as intermediate step in creating a reverberation chamber pre-characterization model. This way it is easier to analyse potential errors in the model before handling the most difficult geometry.

4.4 Shielded chamber with biconical antenna

The measurement setup was first created in the Comtest shielded chamber and thereafter modelled in Comsol Multiphysics. The shielded chamber has dimensions (4.05 m × 2.55 m × 2.925 m). This modelling order was chosen due to the limitations of the measurement setup. The biconical antenna was attached to a wooden tripod. The antenna was attached to the tripod with a plastic clamp. It was found easiest to level the antenna first and replicate it in the way shown in figure 16a. The middle point of the biconical antenna, the middle of the balun, lies at the coordinates $(x, y, z) = (1.215, 1.37, 1.39)$ m. These seemingly random coordinates were measured after the placement of the antenna due to difficulty levelling an antenna attached to a tripod. The tripod which has long legs, taking up more room than the antenna, was chosen to stand in one side of the room to keep the rest of the room available for the probe setup. This setup will be explained in more detail in section 4.9. Figure 16b shows that the elements near the antenna are meshed so finely that the antenna appears to be entirely black as opposed to the exterior walls that are meshed much coarser.

The boundary conditions assumed in this model are the lumped port for excitation, PEC and impedance boundaries. The lumped port is applied in the same way as it was in section 4.2. The antenna is made of aluminum, therefore the boundaries of the biconical antenna have added impedance boundary conditions. Comsol Multiphysics uses the permittivity, permeability and conductivity, from the material sub-node, in the impedance boundary. The exterior walls which are made of a good conducting steel composite are assumed to have perfect electronic conductor boundaries. The reason to choose PEC boundaries is to keep the model as simple as possible.

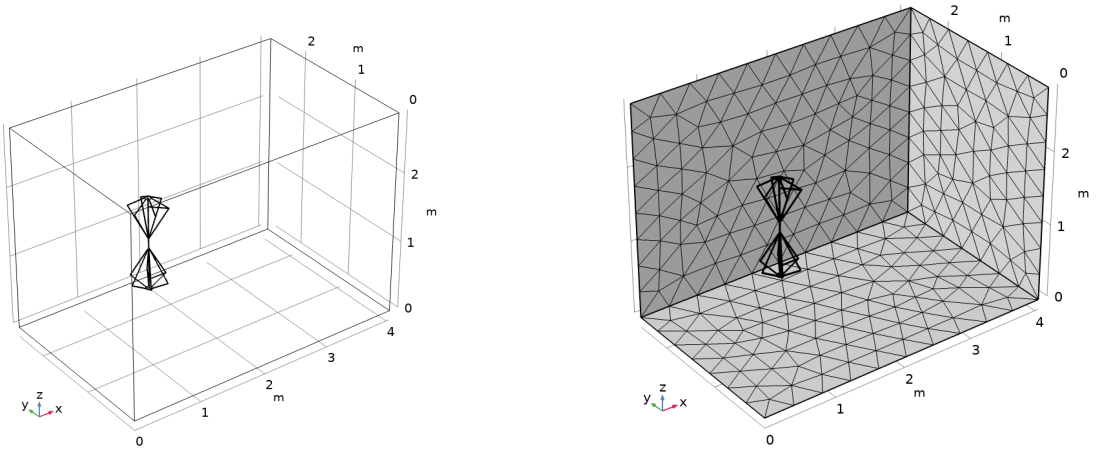

(a) (b)

Figure 16: The modelled biconical antenna in the Comtest shield chamber with dimensions (4.05 m × 2.55 m × 2.925 m). Subfigure (a) shows the schematic overview of the shielded chamber with biconical antenna. Subfigure (b) shows the used mesh for the modelled shielded chamber with biconical antenna. Note that three surfaces of the chamber are suppressed for visualization purposes

4.5 Shielded chamber with log-periodic dipole array antenna

The same Comtest shielded chamber (4.05 m × 2.55 m × 2.925 m) is considered as before in this model, though now a log-periodic dipole array antenna is used. The model was, like before, created after the measurement setup was created in the shielded chamber at Comtest. Again a tripod was used to hold up the log-periodic antenna. This time the position of the middle of the antenna is located at $(x, y, z) = (1.56, 1.435, 1.205)$ m. The antenna is visualised in blue in figure 17b to make it more distinguishable with the meshed background. Note that the mesh is denser due to the higher studied frequencies.

The boundary conditions used in the model are the lumped port and element, the impedance boundary condition and the PEC boundary condition. The lumped port and element are applied in the same way as explained in section 4.3. The antenna is made of aluminum and is therefore chosen to have impedance boundary conditions. For the same reason as before in section 4.4, the exterior walls are assumed to have perfect electric conducting boundaries.

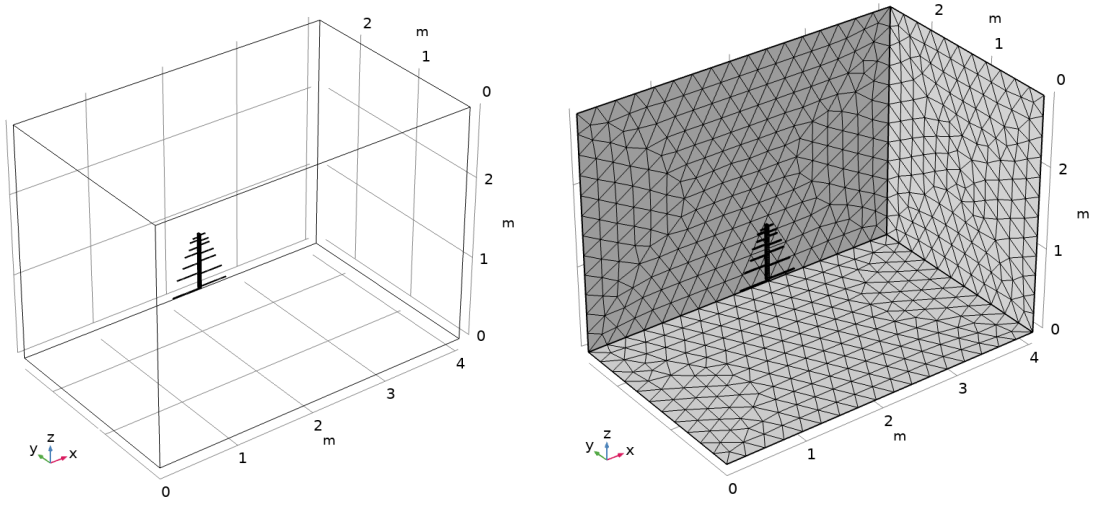

Figure 17: The modelled 3146a log-periodic dipole array antenna in the Comtest shield chamber (4.05 m × 2.55 m × 2.925 m). Subfigure (a) shows a schematic overview of the shielded chamber setup with log-periodic dipole array antenna. Subfigure (b) shows the used mesh for the antenna in the Comtest shielded chamber. Note that three surfaces of the chamber are suppressed for visualization purposes

The next two sub-sections will consider an extra dielectric object in the previously discussed shielded chamber environment. The added object is called a load. The models of these loaded chambers are not an intermediate step to create the reverberation chamber model, but are added out of interest and physical completeness of studying the effect of adding a load to a shielded chamber environment. Also, the behaviour of electromagnetic waves near a dielectric medium can be observed.

4.6 Shielded chamber with biconical antenna and dielectric object

This model included the biconical antenna, the shielded chamber and an added dielectric object. The middle point of the biconical antenna is located at $(x, y, z) = (1.215, 1.37, 1.39)$ m. This is replicated from the measurement setup in the Comtest chamber (4.05 m $\times$ 2.55 m $\times$ 2.925 m). Adding a dielectric object to the shielded chamber has an influence on the electric field inside the chamber dependent on the material and dimensions of the object. As discussed in section 2.4 and 2.5 the reflectivity coefficient increases for increasing refractive index thus for increasing relative permittivity. Reflectance can also decrease if the magnetic permeability of the second domain is increased. The absorption increases for increasing imaginary wavenumber thus for increasing imaginary part of the permittivity as shown by equation 14b. Water was used as dielectric object for its easy accessibility, unit relative permeability, high real permittivity and smaller imaginary permittivity. As the permittivity is frequency dependent an interpolation/extrapolation plot was made using data from an article on the frequency dependency of the permittivity of water at $20°C$ (Kaatze, 1989). The interpolation is piecewise cubic and the extrapolation is to nearest function. The plots for the real and imaginary permittivity are shown in the appendix in figures 60a and 60b respectively. The reflectance allows us to observe a change in the electric field inside the shielded chamber as an effect of the added water tank.

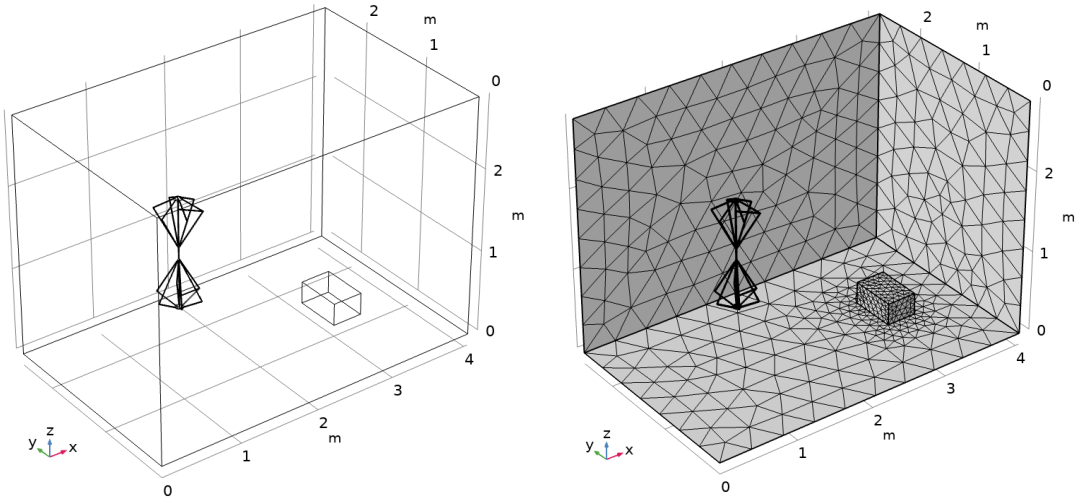

Figure 18: The modelled biconical antenna in the Comtest shield chamber (4.05 m $\times$ 2.55 m $\times$ 2.925 m) with dielectric object. The loading is a container filled with tap-water. The inner dimensions of which are (0.37 m $\times$ 0.565 m $\times$ 0.27 m). The lower right corner of the container is located at $(x, y, z) = (3, 1, 0)$ m. Subfigure (a) shows the schematic setup and subfigure (b) shows the meshed used for the setup. Note that three surfaces of the chamber are suppressed for visualization purposes. Also the mesh is denser in the water tank due to the smaller wavelengths

The plastic container holding the water together has been ignored in the model as its effect on the absorption can be neglected. The inner dimensions of the container are (0.37 m $\times$ 0.565 m $\times$ 0.27 m). The lower right corner of the container is located at $(x, y, z) = (3, 1, 0)$ m. This is to ensure space in the middle for the measuring equipment. The boundary conditions for the aluminum antenna are impedance boundary conditions and the walls are again PEC boundaries.

The mesh is finer in the water domain because of smaller wavelengths in water and to better see the behaviour of the electric field in this domain.

4.7 Shielded chamber with log-periodic dipole array antenna and dielectric object

This model includes a log-periodic dipole array (LPDA) antenna, the shielded chamber and a dielectric object. The middle of the LPDA antenna is located at $(x, y, z) = (1.0, 1.275, 1.45)$ m. This time a different orientation of the antenna is used to model test the reliability of the model for different situations. The shielded chamber again has dimensions (4.05 m $\times$ 2.55 m $\times$ 2.925 m). The dielectric object is chosen to be a container filled with tap-water for the same reasons as stated in the previous subsection. The inner dimensions of the water filled container are (0.37 m $\times$ 0.565 m $\times$ 0.27 m). The lower right corner of the container is located at $(x, y, z) = (3, 1, 0)$ m. The relative permeability of water is taken to be 1 and the real and imaginary relative permittivity can be found in figures 60a and 60b in the appendix.

The boundary conditions used in the model are impedance boundaries for the aluminum antenna and PEC boundary conditions for the exterior walls. The system is again excited by the lumped port-element combination like before. Note that the mesh is denser in the dielectric object domain, this is because the wavelength of the electromagnetic waves are shorter in the object and because we want to more accurately study the behaviour of the electric field in this domain. The used setup is shown in figure 19.

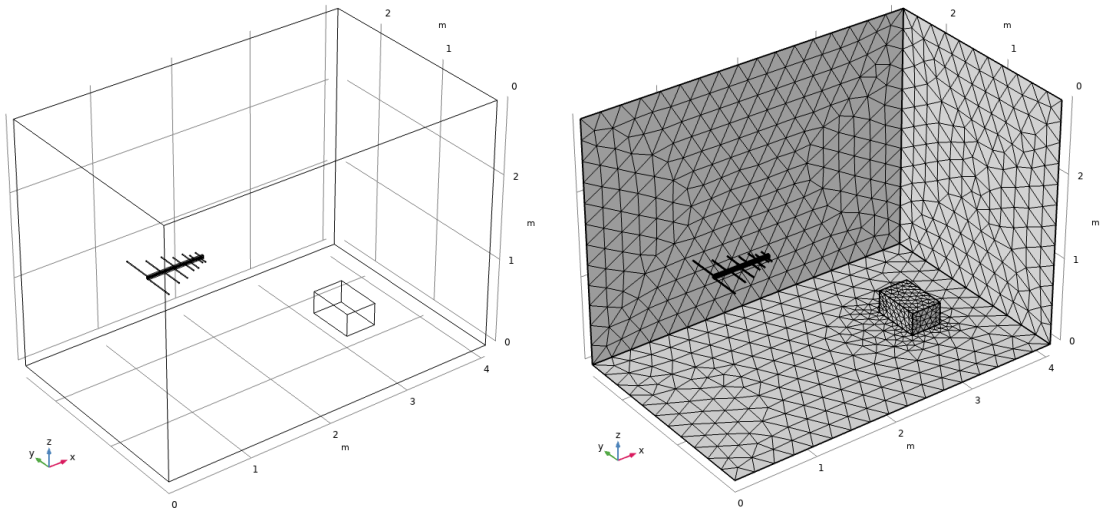

(a) (b)

Figure 19: The modelled 3146a log-periodic dipole array antenna in the Comtest shield chamber (4.05 m $\times$ 2.55 m $\times$ 2.925 m) with dielectric object. The object is a container filled with tap-water. The inner dimensions of which are (0.37 m $\times$ 0.565 m $\times$ 0.27 m). The lower right corner of the container is located at $(x, y, z) = (3, 1, 0)$ m. Subfigure (a) shows the setup used in the model and subfigure (b) shows the mesh in the model. Note that three surfaces of the chamber are suppressed for visualization purposes. The mesh is denser in the object due to smaller wavelengths

4.8 Reverberation chamber with z-fold stirrer

The final model is a model of the reverberation chamber located at Comtest, Zoeterwoude. This is the last step in the modelling process aimed to produce a pre-characterization model of a reverberation chamber. The dimensions of the reverberation chamber are (5.03 m × 3.97 m × 2.85 m). This is bigger than the shielded chamber considered before. The reverberation chamber at Comtest includes a z-fold stirrer as mode-stirrer. The stirrer is placed in a corner of the chamber The included log-periodic dipole array (LPDA) antenna is placed in the corner closest to the stirrer. This keeps the working volume the largest. A log-periodic dipole array antenna is used in this situations because frequencies from 200-300 MHz are used. The middle of the antenna is located at $(x, y, z) = (1.20, 3.12, 1.55)$ m.

Both the antenna and stirrer are made of aluminum. For this reason they are modelled with the impedance boundary condition. The exterior walls again have the PEC boundary condition. The field is excited by a lumped port-element combination as explained in section 4.3.

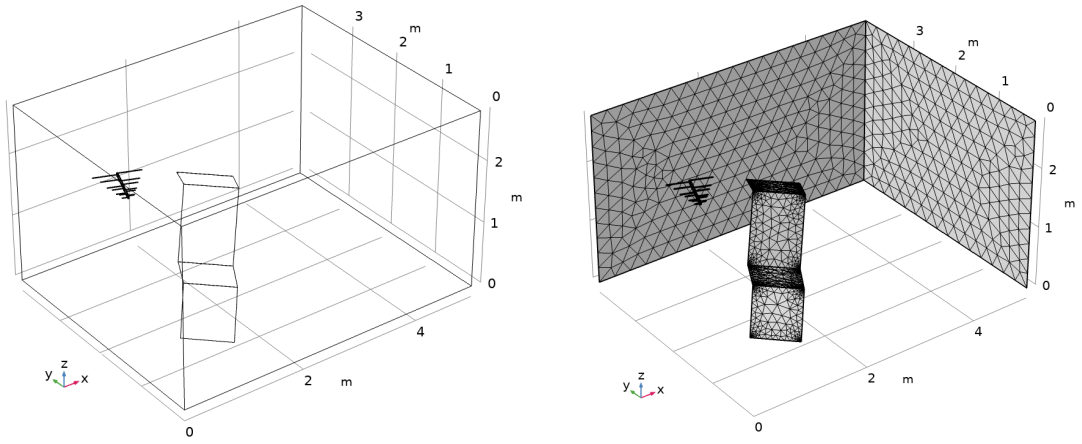

(a) (b)

Figure 20: The modelled 3146a log-periodic dipole array antenna in the Comtest reverberation chamber (5.03 m × 3.97 m × 2.85 m) with the Z-fold stirrer in its initial position. The antenna is located at $(x, y, z) = (1.20, 3.12, 1.55)$ m and the Z-fold stirrer in the neares corner. The model setup is shown in subfigure (a) and the model mesh is shown in subfigure (b). Note that four surfaces of the chamber are suppressed for visualization purposes

4.9 Data acquisition

To confirm the models described above the results of the respective models are compared to measurements of the same setup at Comtest. As mentioned before the setup at Comtest uses either a 3104c biconical antenna or a 3146a log-periodic dipole array antenna. The power of these antennas are supplied by a Marconi 2024 generator amplified by a AR25W1000M7 amplifier. Also a Boonton 5232 RF power meter was used in the reverberation chamber measurements. The power input, antenna and power meter are coupled with a Kalmus c2630 coupler. At last an ETS Lindgren HI-6053 electrical field probe is used to measure the electric field. This field probe is directly connected to a computer running Comtest EMC measuring software. The cables connecting the probe to the computer are made of optical fibre and are neglected in the model.

The electrical field probe was placed upright on mount on a long vertical pole such that the height was easily adjustable. To keep the pole upright it was clamped on a stand at the bottom. The clamping of the pole by the stand restricts the adjustability of the mounted probe. Therefore the probe cannot measure the electric field below 0.9 meter in the z-direction. Additionally the stand at the bottom limits the maneuverability of the field probe. This makes measuring close to exterior walls or interior objects impossible.

Taking these limitations into consideration, the solutions to the modelled problems in the shielded chamber were analysed. The reliability of the model is tested by comparing the electromagnetic wave pattern calculated by the model to the measured electromagnetic field in the Comtest chamber. In the model, slices of the electric field were analysed to find a distinguishable pattern. For various frequencies the most distinct field patterns were searched for in cross-sections of the shielded chamber to test multiple modelled frequencies on their reliability. After finding distinguishable cross-sections the measuring points were determined in Comsol Multiphysics taking the measuring limitations in regard. The electric field value in each direction and the electric field norm from the model could be immediately exported to Matlab for analysis. The measured electric field values and electric field norm were written down for each point in the chamber as well. Each point had to be measured separately and the probe had to be moved manually from one point to another.

The measured electric field values were only measurable for electric field values above 2 V/m, under this threshold there was to much noise influence. Therefore amplification was used to increase the electric field at frequencies that required it. This means that the power was not kept constant during the measurements. Since the power could easily be changed in the model as well, it was decided to only compare the field pattern from the model and the measurements. As the power in the model was kept constant, the measured electric field values were normalised. The highest measured electric field value was chosen and divided by the electric field at that same point in the model. The constant that followed divides all measurement values of that frequency. In this way the maximum value of the model and normalised measurements will be the same.

The model of the reverberation chamber is compared to the reverberation chamber at Comtest using a chamber field uniformity plot. Data acquisition is done according to the method supplied by IEC 61000-4-21. The setup is the same as in the shielded chamber, however now the Z-fold stirrer is added. The measurement points are at the 8 vertices of the working volume. The working volume was defined as 0.8 m from all walls and objects. Measurement will be done for 6 frequencies linearly spaced between 200-300 MHz. 4 and 12 stirrer rotation positions will be considered. At each of the 8 points the electric field is measured for all frequencies and stirrer positions. The same is done for the model. The acquired model and measurement data can now be used to calculate field uniformity. The following procedure is exactly as described in IEC 61000-4-21 (International Electrotechnical Commission & Technical Committee 77, 2011).

First the maximum of the E-field at each probe position is found over all stirrer rotation positions. This is done for all E_x,E_y and E_z at each frequency. These maxima are then normalised by dividing them by the root of the input power:

$$\ddot{E}_{x,y,z} = \frac{E_{Max\ x,y,z}}{\sqrt{P_{input}}} \tag{48}$$

where $E_{Max\ x,y,z}$ is the maximum of the E-field (V/m) of each probe axis across all generated

stirrer positions. $\ddot{E}_{x,y,z}$ is the normalized maximum field (V/m) and P_{input} is the average input power to the chamber during the stirrer rotation at which $E_{Max\ x,y,z}$ was recorded.

Thereafter, the average of the normalized maximum values across the probe positions is calculated for each validation frequency and each probe axis of the E-field probe.

$$\langle \ddot{E}_x \rangle_8 = \frac{\left(\sum \ddot{E}_x \right)}{8} \tag{49a}$$

$$\langle \ddot{E}_y \rangle_8 = \frac{\left(\sum \ddot{E}_y \right)}{8} \tag{49b}$$

$$\langle \ddot{E}_z \rangle_8 = \frac{\left(\sum \ddot{E}_z \right)}{8} \tag{49c}$$

Similarly the average of the normalized maximum of all the E-field probe measurements is calculated giving equal weight to each axis:

$$\langle \ddot{E} \rangle_{24} = \frac{\sum \ddot{E}_{x,y,z}}{24} \tag{50}$$

The field uniformity is defined by IEC 61000-4-21 as follows, "The field uniformity is specified as a standard deviation from the normalized mean value of the normalized maximum values obtained at each of the eight locations during one rotation of the tuner. The standard deviation is calculated using data from each probe axis independently and the total data set." The standard deviation is given by:

$$\sigma_x = \sqrt{\frac{\sum \left(\ddot{E}_{x,i} - \langle \ddot{E}_x \rangle_8 \right)^2}{7}} \tag{51}$$

Here $\ddot{E}_{x,i}$ is the individual measurement of the x-vector, $\langle \ddot{\mathrm{E}}_x \rangle_8$ is the arithmetic mean of normalized $E_{Max\ x}$ vectors for all eight measurement locations. σ_x is the standard deviation for the x axis. The same can be done for the y and z direction. For the norm, the standard deviation is defined as:

$$\sigma = \sqrt{\frac{\sum_{m=1}^{8} \sum_{n=1}^{3} \left(\ddot{E}_{m,n} - \langle \ddot{E} \rangle_{24} \right)^2}{23}} \tag{52}$$

where $\ddot{E}_{m,n}$ is the individual measurements of all vectors (m = probe locations 1 through 8 and n is the probe direction x, y and z). $\langle \ddot{E} \rangle_{24}$ is the arithmetic mean of the normalized vectors $E_{Max\ x,y,z}$ vectors from all 24 measurements. σ is the standard deviation for all vectors x,y and z.

The previously calculated standard deviations signifying the field uniformity are expressed in V/m, like the electric field. By convention the field uniformity is expressed in dB to compare electromagnetic compatibility results. (International Electrotechnical Commission & Technical Committee 77, 2011) uses the previously calculated standard deviation and the arithmetic mean to formulate the standard deviation in dB as follows:

$$\sigma(dB) = 20\log_{10} \left(\frac{\sigma + \langle \ddot{E}_{x,y,z} \rangle}{\langle \ddot{E}_{x,y,z} \rangle} \right) \tag{53}$$

4.10 Shifted laplacian preconditioner setup

Comsol Multiphysics version 5.5 added new preconditioning methods for the pressure acoustics module. The addition of the shifted laplacian contribution to multigrid preconditioners for the pressure acoustic module enables the numerical study of the shifted laplacian preconditioner. This module works with a scalar Helmholtz equation where only the pressure is considered as variable instead of the electric field in the x,y and z direction.

In the last chapter, the theory behind the preconditioner was briefly discussed. As intermediate step in showing the working of the shifted laplacian preconditioning, it was explained why the GMRES is theorised to converge faster for Helmholtz problems with increased damping. The following setup was used to test this theory. The setup is made using the electromagnetic study in the frequency domain just like the previous models. The material in the interior domain has unit relative permeability and permittivity. Only the conductivity will be changed to show the effect of a shift in the Helmholtz equation on the convergence of the GMRES. The setup includes a reflective reverberation chamber (5.03 m $\times$ 3.97 m $\times$ 2.85 m) with log-periodic dipole antenna but without Z-fold mode stirrer. The system is again excited by a lumped port-element combination like all models using the log-periodic dipole array antenna. The frequency is set at 300 MHz. This is the largest frequency considered in this thesis, to allow for the finest mesh and thus the largest amount elements. This setup allows for a computational time in the order of tens of seconds.

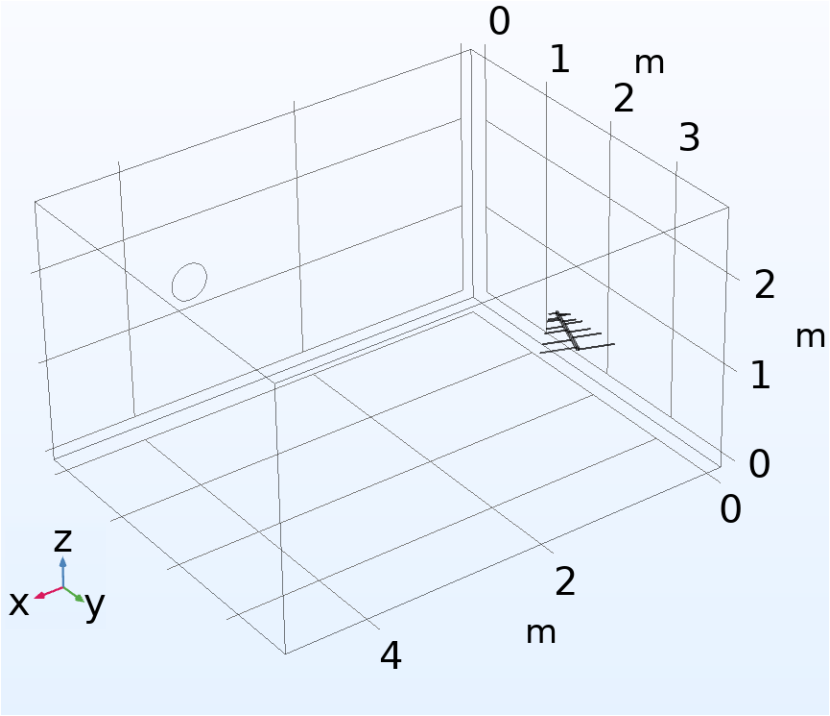

Figure 21: The modelled geometry used in the model showing the convergence of the GMRES for different values of the conductivity and the model showing the convergence for different solvers with and without shifted laplacian preconditioning. The circle on the back wall signifies the placement of a subwoofer exciting the system via a normal acceleration of 1 m/s^2 in the y-direction

To show the effect of adding the shifted laplacian preconditioner on the convergence of the GMRES for a Helmholtz equation with no damping, we build a setup using the pressure acoustic module in Comsol Multiphysics. Similarly this model discussed a Helmholtz equation in the frequency domain, though the dependent variable, pressure, is now scalar. The same model geometry is used as before. The excitation of this system and the addition of the shifted laplacian preconditioner is copied from a tutorial model by Comsol Multiphysics (M. Comsol, 2020b). Instead of exciting the system by a lumped port-element combination, a normal acceleration of 1 m/s^2 in the y-direction is used. The location of this acceleration is shown by the circle in figure 21. The circle signifies a simplified subwoofer as the tutorial model uses. The study considers the problem at 200 Hz which was the highest frequency that the used working computer could solve the problem for in under one hour using the setup as described.

5 Results

This section will show the acquired results from both the models and the measurements. The results are only compared, the discussions of discrepancies are discussed in the next section. Just like the gradual build up of the reverberation chamber, this section will use the order of this build up. Therefore, the first results show the antenna behavior in the form of radiation patterns. The results will start with the low frequencies, so the biconical antenna followed by the higher frequencies with the log-periodic dipole array antenna. The next results are a comparison between the electric field in a shielded chamber with both antennas. The acquisition process of the data is described in the previous chapter. Additionally, there are two subsections that compare the modelled and measured electric field in a shielded chamber with an added dielectric object. This is not part of the build up but added for physical completeness. The final results compare the field uniformity of the modelled reverberation chamber to the field uniformity of the Comtest reverberation chamber.
At last, a convergence plot of the GMRES algorithm with geometric multigrid preconditioning will be shown to support the effectiveness of the shifted laplacian preconditioner.

5.1 Biconical Antenna

The biconical antenna modelled in the far field domain using the perfectly matched layer method in Comsol Multiphysics displays similar behaviour to the measurements of the biconical antenna from the supplying company Schwarzbeck (SCHWARZBECK, 2020a). The 3D radiation pattern is thorus-shaped as expected for an omnidirectional antenna (Balanis & Ioannides, 2007).

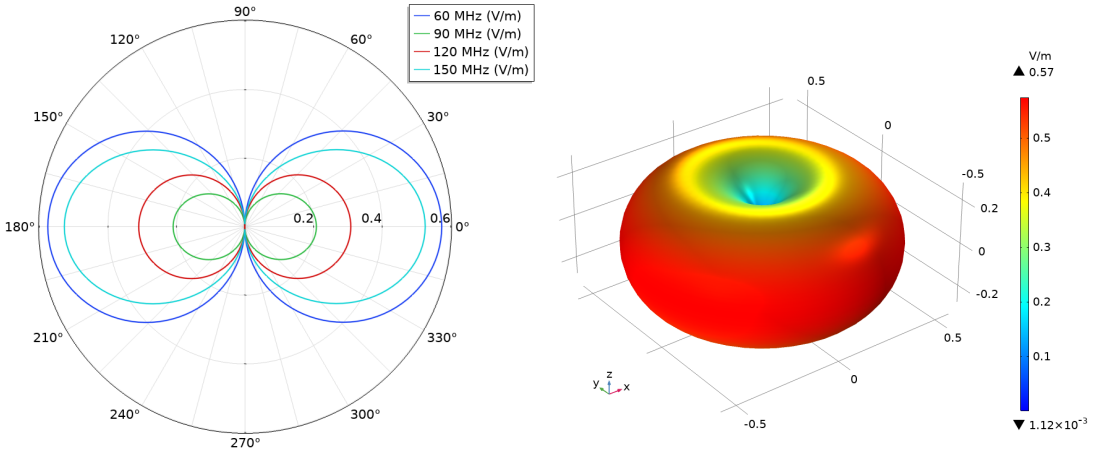

(a) (b)

Figure 22: The radiation patterns of the 4106c biconical antenna. Subfigure (a) shows the 2D radiation pattern for 60, 90, 120 and 150 MHz. Subfigure (b) shows the thorus shaped 3D radiation pattern at 60 MHz

5.2 Log-periodic dipole array antenna

The 2D radiation pattern of the log-periodic dipole antenna calculated using Comsol Multiphysics resembles the 2D radiation pattern as measured by Schwarzbeck (SCHWARZBECK, 2020b) for both low and high frequencies. No such data could be found for the 3D radiation pattern. Though the 3D radiation pattern for high frequencies does show behaviour expected from a directional antenna (Balanis & Ioannides, 2007).

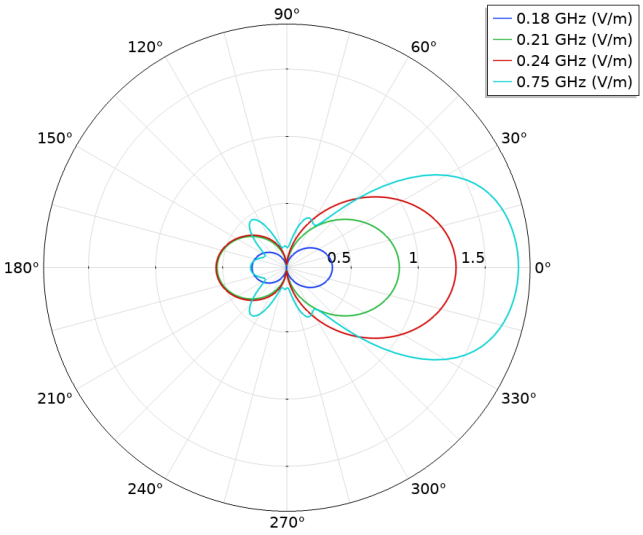

(a)

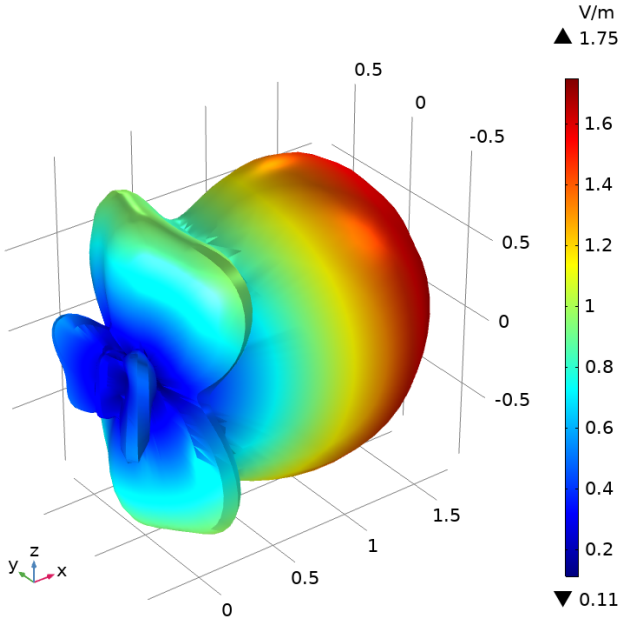

(b)

Figure 23: The radiation patterns of the 3146a log-periodic dipole array antenna. Subfigure (a) shows the 2D radiation pattern for 180, 210, 240 and 750 MHz. Subfigure (b) shows the 3D radiation pattern at 750 MHz

5.3 Shielded chamber with biconical antenna

The modelled biconical antenna is now placed in a shielded chamber (4.05 m × 2.55 m × 2.925 m) with its perfectly conducting surfaces. The setup for these results is shown in section 4.4. As explained in section 4.9 the values are normalised such that the maximal values of the model and measurement are the same.

For 30 MHz it was decided to compare the modelled electric field to the measured electric field at the YZ-slice at $x = 3$ m. This modelled electric field shows a distinct pattern as shown in figure 24. This makes it easy to compare. The black lines in the same figure signify the measurement lines that were chosen. The points on these measurement lines are shown and compared in figures 25a, 25b. Note that figure 24 shows two peaks while figure 25a does not. This is due to a limitation in the measurement setup which only allows values higher than 0.9 m to be measured.

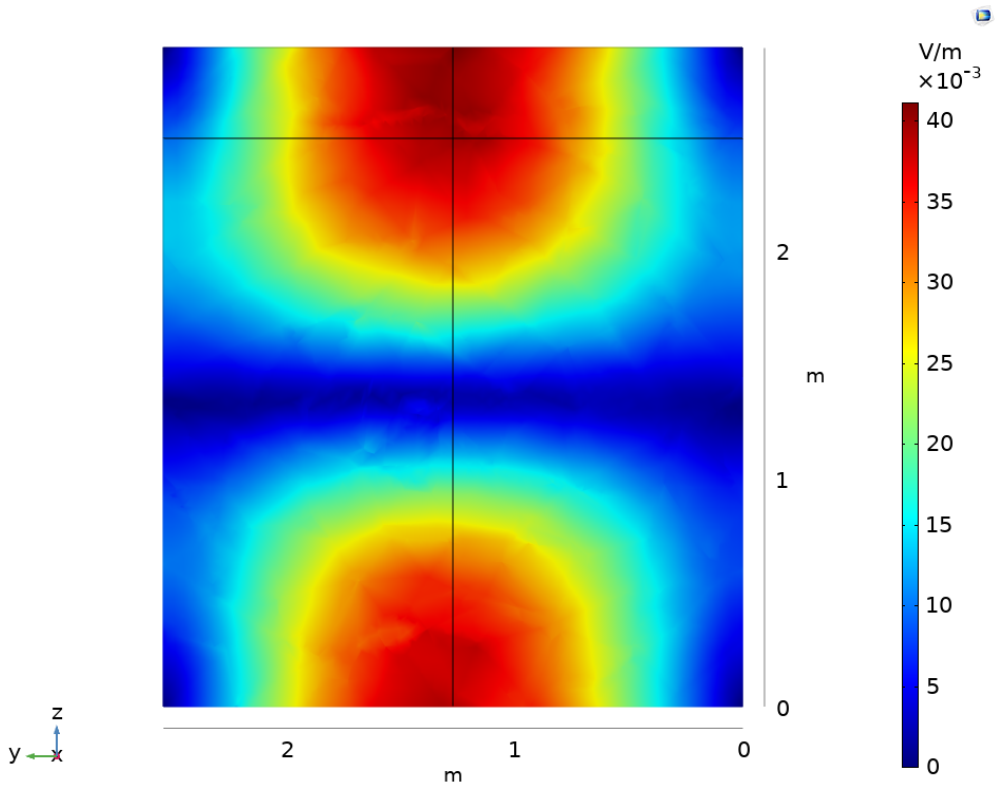

Figure 24: The YZ-plane of the modelled electric field in the shielded chamber with the biconical antenna at 30 MHz. This slice is located at $x = 3$ m. The black lines signify the line-cuts over which measurements were done. Specific points were chosen on these lines which are shown in the next figure 25

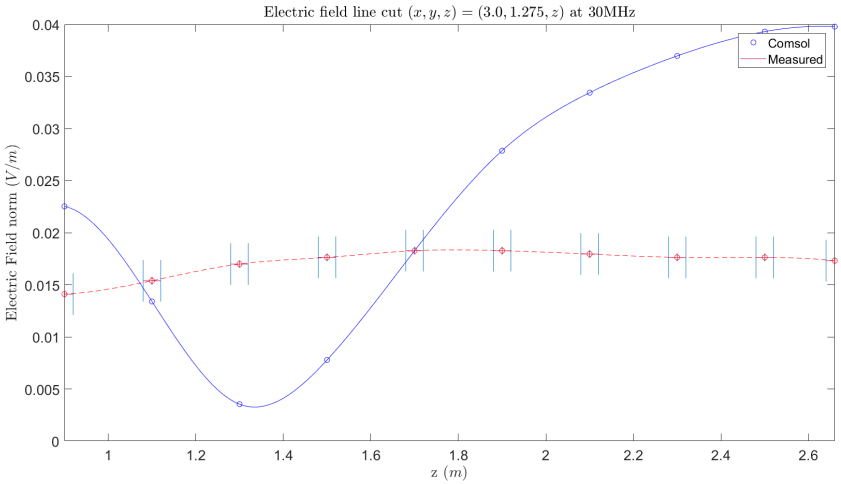

(a)

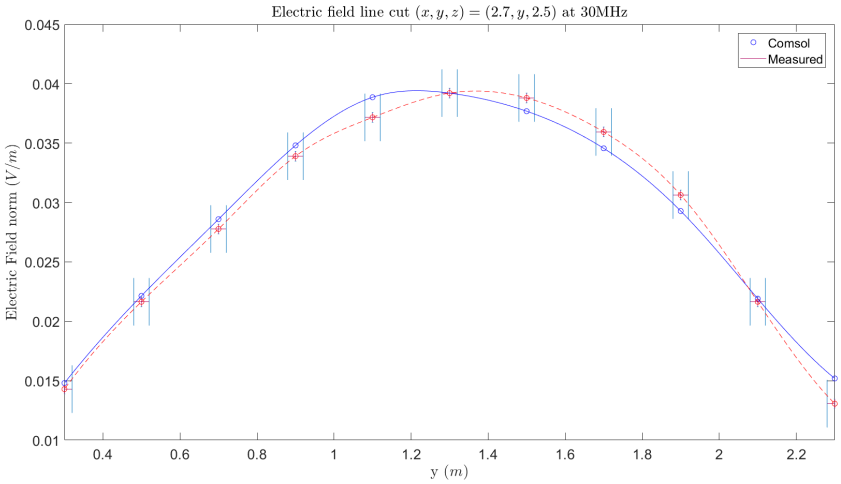

(b)

Figure 25: A comparison of the data points from the biconical antenna model with the measured electric field in the shielded chamber with a biconical antenna at Comtest. The comparison is made for a 30 MHz frequency. The modelled electric field is plotted in blue and the measured electric field is shown in red. The measurements have their respective errors. The vertical error bars are very small and almost not visible. These are errors after normalisation. The horizontal error bars are due to possible probe placement errors. Subfigure (a) shows the electric field over the linecut $(x, y, z) = (3.0, 1.275, z)$ m, which is the vertical line in the previous figure. Subfigure (b) shows the electric field over the linecut $(x, y, z) = (3.0, y, 2.5)$ m, which is the horizontal line in the previous figure

Even though figure 25b seems to model represent the measurements quite well, it is clear from figure 25a that the model does not accurately predict the electric field at 30 MHz. Where the model predicts two peaks at the line $(x, y, z) = (3.0, 1.275, z)$ m, the measured the electric field is more or less constant at this line. Possible explanations for this discrepancy are explained in the next section.

At 60 MHz the modelled electric field shows a distinct pattern in the YZ-plane at $x = 2.7$ m. This pattern is shown in figure 26. Again the black lines in the same figure signify the measurement lines that were chosen. The points on these measurement lines are shown and compared in figures 27a, 27b.

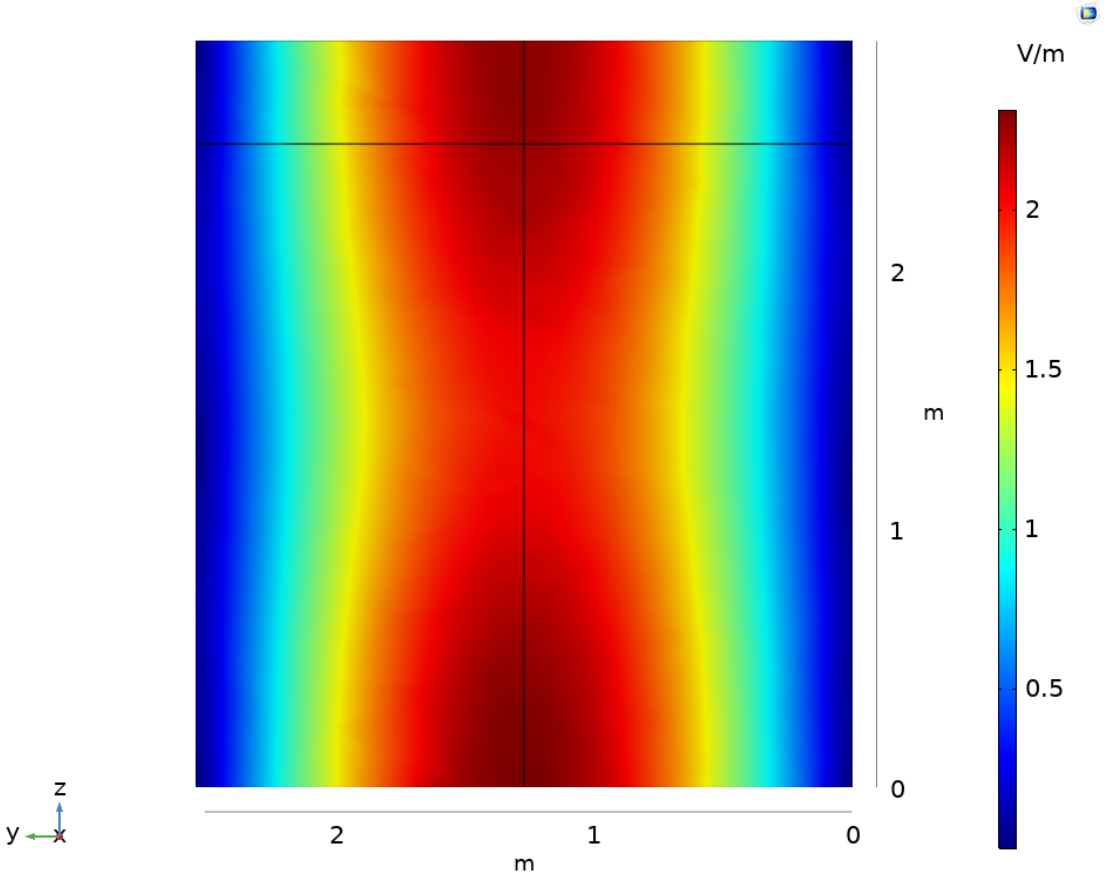

Figure 26: The YZ-plane of the modelled electric field in the shielded chamber with a biconical antenna at 60 MHz. The field slice is located at $x = 2.7$ m. The black lines signify the line-cuts over which measurements were done. The acquired data is measured at specific points on the measurement lines as shown in figure 27

The modelled electric field shows global minima over the entirety of the vertical exterior walls. The field increases closer to the middle with maxima in the middle at the top and bottom.

Figures 27a and 27b show that the measured electric field does not have the same wave pattern as predicted by the Comsol model. Especially the data on the vertical measurement line show the difference in wave pattern. The measurements done in the shielded chamber show a maximum at $z \approx 1.5$ m. This is approximately the middle of the shielded chamber. The model however predicted there to be a local minimum at this point. The data over the horizontal measurement line does show similar behaviour of the model and the measurements. However the electric field seems to decrease more slowly for the measurements. These discrepancies are discussed in the next section

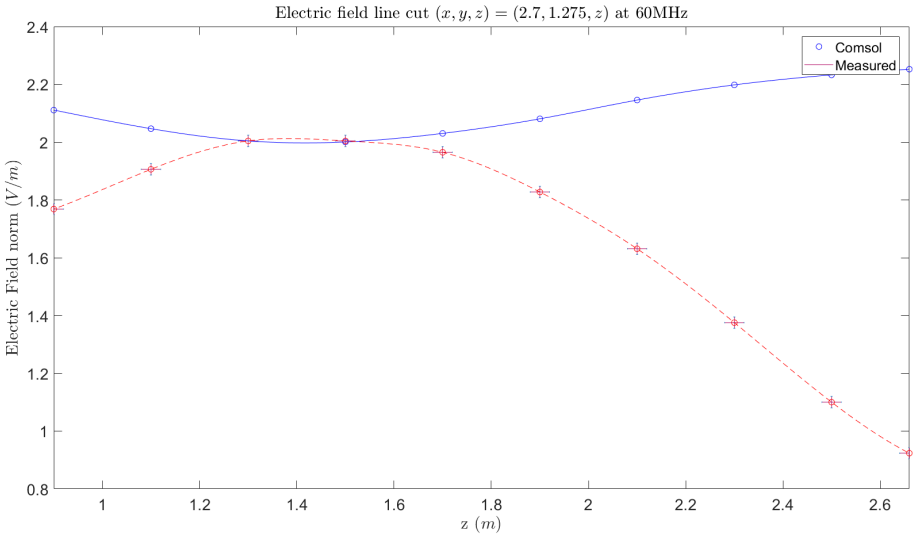

(a)

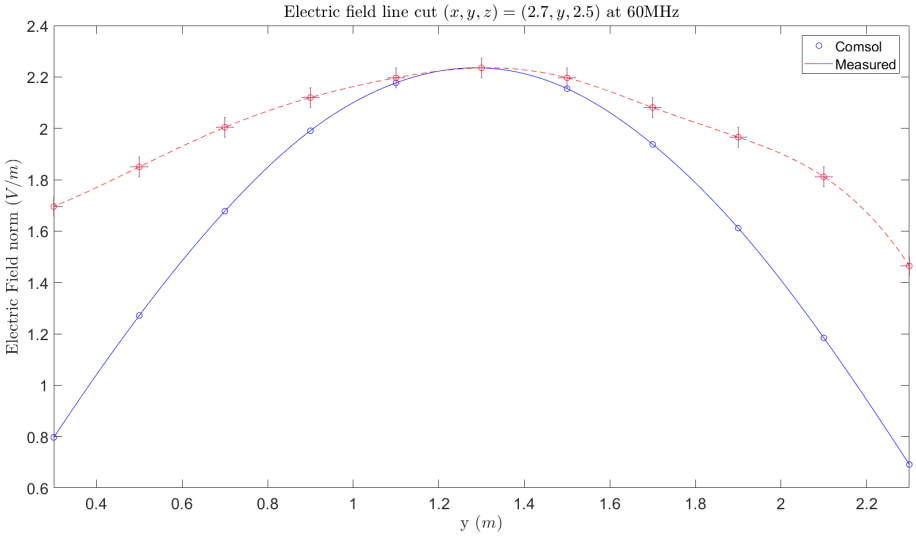

(b)

Figure 27: A comparison of the data points from the model with the measured electric field in the shielded chamber with a biconical antenna at Comtest. The comparison is made for a 60 MHz frequency. The modelled electric field is plotted in blue and the measured electric field is shown in red. The measurements have their respective errors. The vertical error bars are very small and almost not visible. These are errors after normalisation. The horizontal error bars are due to possible probe placement errors. Subfigure (a) shows the electric field over the linecut $(x, y, z) = (2.7, 1.275, z)$ m, which is the vertical line in the previous figure. Subfigure (b) shows the electric field at the horizontal line $(x, y, z) = (2.7, y, 2.5)$ m

At 90 MHz the modelled electric field shows a distinct pattern in the XY-plane at $z = 2.5$ m . This pattern is shown in figure 26. Again the black lines in the same figure signify the measurement lines that were chosen. The points on these measurement lines are shown and compared in figures 29a, 29b.

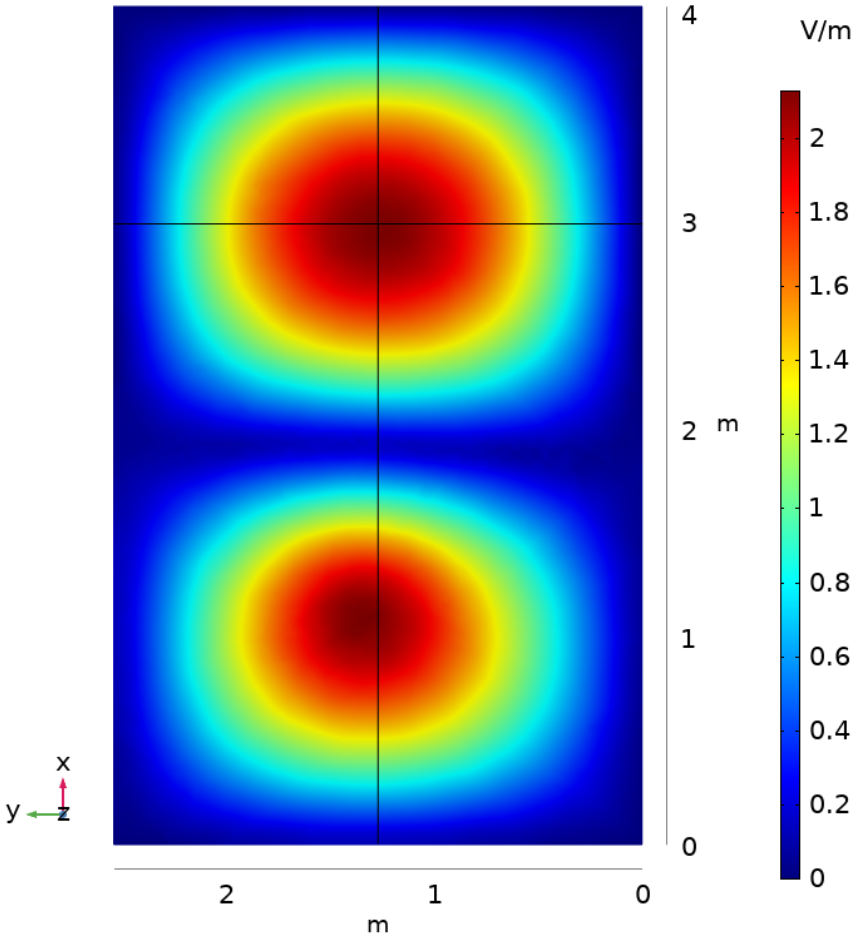

Figure 28: The XY-plane of the modelled electric field in the shielded chamber with a biconical antenna at 90 MHz. The field slice is located at $z = 2.5$ m. The black lines signify the line-cuts over which measurements were done. The acquired data is taken at specific points on these measurement lines as shown in figure 29

Even though the modelled electric field shows two peaks, the measurements show only 1. This is due to the limitation in the measurement setup by the antenna tripod and probe stand, as discussed in the previous chapter. The shielded chamber model at 90 MHz seems to accurately predict the behaviour of the electric field. Both the model and the measurements show a maximum of the electric field in the upper half of the XY-plane at $z = 2.5$ m. In figure 29a the model curve shows a minimum at $x \approx 1.9$ m where the measurement curve does not show this. However since the curve is interpolated between the two points it may as well be that in reality there is a minimum between points 1 and 2.

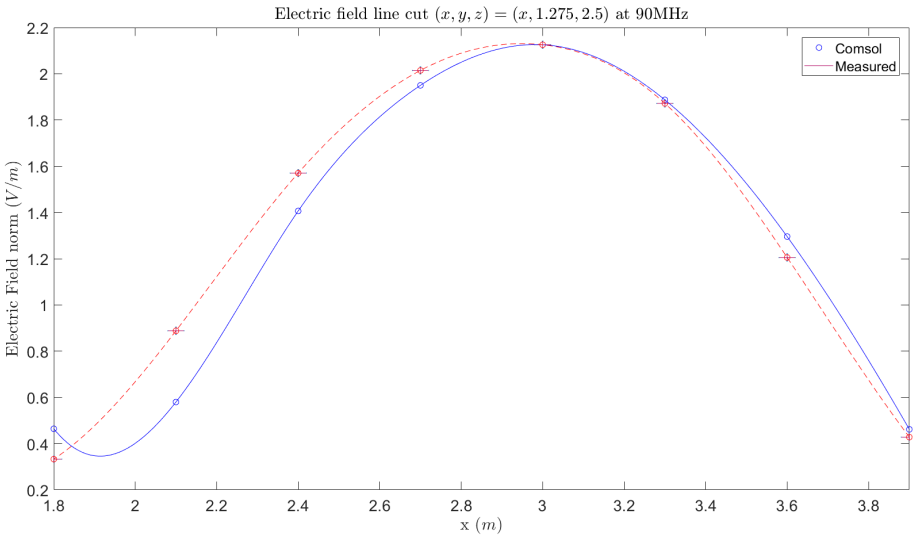

(a)

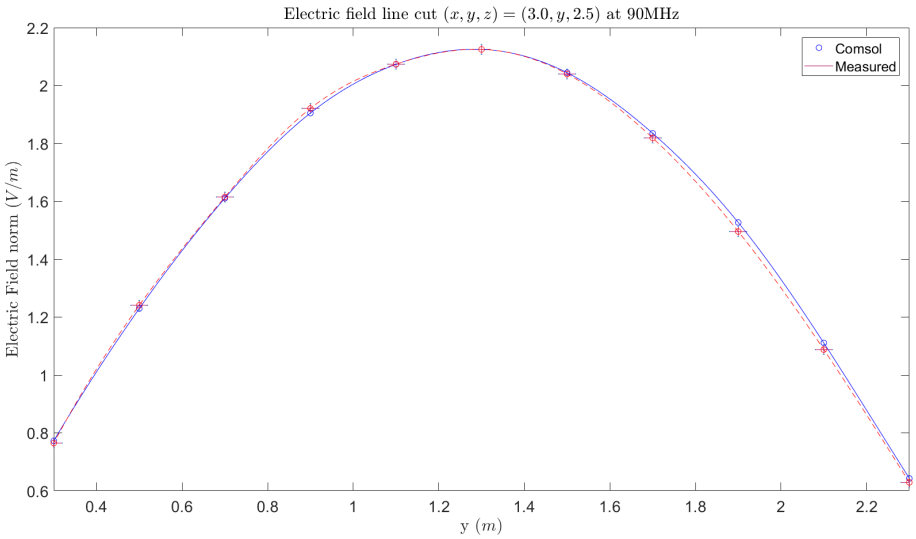

(b)

Figure 29: A comparison of the data points from the model with the measured electric field in the shielded chamber with a biconical antenna at Comtest. The comparison is made for a 90 MHz frequency. The modelled electric field is plotted in blue and the measured electric field is shown in red. The measurements have their respective errors. The vertical error bars are very small and almost not visible. These are errors after normalisation. The horizontal error bars are due to possible probe placement errors. The modelled and measured electric field over the line located at $(x, y, z) = (x, 1.275, 2.5)$ m is shown in subfigure (a). This is the vertical line in the previous plot. Note that we only see 1 maximum due to the restricted probe placement by the antenna tripod and probe stand. Subfigure (b) shows the electric field over the line located at $(x, y, z) = (3.0, y, 2.5)$ m

At 120 MHz the modelled electric field shows a distinct pattern in the XZ-plane at $y = 0.2$ m in figure 30. The black lines in the same figure signify the measurement lines that were chosen for this field slice. The data points on these measurement lines are shown and compared in figures 31a, 31b. As the probe cannot measure electric field below 0.9 meter in z-direction the data points are distributed from 0.9 to 2.7 meter. This is also the reason that figure 31a only shows two minima instead of 3.

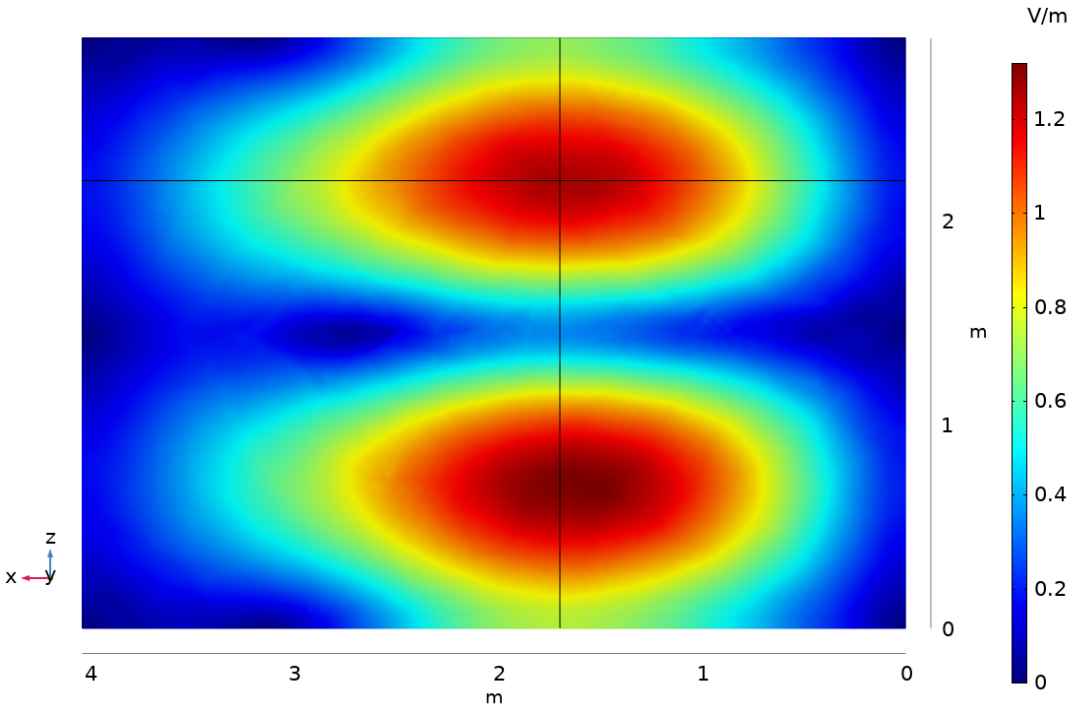

Figure 30: The XZ-plane of the modelled electric field in the shielded chamber with biconical antenna at 120MHz. We observe the field slice at $y = 0.2m$ m. This is close the the exterior wall with PEC bounaries. The black lines signify the line-cuts over which measurements were done

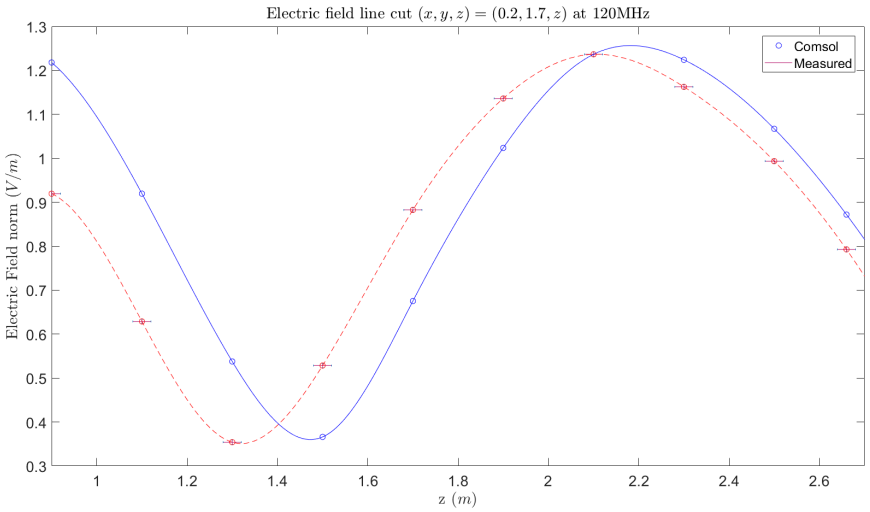

(a)

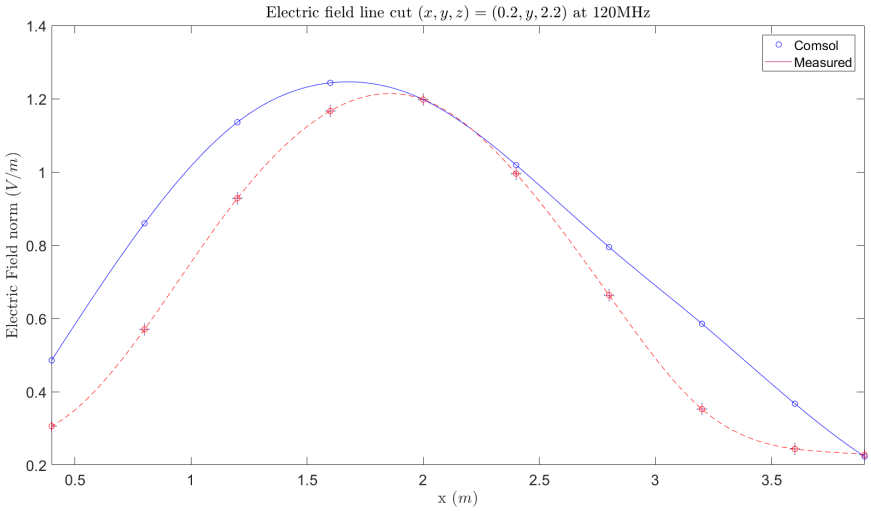

(b)

Figure 31: A comparison of the data points from the model with the measured electric field in the shielded chamber with a biconical antenna at Comtest. The comparison is made for a 120 MHz frequency. The modelled electric field is plotted in blue and the measured electric field is shown in red. The measurements have their respective errors. The vertical error bars are very small and almost not visible. These are errors after normalisation. The horizontal error bars are due to possible probe placement errors. Subfigure (a) shows the modelled and measured electric field over the line located at $(x, y, z) = (1.7, 0.2, z)$ m. The electric field begins at 0.9 m due the the limitations in the probe setup. Subfigure (b) shows the modelled and measured electric field over the line located at $(x, y, z) = (x, 0.2, 2.2)$ m

The field pattern as shown in figure 30 is similar to the measured field pattern. Both figures 31a and 31b show the predicted global maxima and minima. However both also show a shift of the measured field opposed to the modelled field. Additionally, figure 31b shows a linear decrease of the electric field in the modelled electric field whereas the measurements do not show this behaviour.

5.4 Shielded chamber with log-periodic dipole array antenna

The log-periodic array antenna (LPDA) is now modelled inside the shielded chamber with its perfectly conducting surfaces. The setup is shown in section 4.5. As stated in section 2.7, the amount of propagating waves increases with frequency. Therefore the modelled electric fields are also expected to show more complex patterns. We will do comparisons around 200 MHz starting at 180 MHz.

At 180 MHz the modelled electric field shows a distinct clover-like pattern in the YZ-plane at $x = 3.5$ m in figure 32. The black lines through the maxima in the figure signify the measurment lines. The data points on these lines are shown and compared in figures 33a, 33b and 33c.

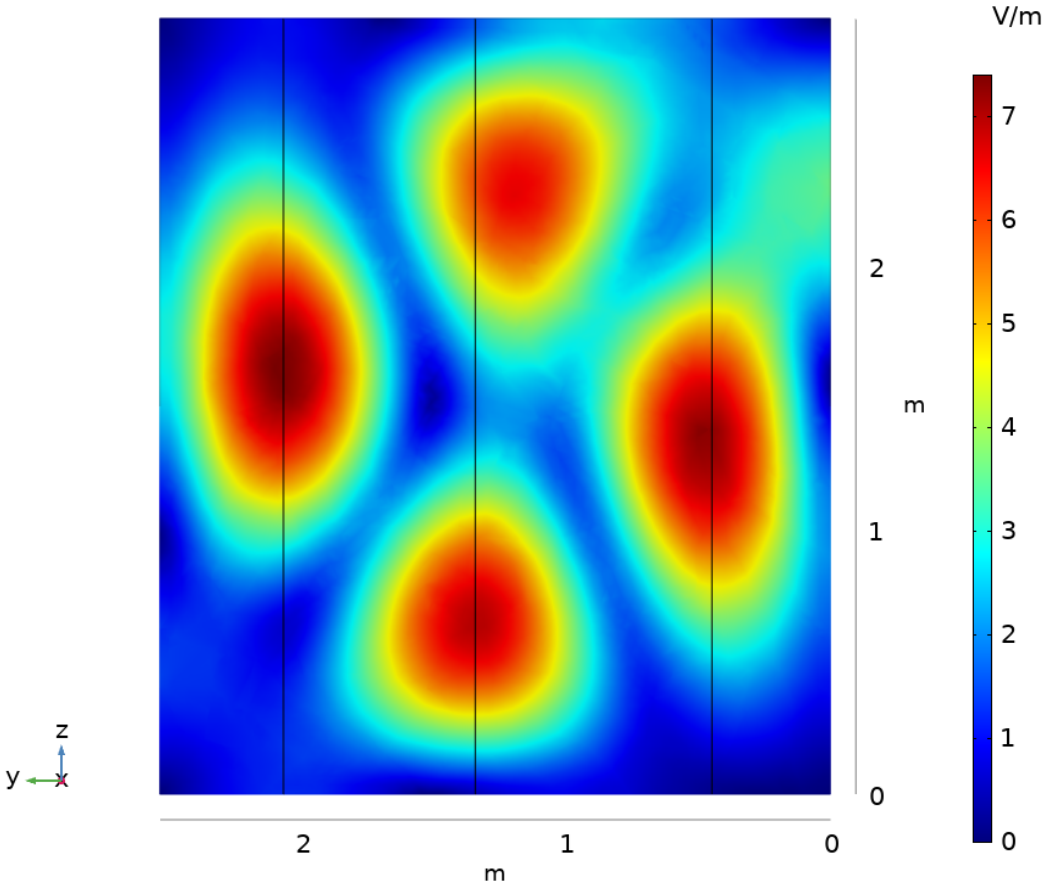

Figure 32: The YZ-plane of the modelled electric field in the shielded chamber with a log-periodic dipole array antenna at 180 MHz. The field slice is located at $x = 3.5$ m in the chamber. The black measurement lines are drawn through the maxima to see whether the model correctly predicted these in the shielded chamber at Comtest

Figure 33a shows that the model predicts a maximum at $z \approx 1.65$ m. The measurements from the Comtest shielded chamber do show a maximum, however this maximum is shifted to $x \approx 1.4$ m. Also the measurement show a region where the electric field is almost constant at $z = 2.1$ m, this is not shown by the model which decreases monotonically for heights above 1.65 m.

Figure 33b shows that the model predicts two peaks at $y = 1.34$ m. The measurements do show two maxima. The maxima at 0.9 m is however much lower than predicted by the model. Due to a restriction by the probe setup, electric field below 0.9 meter cannot be measured therefore the we cannot show the field pattern below this.

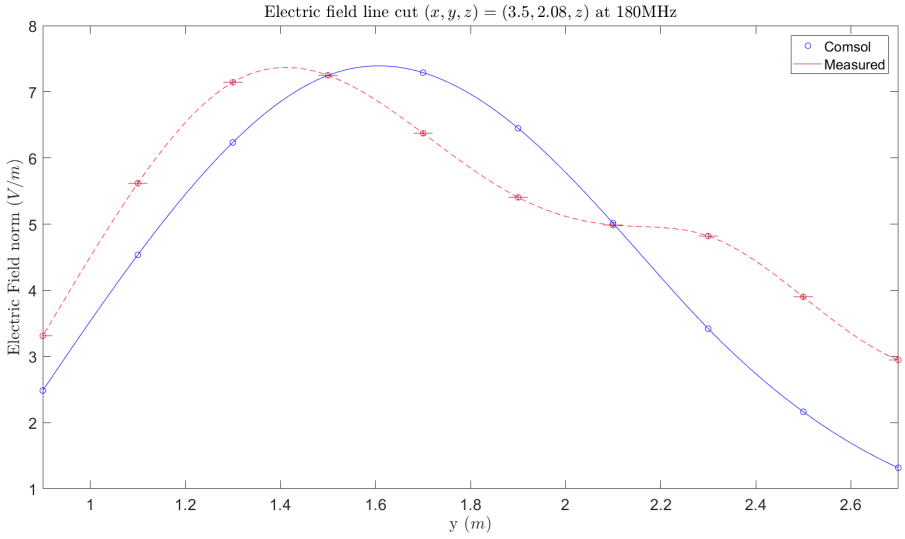

(a)

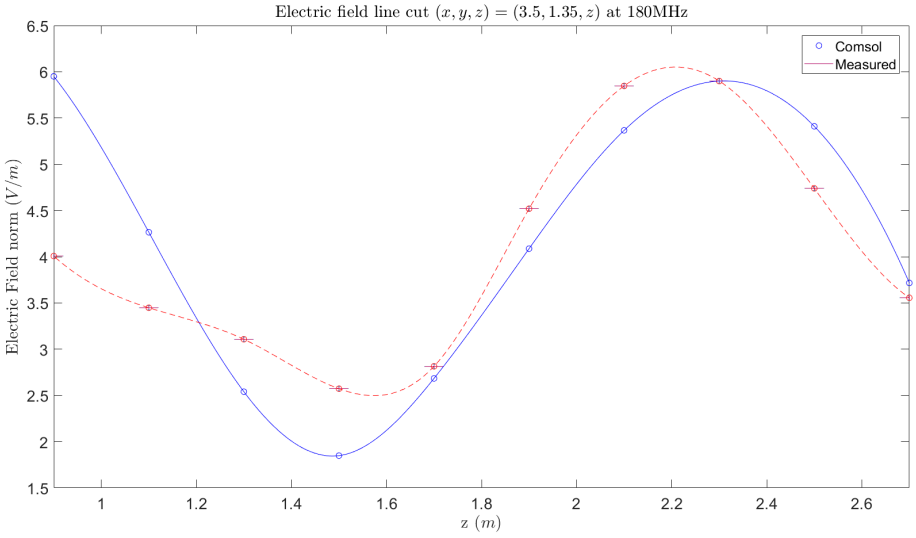

(b)

Figure 33

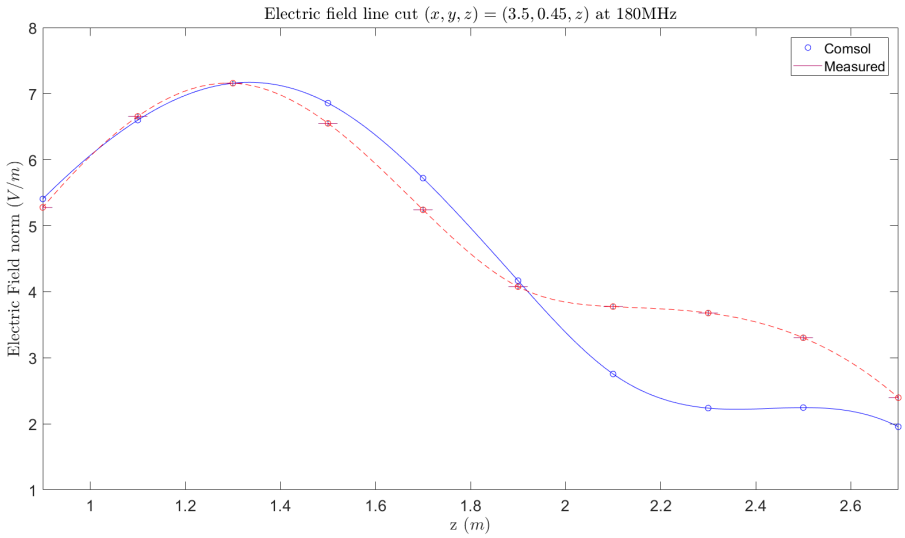

(c)

Figure 33: A comparison of the data points from the model with the measured electric field in the shielded chamber with a log-periodic dipole array antenna at Comtest. The comparison is made for a 180 MHz frequency. The modelled electric field is plotted in blue and the measured electric field is shown in red. The measurements have their respective errors. The vertical error bars are very small and almost not visible. These are errors after normalisation. The horizontal error bars are due to possible probe placement errors. Subfigure (a) shows the modelled and measured electric field over the line located at $(x, y, z) = (3.5, 2.08, z)$ m. Subfigure (b) shows the modelled and measured electric field over the line located at $(x, y, z) = (3.5, 1.35, z)$ m. Subfigure (c) shows the modelled and measured electric field over the line located at $(x, y, z) = (3.5, 0.45, z)$ m. The data points start at $z = 0.9$ m as the probe setup has restrictions in adjustability as explained in 4.9

The model correctly predicts the position of the maximum in figure 33c. The general wave pattern is the same. Both data sets show a flattening of the curve near $z \approx 2$ m. However part of the curve with constant electric field is higher for the measurements than the model.

The modelled electric field at 225 MHz shows a very specific field pattern in the XZ-plane at $y = 0.1$ m. This pattern is very close to the boundary so will be similar to the electric field on the boundary. The field pattern is shown in figure 34. The measurements over the black measurement lines are shown and compared in figures 35a and 35b.

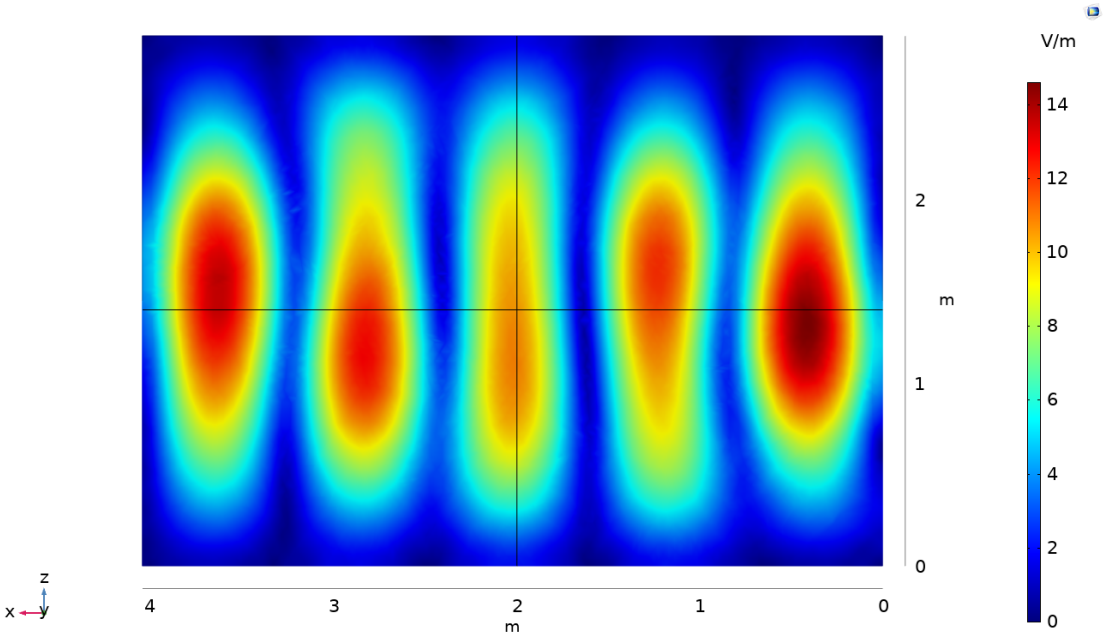

Figure 34: The XZ-plane of the modelled electric field in the shielded chamber at 225 MHz. The field slice is located at $y = 0.1$ m, which is close to the exterior wall of the shielded chamber. The field will thus be similar to the field on the boundary. The black lines specify the lines over which data points are acquired

The modelled field slice shows 5 maxima next to each other in the XZ-plane. To see whether this electric field pattern is correctly predicted by the model we will do measurements over the horizontal measurement line. This will show whether or not the maxima are correctly predicted. The vertical measurement line checks the electric field behaviour in the z-direction.

Figure 35a shows that the electric field pattern in the x-direction is accurately predicted by the model. All 5 maxima are shown at the correct locations. There are some deviations in amplitude apparent though.

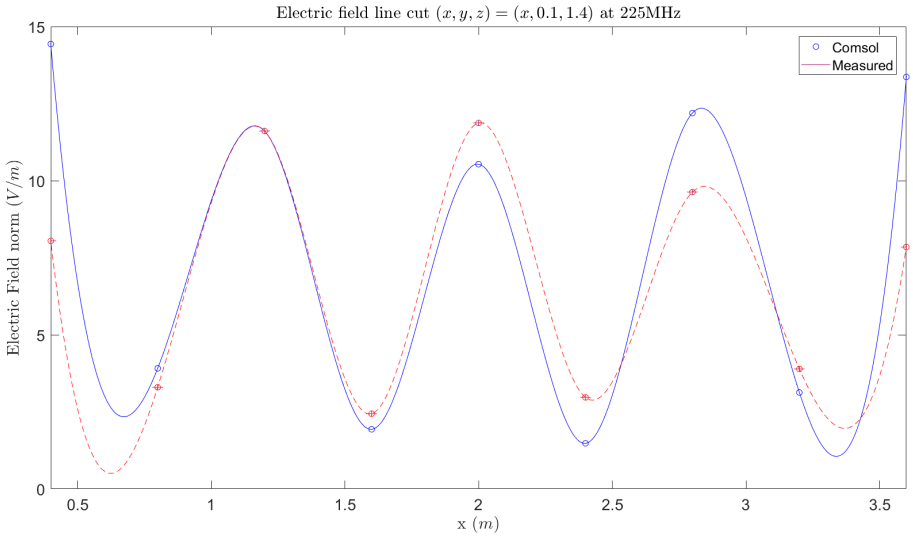

(a)

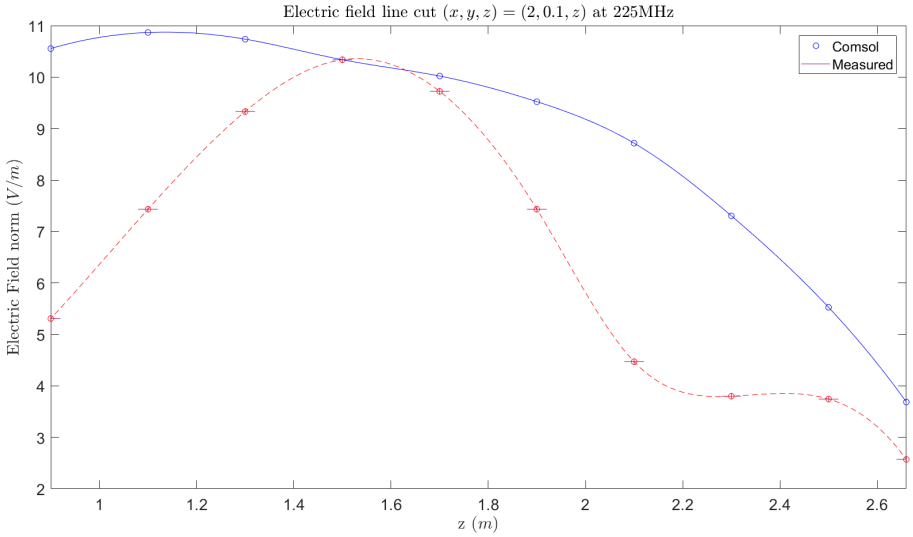

(b) T

Figure 35: A comparison of the data points from the model with the measured electric field in the shielded chamber with a log-periodic dipole array antenna at Comtest. The comparison is made for a 225 MHz frequency. The modelled electric field is plotted in blue and the measured electric field is shown in red. The measurements have their respective errors. The vertical error bars are very small and almost not visible. These are errors after normalisation. The horizontal error bars are due to possible probe placement errors. Subfigure (a) shows the modelled and measured electric field over the line located at $(x, y, z) = (x, 0.1, 1.4)$ m. he modelled and measured electric field over the line located at $(x, y, z) = (2, 0.1, z)$ m. The data points start at $z = 0.9$ m as the probe setup has restrictions in adjustability as explained in 4.9

The data points both show a maxima. The place of this maxima is not predicted at the correct location. The middle maximum in the model decreases in field strength more quickly near the boundary whereas the measurement suggests the maximum to decrease more quickly in the middle. Therefore the middle maximum should have been more similar to the most right maximum in figure 34. This discrepancy is discussed in the next chapter.

The highest modelled frequency for the shielded chamber is 240 MHz. At this frequency the electric field pattern starts to become more complex. The field pattern in the XY-plane at $z = 1.9$ m will be observed. The field pattern is shown in figure 36. The measurements over the black measurement lines are shown and compared in figures 37a and 37b.

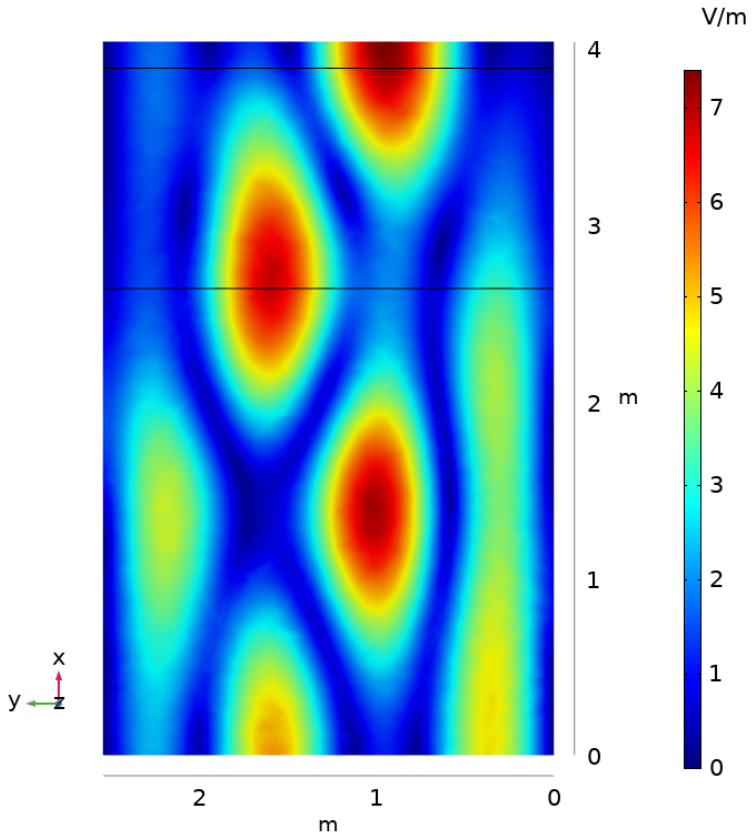

Figure 36: The XY-plane of the modelled electric field in the shielded chamber with a log-periodic dipole array antenna at 240 MHz. The black lines specify the lines over which data points are acquired. The field slice is located at $z = 1.9$ m

The electric field at 240 MHz shows a similar clover shape as seen at 180 MHz in the bottom left corner. However there is another maximum in the top right. There are two horizontal measurement lines. Initially there were two vertical lines as well, however due restrictions in the measurement setup these were only measurable for $x > 2$ m. The measurement data from the Comtest chamber along these lines were lost.

Figure 37a shows that the model predicts the general wave pattern shown by the measurements. The maxima are at the correct locations. The local minima of the model data at $y = 0.65$ m and $y = 1.05$ m are not supported by the measurement date though.

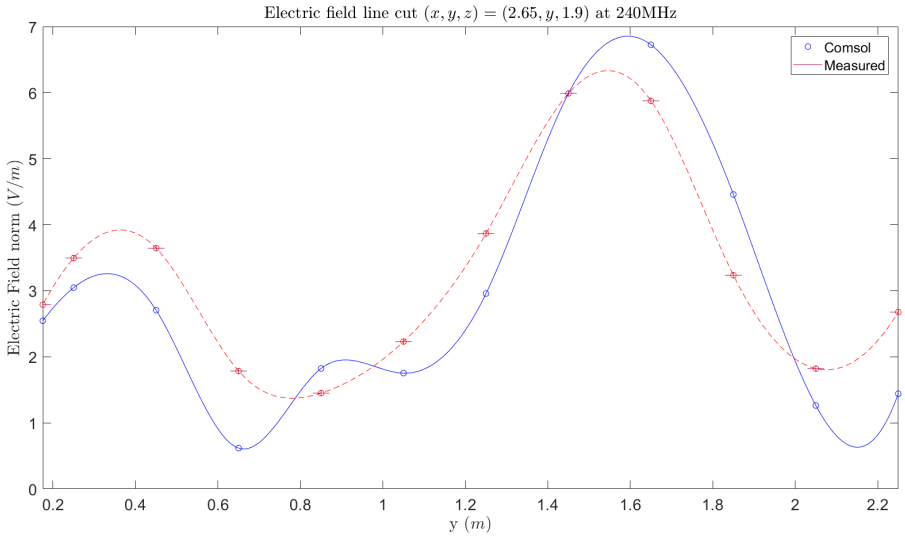

(a)

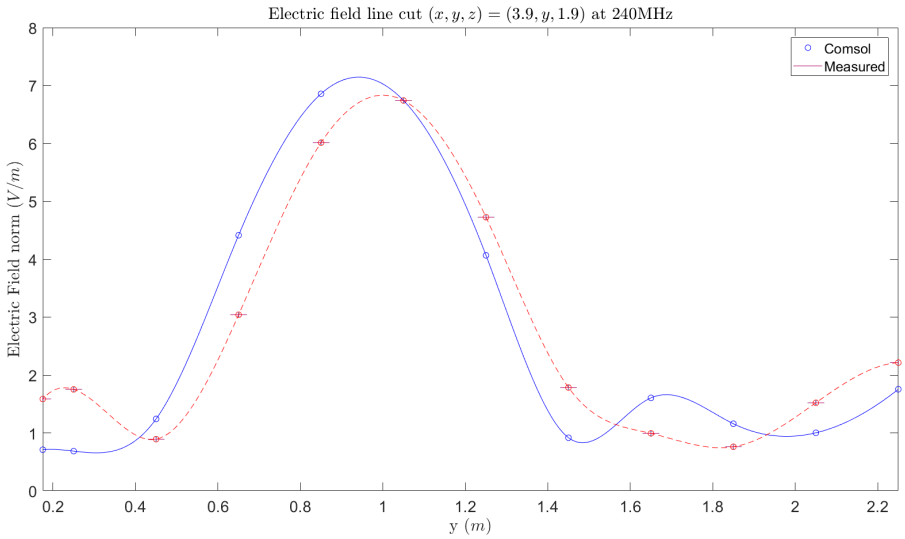

(b)

Figure 37: A comparison of the data points from the model with the measured electric field in the shielded chamber with a log-periodic dipole array antenna at Comtest. The comparison is made for a 240 MHz frequency. The modelled electric field is plotted in blue and the measured electric field is shown in red. The measurements have their respective errors. The vertical error bars are very small and almost not visible. These are errors after normalisation. The horizontal error bars are due to possible probe placement errors. Subfigure (a) shows the modelled and measured electric field over the line located at $(x, y, z) = (2.65, y, 1.9)$ m. Subfigure (b) shows the modelled and measured electric field over the line located at $(x, y, z) = (3.9, y, 1.9)$ m

Again the general wave pattern is correctly predicted by the Comsol model. Yet it is not completely accurate as the local maximum at $y = 0.25$ m is not predicted. Also the model expected a local minimum at $y = 1.7$ m. The measurement data do not show this.

5.5 Shielded chamber with biconical antenna and dielectric object

The model build in Comsol Multiphysics was used to assess the characterization of the electric field in a loaded shielded chamber, so a shielded chamber with additional dielectric object. These results are not used as intermediate step for the reverberation chamber model but are added for physical completeness. The setup for the shielded chamber loaded with a tank of water of dimensions (0.27 m $\times$ 0.565 m $\times$ 0.269 m) and a biconical antenna is shown in section 4.6. The results below were acquired using this setup.

At 60 MHz the electric field slice of the YZ-plane at $x = 3.8$ m shows a simple electric field pattern. A maximum of the electric field norm at the middle bottom of the chamber is shown.

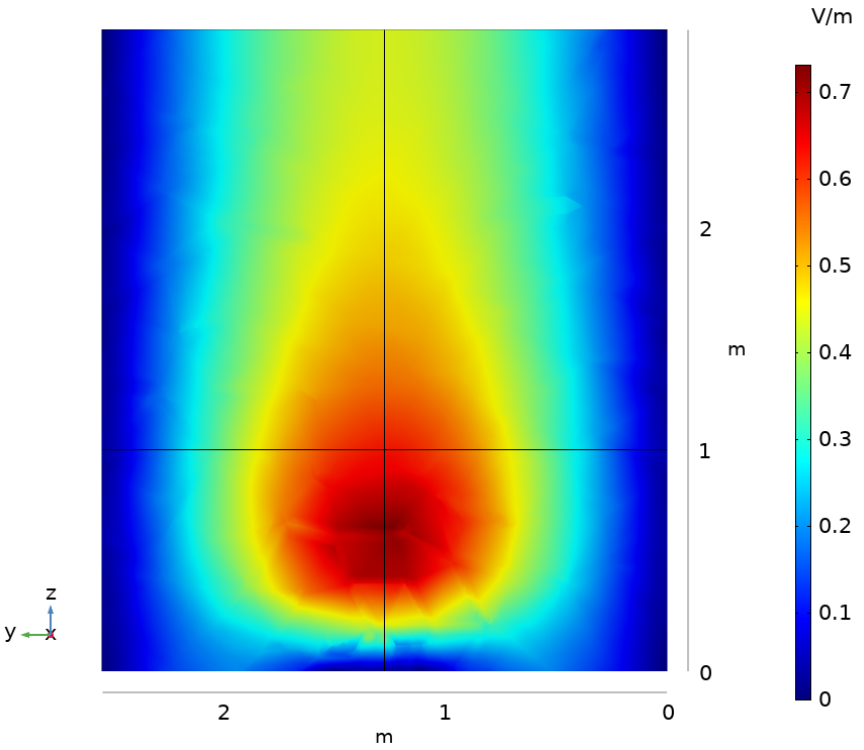

Figure 38: The YZ-plane of the modelled electric field in the loaded shielded chamber with a biconial antenna at 60 MHz. The black lines are the lines over which the data points are acquired

As the maxima at $z \approx 0.6$ m is not reachable with the field probe a horizontal measuring line was chosen at $z = 1.0$ meter. Another vertical line was chosen in the middle going through the maximum.

Previously we have seen that the empty shielded chamber was not accurately predicted by the model of the empty shielded chamber. The same appears to be true for the loaded shielded chamber at 60 MHz. Figure 39a starts at $z = 0.9$ m because that is the lowest measurable point of the electric field for the field probe. The model predicted the electric field to monotonically decrease from there. The measurements however first increase a little and decreased after $z = 1.6$ m. This seems to be a shift approximately 0.5 meters of the maximum electric field.

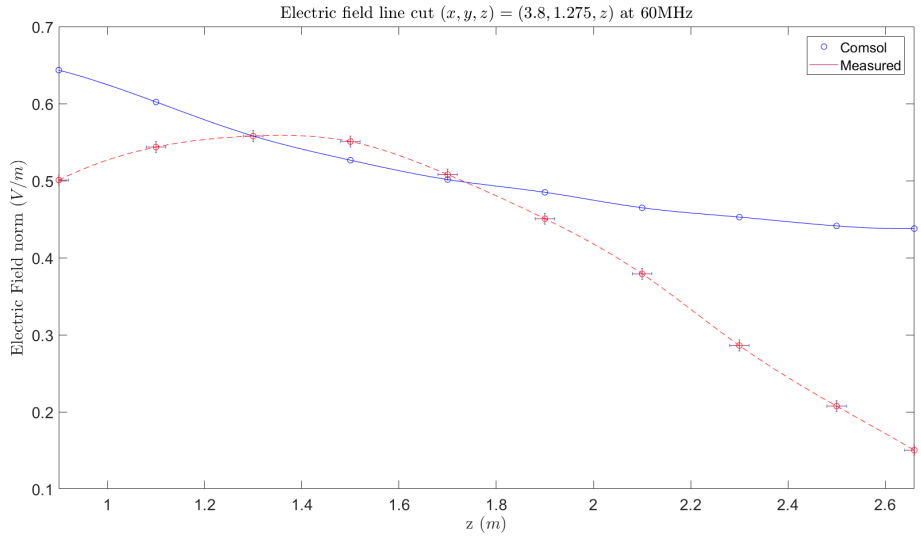

(a)

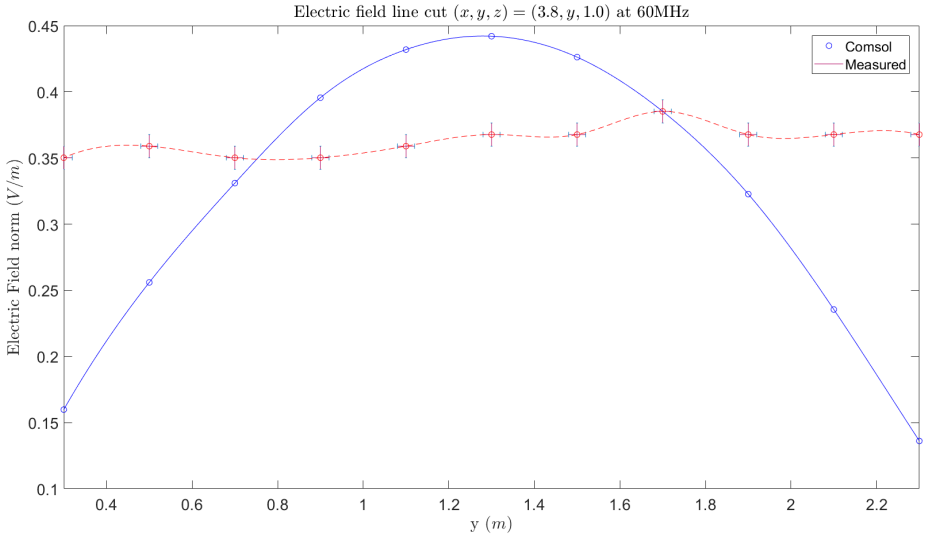

(b)

Figure 39: A comparison of the data points from the model with the measured electric field in the loaded shielded chamber with a biconical antenna at Comtest. The comparison is made for a 60 MHz frequency. The loading is a tank filled with tap-water. The modelled electric field is plotted in blue and the measured electric field is shown in red. The measurements have their respective errors. The vertical error bars are very small and almost not visible. These are errors after normalisation. The horizontal error bars are due to possible probe placement errors. Subfigure (a) shows the modelled and measured electric field over the line located at $(x, y, z) = (3.8, 1.275, z)$ m. The data points start at $z = 0.9$ m due to restrictions in the probe setup. Subfigure (b) shows the modelled and measured electric field over the line located at $(x, y, z) = (3.8, y, 1.0)$ m

Figure 39b suggest the electric field to be approximately constant of the y-axis. The Comsol Multiphysics model predicts the exact opposite having maximum in the middle of the y-axis. Possible explenations are discussed in the next chapter.

At 90 MHz the electric field in the empty chamber predicted the general wave pattern. Figure 40 shows the modelled electric field at $x = 2.0$ m. The black lines signify the measurement lines.

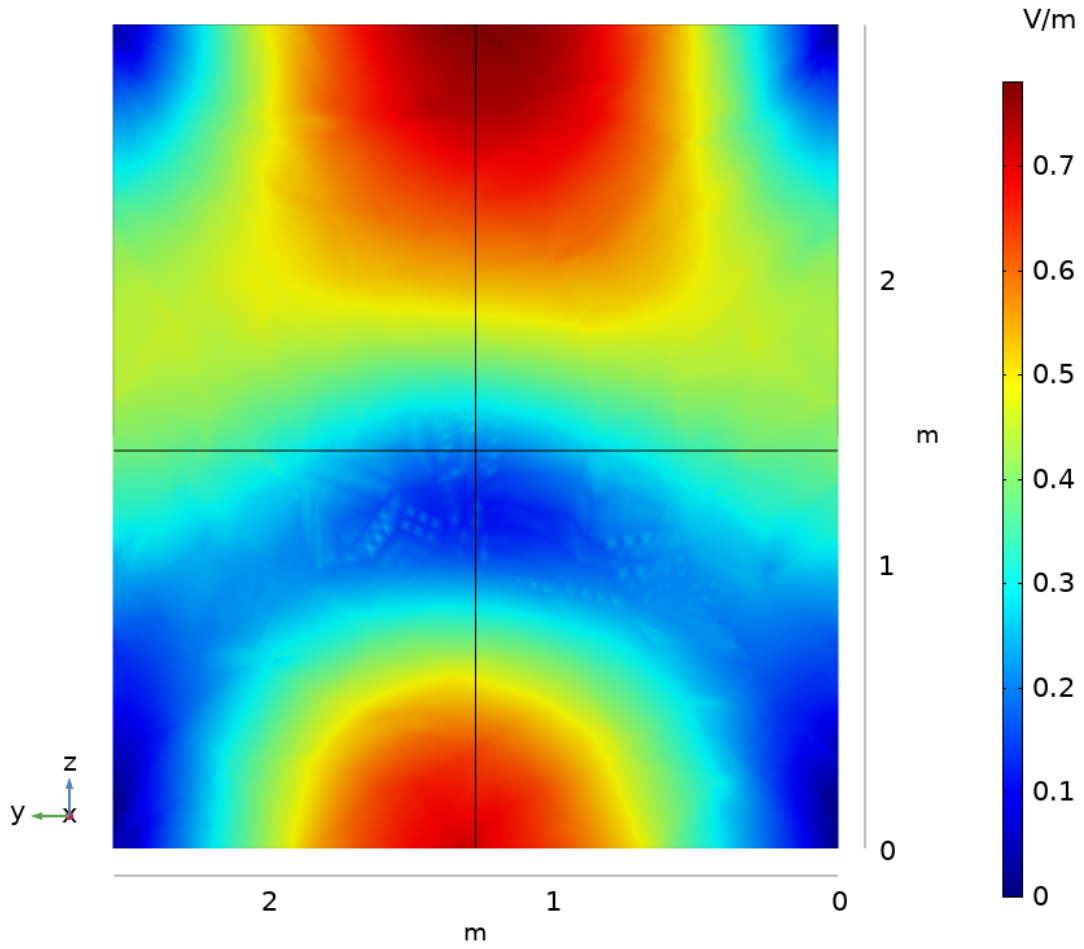

Figure 40: The XY-plane of the modelled electric field in the loaded shielded chamber with a biconial antenna at 90 MHz. The field slice is located at $x = 2.0$ m. The black lines are the lines over which data points are distributed

The predicted pattern shows two maxima in the middle at the bottom and the top. The vertical measurement line runs through these. The horizontal line eliminates the possibility of additional maxima in the middle.

Similarly to the empty shielded chamber at 90 MHz, the loaded shielded chamber model predicts the behaviour of the electric field. The minimum in figure 41a is located at the same position for the model and the measurements .

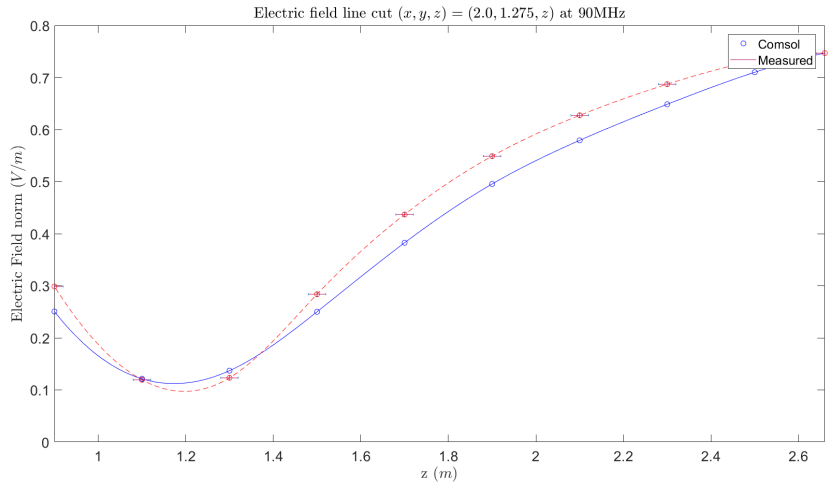

(a)

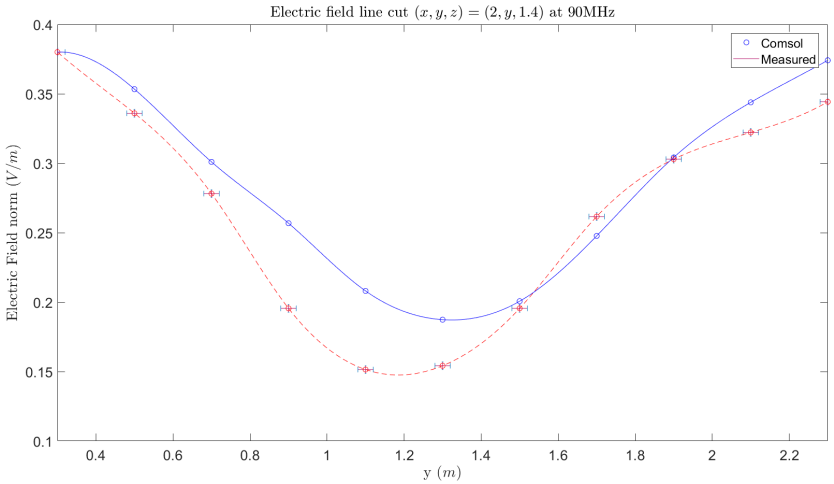

(b)

Figure 41: A comparison of the data points from the model with the measured electric field in the loaded shielded chamber with a biconical antenna at Comtest. The comparison is made for a 90 MHz frequency. The loading is a tank filled with tap-water. The modelled electric field is plotted in blue and the measured electric field is shown in red. The measurements have their respective errors. The vertical error bars are very small and almost not visible. These are errors after normalisation. The horizontal error bars are due to possible probe placement errors. Subfigure (a) shows the modelled and measured electric field over the vertical line located at $(x, y, z) = (2.0, 1.275, z)$ m. Subfigure (b) shows the modelled and measured electric field over the horizontal line located at $(x, y, z) = (2.0, y, 1.4)$ m

Although the model does predict a minimum, the location of the minimum is shifted 20 centimeters in the measurements.

At 120 MHz an interesting field slice was found in the YZ-plane at $x = 2.0$ m. The same loaded shielded chamber setup was used as before. Figure 43 shows the modelled electric field with the measurement lines in shown in black.

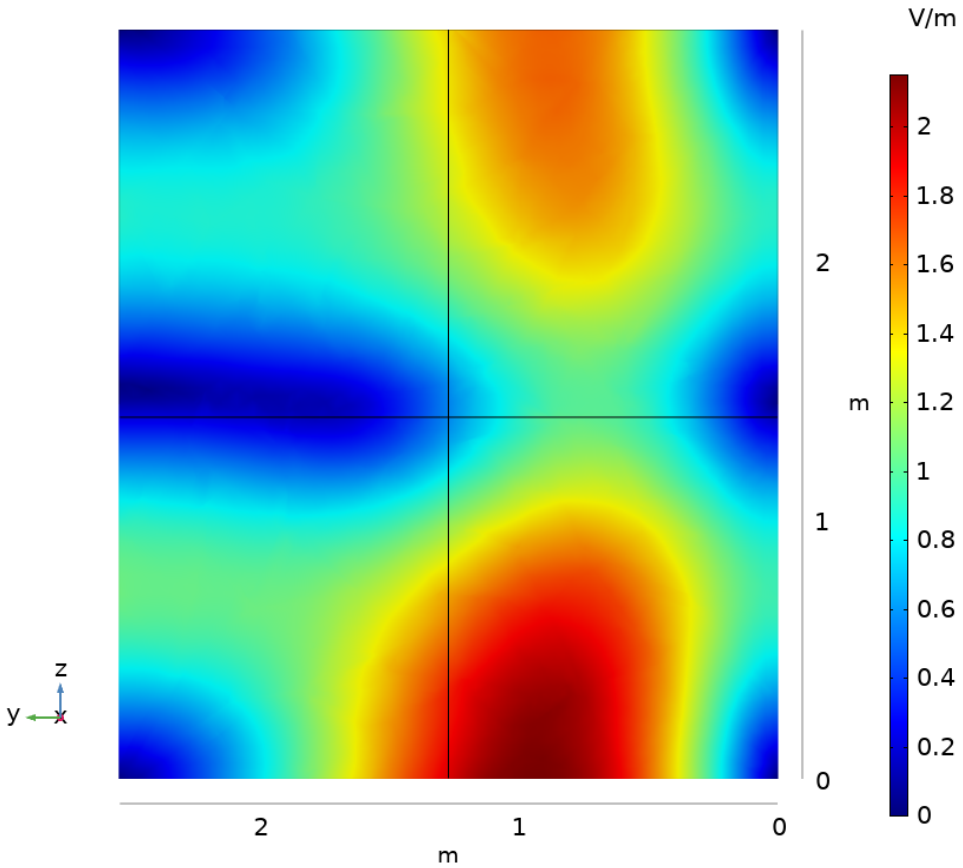

Figure 42: The YZ-plane of the modelled electric field in the loaded shielded chamber with a biconical antenna at 120 MHz. The black lines show the locations of the measurement lines over which the data points are distributed

The model predicts an electromagnetic field with two maxima near the middle of the y-axis at the bottom and top of the chamber.

Figure 43a shows good correspondence between the prediction of the electric field by the model and the measured electric field. Both show a minimum at nearly the same location. The measurement is shifted with approximately 0.1 m with respect to the model.

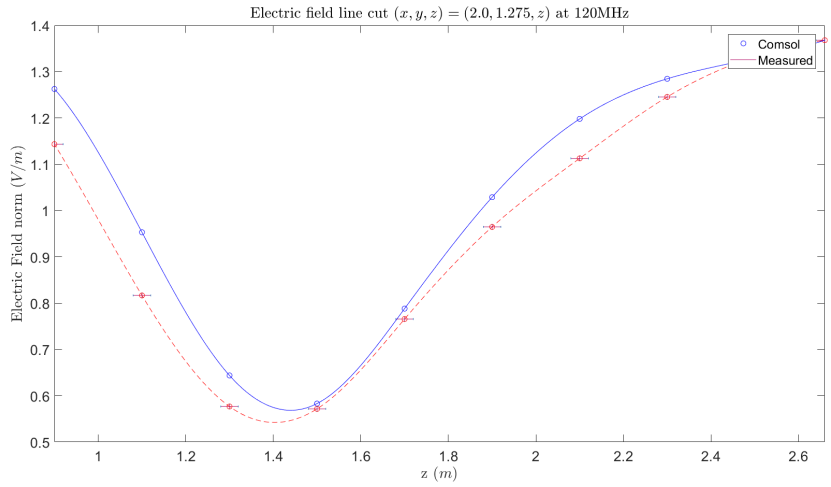

(a)

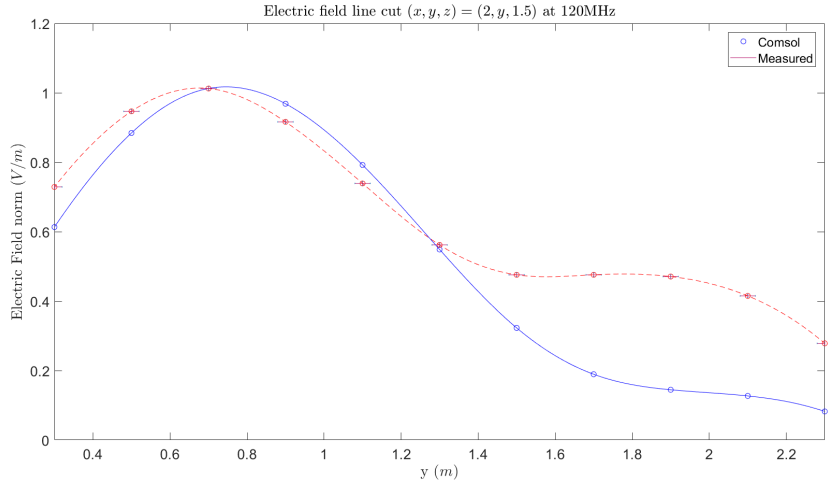

(b)

Figure 43: A comparison of the data points from the model with the measured electric field in the loaded shielded chamber with a biconical antenna at Comtest. The comparison is made for a 120 MHz frequency. The loading is a tank filled with tap-water. The modelled electric field is plotted in blue and the measured electric field is shown in red. The measurements have their respective errors. The vertical error bars are very small and almost not visible. These are errors after normalisation. The horizontal error bars are due to possible probe placement errors. Subfigure (a) shows the modelled and measured electric field over the vertical line located at $(x, y, z) = (2.0, 1.275, z)$ m. The starting data point is at $z = 0.9$ m due to restrictions of the probe setup. Subfigure (b) shows the modelled and measured electric field over the horizontal line located at $(x, y, z) = (2.0, y, 1.5)$ m

Figure 43b shows that the general form of the wave is predicted by the model. Both curves show flattening near $y = 1.7$ m, though the measurements have a higher electric field at these points compared to the Comsol model.

5.6 Shielded chamber with log-periodic dipole array antenna and dielectric object

Again, the results of this sub-section are not included as intermediate step for the final reverberation chamber model, but are added for physical completeness. The shielded chamber with dielectric object is referred to as loaded shielded chamber.

5.6.1 Electric field in the shielded chamber with dielectric object

To observe if Comsol Multiphysics can handle more complex electric fields we need higher frequencies. These are modelled using the log-periodic dipole array antenna. The setup for the shielded chamber with the log-periodic dipole array antenna and dielectric object is shown in section 4.7. The dielectric object is a container filled with tap-water with dimensions (0.27 m $\times$ 0.565 m $\times$ 0.269 m). The right corner of the tank is located at $(x, y, z) = (3, 1, 0)$ m.

The first frequency for which the model is assessed is 180 MHz. Figure 45 shows the modelled electric field slice in the YZ-plane at $x = 2.0$ m with the black line-cuts.

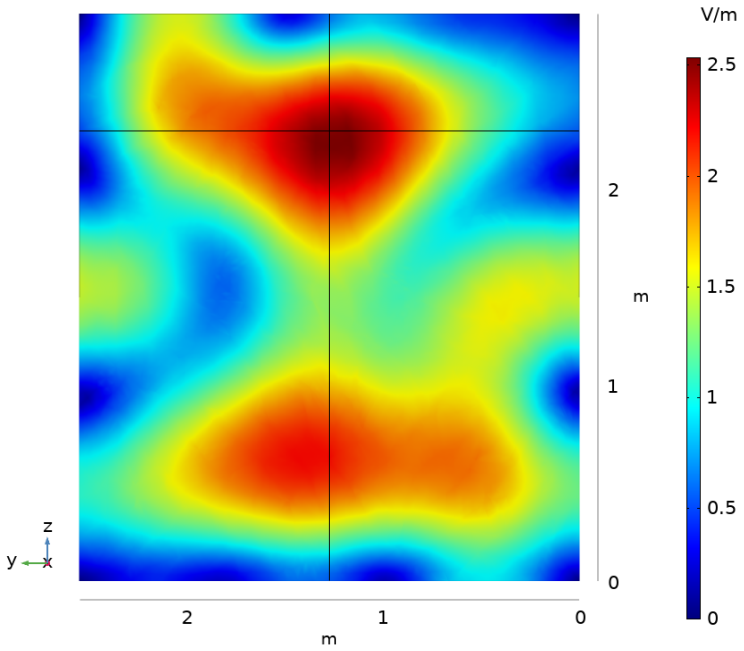

Figure 44: The YZ-plane of the modelled electric field in the shielded chamber with dielectric object and log-periodic dipole array antenna at 180 MHz. The black lines are the line-cuts over which data points are acquired

The modelled electric field shows complex shaped maxima. The maxima are located near the bottom and top of the slice. The vertical line-cut checks the prediction of two maxima and the horizontal line checks whether there is only one maxima in the middle as predicted by the model.

The general electric field pattern in the model is supported by the measurements. However, subfigure 45a shows that the local minimum of the measurements is higher than predicted by the model.

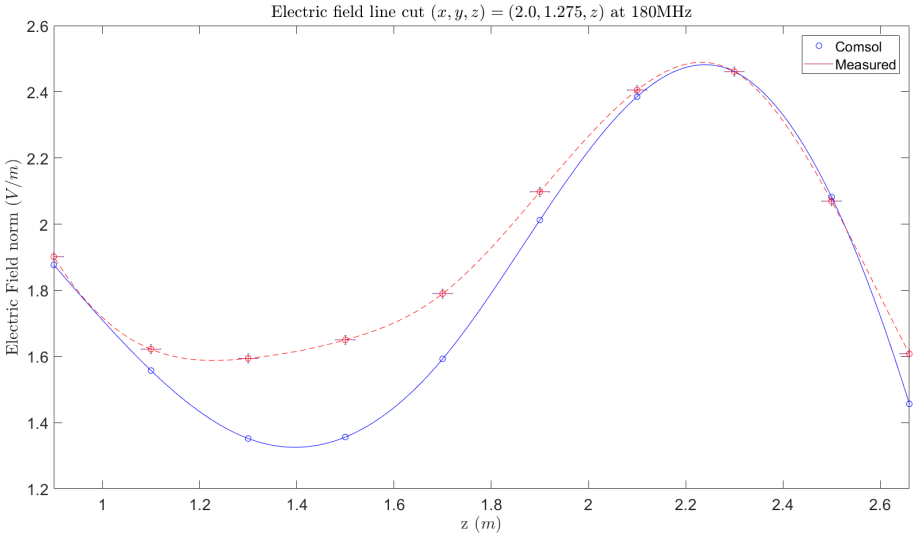

(a)

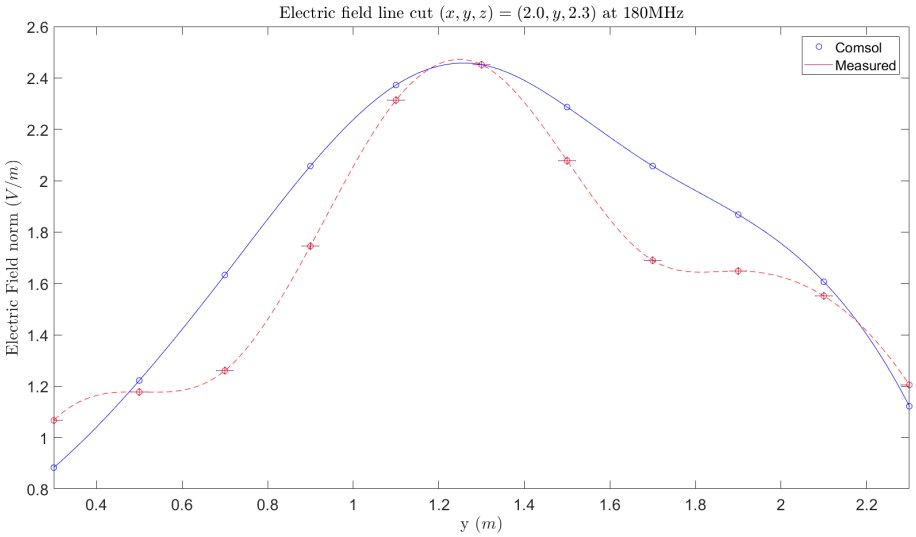

(b)

Figure 45: A comparison of the data points from the model with the measured electric field in the loaded shielded chamber with a log-periodic dipole array antenna at Comtest. The comparison is made for a 180 MHz frequency. The loading is a tank filled with tap-water. The modelled electric field is plotted in blue and the measured electric field is shown in red. The measurements have their respective errors. The vertical error bars are very small and almost not visible. These are errors after normalisation. The horizontal error bars are due to possible probe placement errors. Subfigure (a) shows the modelled and measured electric field over the line located at $(x, y, z) = (2.0, 1.275, z)$ m. The data points start at $z = 0.9$ m due to limitations of the probe setup. Subfigure (b) shows the modelled and measured electric field over the line located at $(x, y, z) = (2.0, y, 2.3)$ m

The maximum of the model corresponds with the maximum of the measurements. Though the model predicts an almost linear decline in electric field strength for decreasing y, where the measurements show that the electric field strength decreases more slowly near the boundary of the shielded chamber.

The next frequency at which we compare the electric field in the model to the measured electric field is 210 MHz. The location of the field slice is $x = 2$ m.

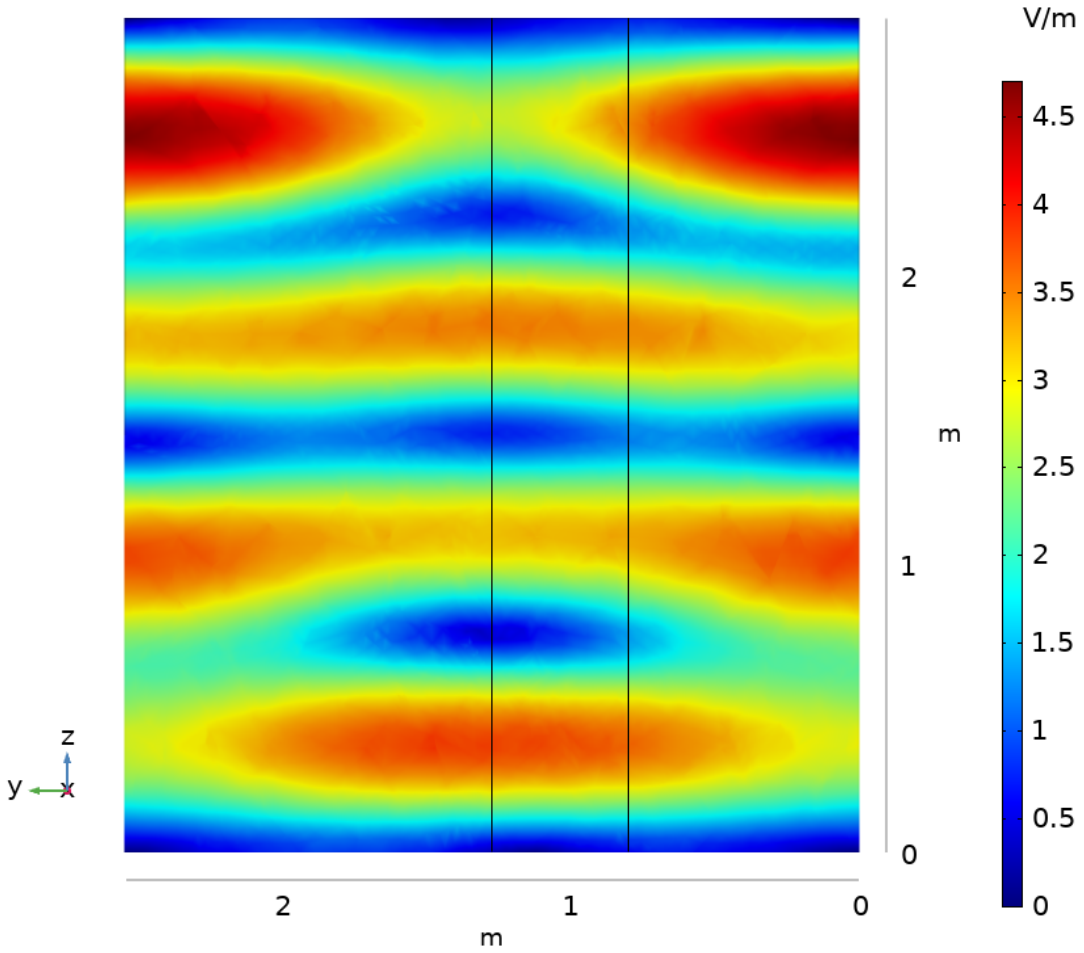

Figure 46: The YZ-plane of the modelled electric field in the loaded shielded chamber at 210 MHz with the black measurement lines

The modelled electromagnetic field shows a complex electric field pattern. There is a clear wave-like pattern in the z direction where bands of maxima are distributed

The model predicts the correct locations of the maxima. The measurement amplitudes deviate slightly from the amplitudes predicted by the model.

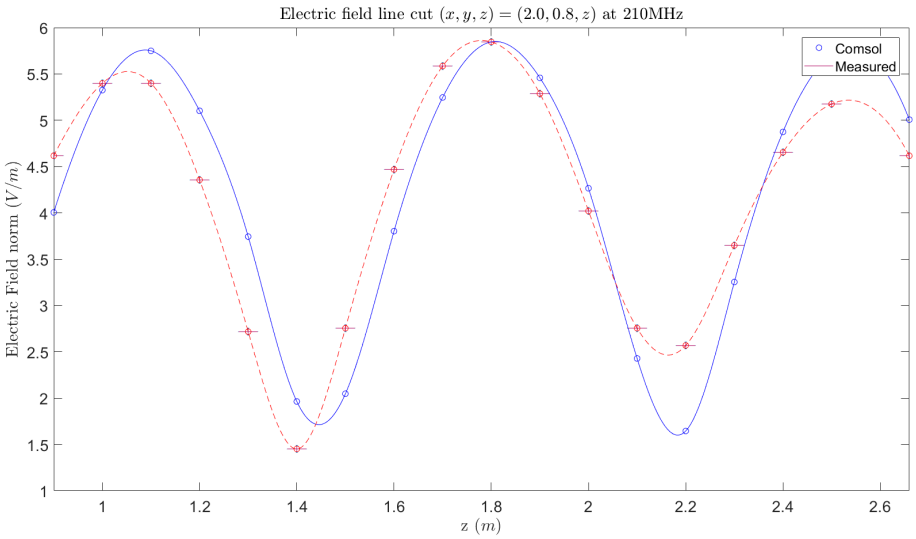

(a)

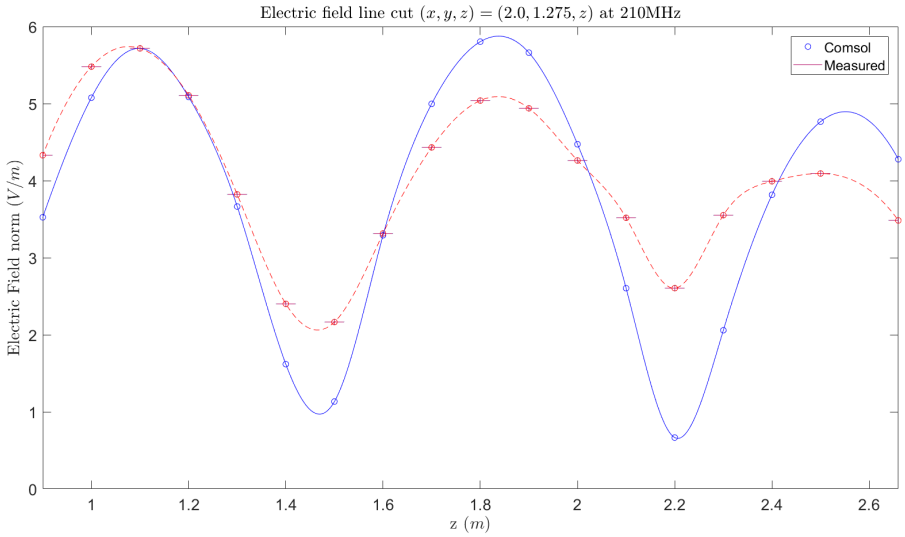

(b)

Figure 47: A comparison of the data points from the model with the measured electric field in the loaded shielded chamber with a log-periodic dipole array antenna at Comtest. The comparison is made for a 210 MHz frequency. The loading is a tank filled with tap-water. The modelled electric field is plotted in blue and the measured electric field is shown in red. The measurements have their respective errors. The vertical error bars are very small and almost not visible. These are errors after normalisation. The horizontal error bars are due to possible probe placement errors. Subfigure (a) shows the modelled and measured electric field over the line located at $(x, y, z) = (2.0, 0.8, z)$ m. Subfigure (b) shows the modelled and measured electric field over the line located at $(x, y, z) = (2.0, 1.275, z)$ m. In both subfigures the data points start at 0.9 meter due to limitations in the probe setup

The model correctly predicts the locations of the maxima at 210 MHz. Thus the general waveform is correctly predicted by the model. Even though the model does show a lower amplitude for the maximum near the boundary, the measurements show an even larger decrease. The measured wave pattern looks more like a damped wave.

The last frequency at which we compare the modelled electric field in the loaded shielded chamber to the measurements is 225 MHz. This field slice is again taken in the YZ-plane. Now the location of the field slice is (x=3.8 m). This is close to the wall of the shielded chamber.

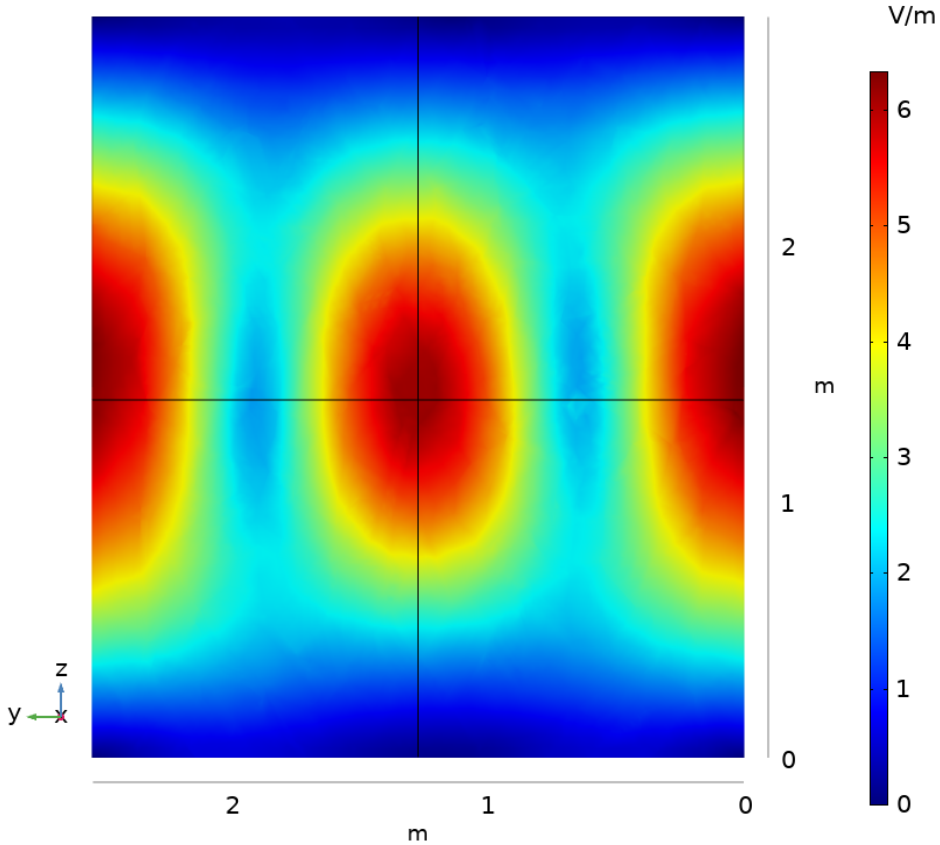

Figure 48: The YZ-plane of the modelled electric field in the shielded chamber with dielectric object and log-periodic dipole array antenna at 225 MHz. The black lines show the field line-cut placements

The electric field pattern shows three similarly shaped maxima next to each other. If the model is to be believed the horizontal measurement line will show the existance of three maxima and the vertical line-cut will show only one maximum in the middle.

Figure 49a shows that the model correctly predicts the location of the maximum of the electric field. Though, the model and the measurements are different in the way they decrease from this maximum. The model decreases linearly whereas the measurements show a bigger decrease further from the maximum.

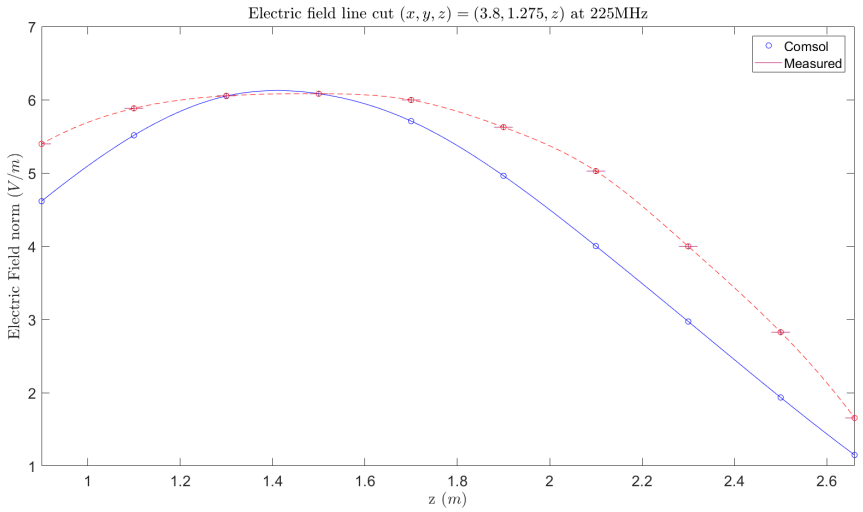

(a)

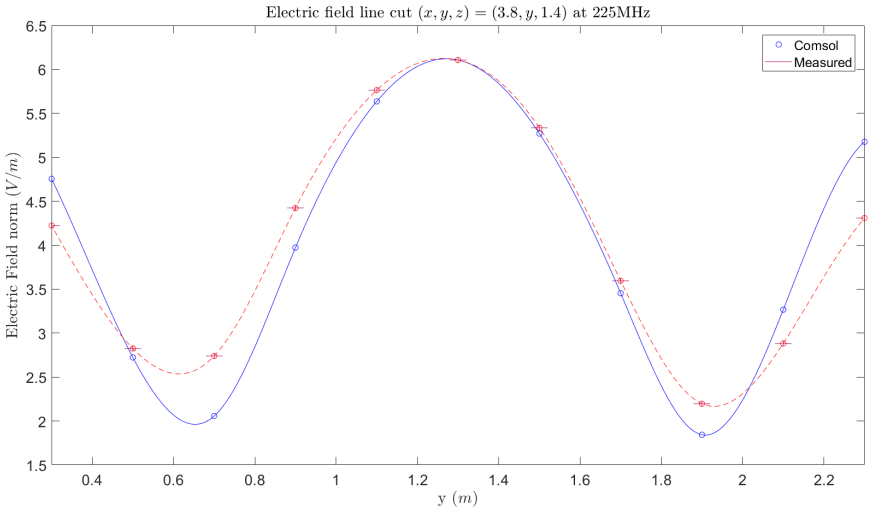

(b)

Figure 49: A comparison of the data points from the model with the measured electric field in the shielded chamber with dielectric object and log-periodic dipole array antenna at Comtest. The comparison is made for a 225 MHz frequency. The loading is a tank filled with tap-water. The modelled electric field is plotted in blue and the measured electric field is shown in red. The measurements have their respective errors. The vertical error bars are very small and almost not visible. These are errors after normalisation. The horizontal error bars are due to possible probe placement errors. Subfigure (a) shows the modelled and measured electric field over the line located at $(x, y, z) = (3.8, 1.275, z)$ m. The points start at 0.9 m again due to the restrictions caused by the probe setup. Subfigure (b) shows the modelled and measured electric field over the line located at $(x, y, z) = (3.8, y, 1.4)$ m

The general wave pattern predicted by the model seems to be correct. It shows two minima, a maximum in the middle and two maxima at the boundary of the chamber. The measured minima do show slight deviations in amplitude compared to the model

5.6.2 Electric field in the water tank

The theory about complex waves in matter predicted absorption to increase for larger imaginary parts of the permittivity and for increasing permeability. Comtest has special ferrite tiles designed to absorb as much radiation as possible. These had high permeability and a high ratio of imaginary vs real permittivity. The high permeability ensures low reflectivity and the high ratio of imaginary-real permittivity ensures good absorption. Therefore the ferrite tile absorbs better than a tank of water. The tank of water however has better reflection. To check whether the model in Comsol Multiphysics showed this theorised behaviour, the modelled object changes only in material and not in dimensions (0.27 m $\times$ 0.565 m $\times$ 0.269 m). This is shown in figure 50.

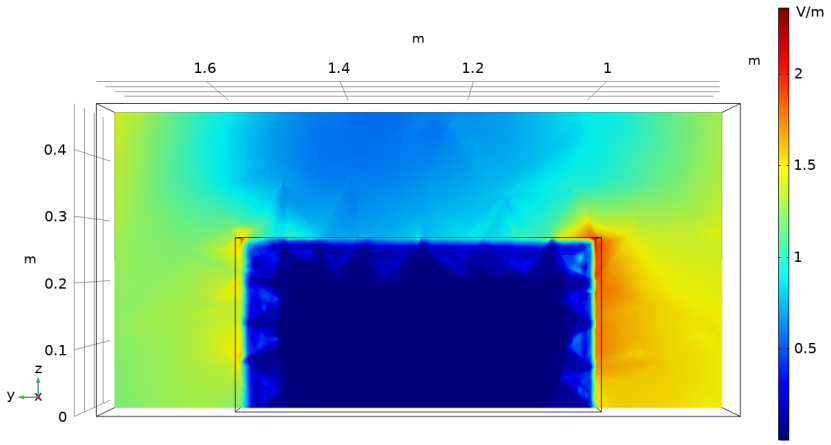

(a)

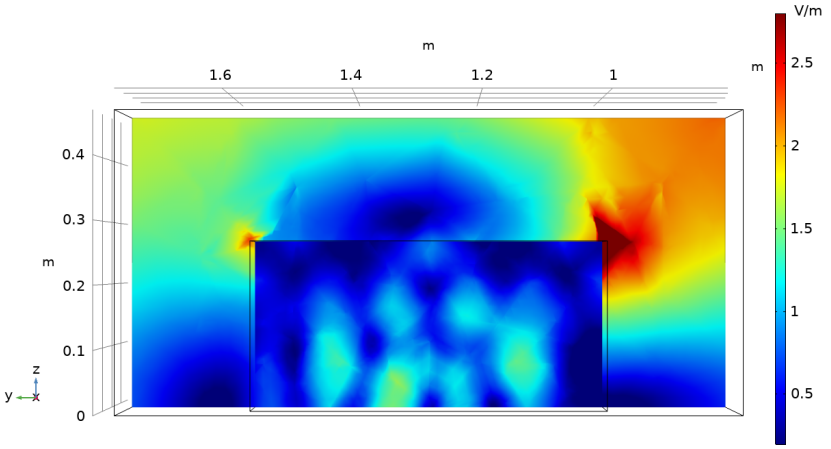

(b)

Figure 50: The modelled absorption by two different materials. The dimensions of the objects are Subfigure (a) shows the high absorption of a ferrite material and subfigure (b) shows the absorption and reflection of water

As can be seen in the figure, the ferrite tile has a lower electric field inside the object. Where the tank of water shows some electromagnetic peaks inside the object, the ferrite tile completely absorbs the electromagnetic radiation. This is exactly as the theory predicted.

5.7 Reverberation chamber with z-fold stirrer

To characterize a reverberation chamber (5.03 m × 3.97 m × 2.85 m), an empty chamber validation test will be done for both the model and the real reverberation chamber. This test checks the chamber field uniformity and is performed as explained in section 4.9. The setup for this comparison is shown in section 4.8.

The theory predicts the field uniformity to increase for increasing frequency. At higher frequencies, more propagating modes are available, thus a superposition will be more random with more maxima and minima. This means that the average uniformity is higher. Below, the electric field is plotted in the YZ-plane ($x = 2.4$ m) of the electric field in the reverberation chamber at 200 MHz and 300 MHz. The electric fields calculated by Comsol Multiphysics support the theory that the electric field becomes more uniform for higher frequencies. This is shown by amount of maxima and minima in the figure. The more maxima and minima, the more even the distribution of the electric field. This property is not caused by the addition of a Z-fold stirrer in the room, but rather a property of the number of propagating modes for higher frequencies. See Appendix 61 for the electric field without the stirrer, which shows the same behaviour.

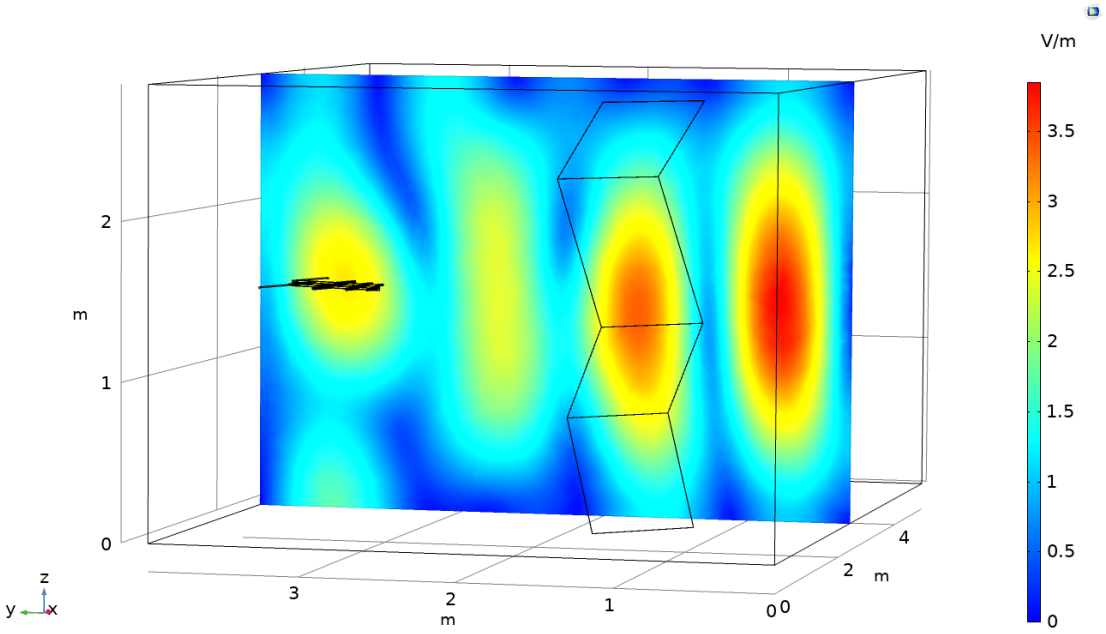

(a)

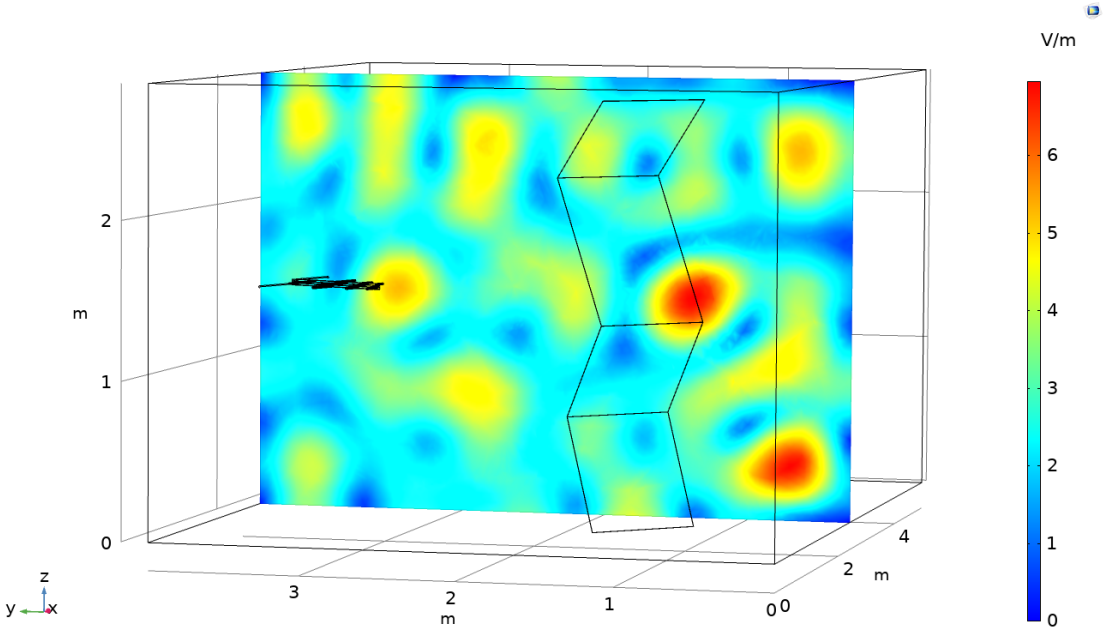

(b)

Figure 51: The electric field plotted at 200 MHz is less uniformly distributed than the electric field at 300 MHz. This is in accordance with the theory. Subfigure (a) shows the electric field plotted in the YZ-plane of the reverberation chamber at 200 MHz. Subfigure (b) shows the electric field plotted in the YZ-plane of the reverberation chamber at 300 MHz

The electric field uniformity will be compared for 4 stirrer rotation positions. The results are shown below in figure 52:

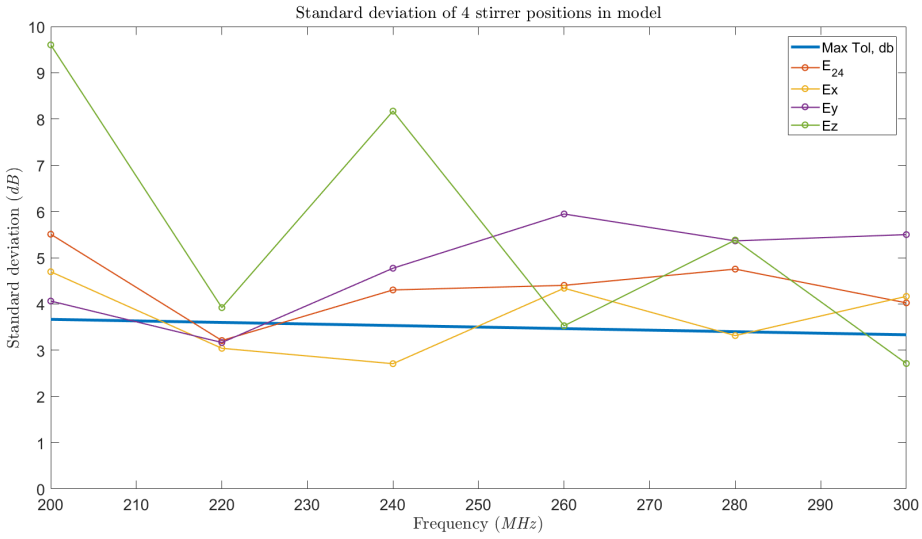

(a)

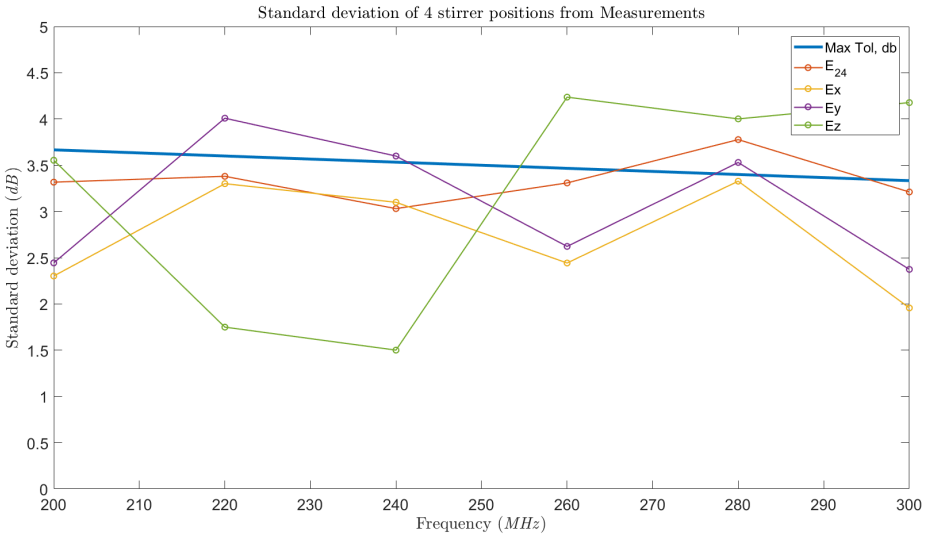

(b)

Figure 52: The electric field uniformity plotted against the frequency (MHz). The uniformity σ_i is plotted for all directions x,y,z and the total field σ_{24}. The straight dark blue line represents the field uniformity requirements as stated in IEC 61000-4-21 (International Electrotechnical Commission & Technical Committee 77, 2011). Subfigure (a) shows the electric field uniformity (dB) for the model using 4 stirrer rotation positions. Subfigure (b) shows the electric field uniformity (dB) for the reverberation chamber at Comtest for 4 stirrer rotation positions

The field uniformity test shows much higher values for the model compared to the measured field uniformity. Higher values mean that the field is less uniform. Figure 52a shows that the uniformity increases for increasing frequency. This is the expected behaviour for the field uniformity. Figure 52b has field uniformity values near the IEC 61000-4-21 requirements.

Next the electric field uniformity is compared for 12 stirrer rotation positions. The results are plotted in figure 53.

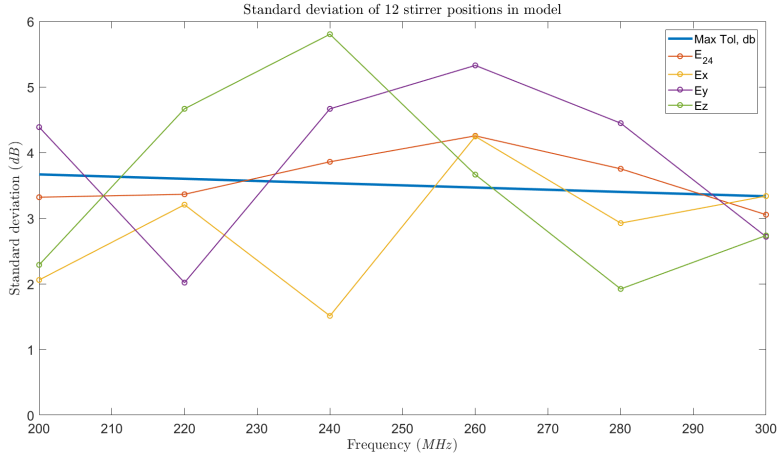

(a)

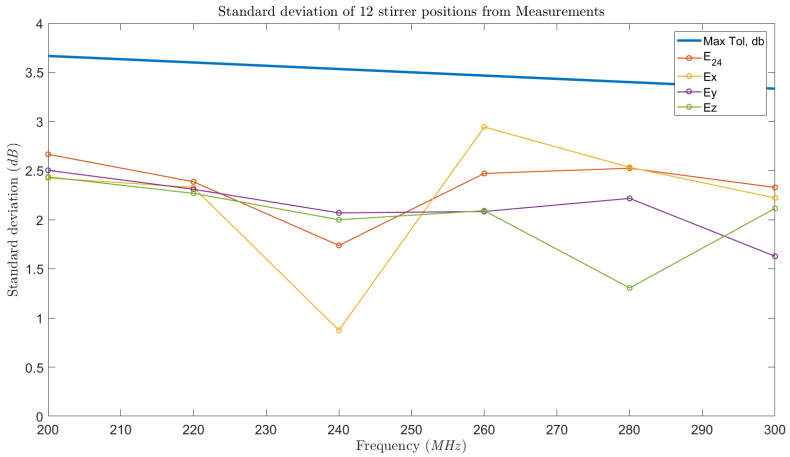

(b)

Figure 53: The electric field uniformity plotted against the frequency (MHz). The uniformity σ_i is plotted for all directions x,y,z and the total field σ_{24}. The straight dark blue line represents the field uniformity requirements as stated in IEC 61000-4-21 (International Electrotechnical Commission & Technical Committee 77, 2011). Subfigure (a) shows the electric field uniformity (dB) for the model using 12 stirrer rotation positions. Subfigure (b) shows the electric field uniformity (dB) for the reverberation chamber at Comtest for 12 stirrer rotation positions

The field uniformity of the reverberation chamber with 12 stirrer rotation positions shows much lower values than it did for 4 stirrer rotation positions. This is the expected behaviour. For 3 of the 6 frequencies, the total field uniformity σ_{24} is below the IEC 61000-4-21 requirements. Also the field uniformity is shown to be decreasing for increasing frequency, though 200 and 220 MHz do not represent this. However this is also shown in the calculated uniformity values of the 4 stirrer rotation position. Figure 53b shows that the Comtest reverberation chamber reaches the required uniformity as stated by the IEC 61000-4-21 for all frequencies. The field uniformity shows a slight trend downwards as expected.

5.8 Shifted laplacian preconditioner

In subsection 3.7 a theoretical introduction to the shifted laplacian preconditioner was given. It was described that by increasing the conductivity, the eigenvalues move away from the origin thereby explaining why a the Helmholtz equation with added damping has faster convergence with the GMRES algorithm. As an intermediate step for the shifted laplacian preconditioner, we will illustrate this important property using a Comsol Multiphysics model. We will show the convergence of the GMRES algorithm with geometric multigrid preconditioning for different values of conductivity σ.

The setup is described in subsection 4.10. The frequency is set at 300 MHz. This is the largest frequency considered in this thesis, to allow for the finest mesh and thus the largest amount elements. This setup allows for a computational time in the order of tens of seconds. The error is plotted against the iteration number. The simulation will terminate when a relative tolerance smaller than 0.01 is reached. The convergence of the GMRES algorithm is shown for multiple values of the conductivity σ, which is the only variable changed in between simulations.

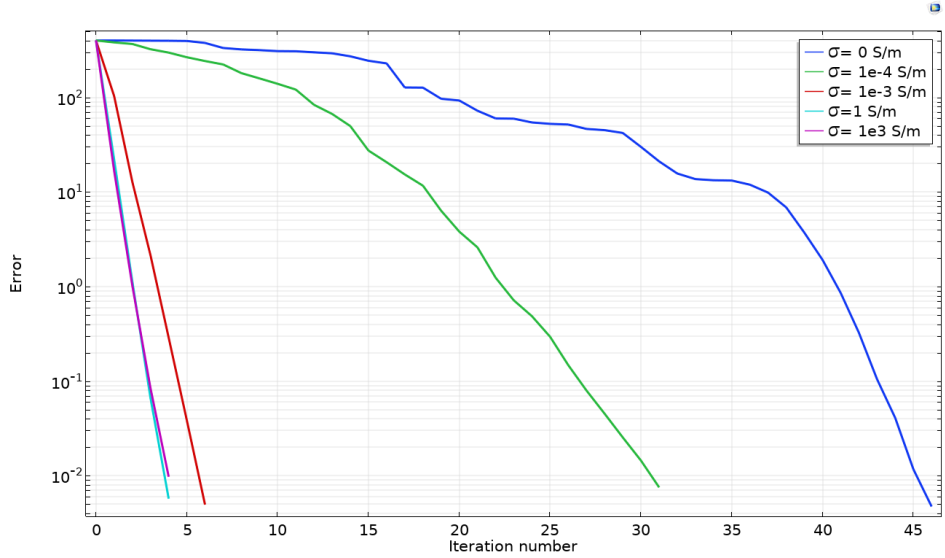

Figure 54: The convergence plot of the GMRES algorithm with geometric multigrid preconditioning for damped Helmholtz problems with different values of the conductivity. The simulation will terminate when a relative tolerance smaller than 0.01 is reached. The convergence is shown for a reverberation room of dimensions (5.03 m $\times$ 3.97 m $\times$ 2.85 m) with the log-periodic dipole array antenna but without the Z-fold mode stirrer. The model considers unit relative permeability and permittivity. The frequency is set at 300 MHz.

This plot shows that the number of iterations needed to reach a relative tolerance smaller than 0.01, is the largest when considering zero-conductivity. This would be the GMRES algorithm solving the Helmholtz problem without damping. The number of iterations needed to reach the set tolerance decreases for increasing conductivity σ. This was expected as the shifted laplacian preconditioning causes the eigenvalues to shift away from the origin where the problem is more oscillatory and thus difficult to compute. Thus the GMRES algorithm with multigrid preconditioning is shown to converge faster for the complex shifted Helmholtz problem. The same amount of iteration steps are needed for a conductivity of 1 S/m as 1000 S/m.

Furthermore, the effect of adding the shifted laplacian preconditioner on the convergence of a non-damped scalar Helmholtz problem is studied. The setup is similar to before and also discussed in subsection 4.10. The setup has a geometry like a reverberation room without Z-fold modestirrer but is now excited via a subwoofer on a wall. The frequency considered is 200 Hz. This was the largest frequency the used working computer could solve the described system for in under one hour.

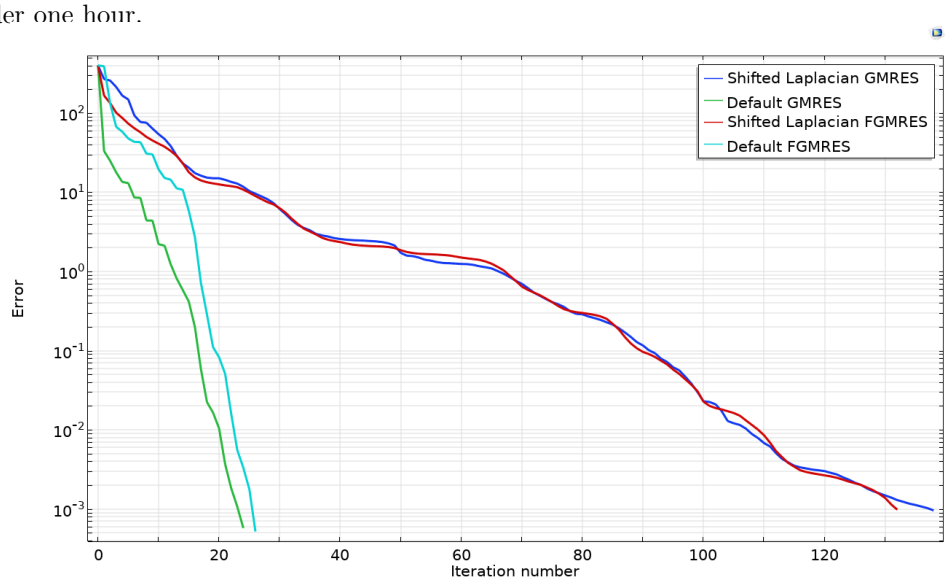

Figure 55: Convergence plots for different solvers of a non-damped pressure acoustic Helmholtz problem at 200 Hz. The problem is excited by a subwoofer with normal acceleration of 1 m/s^2 in the y-direction and is located as shown in figure 21. The domain considers a reverberation room with log-periodic dipole array antenna without Z-fold modestirrer

Figure 55 shows that all solvers with and without shifted laplacian preconditioning reduce the error to 30 rapidly in the first number of iterations. Both the default GMRES and FGMRES with geometric multigrid preconditioning thereafter converge to a tolerance smaller than 0.01 under 30 total iterations. The FGMRES is a more robust version of the GMRES able to switch between preconditioning methods in between different iterations. The GMRES and FGMRES with a shifted laplacian contribution to the multigrid preconditioning have much slower convergence than the default GMRES and FGMRES. The reach a the tolerance in a total of more than 130 iterations. Therefore the shifted laplacian contribution to the multigrid preconditioning was not effective to decrease the number of iterations, so the convergence speed.
Though, the Comsol Multiphysics tutorial about Car Cabin Acoustics, on which this model is based, runs in 10 minutes on a working computer with the added shifted laplacian contribution to the multigrid preconditioning. Without this added shifted laplacian contribution running the model will crash the used working computer, shutting it down. This is probably the effect of a processor that is not strong enough to handle the computation. The Car Cabin Acoustics tutorial model has a more complex geometry and therefore a much denser mesh with more elements. For these complex geometries the added shifted laplacian contribution seems a good and perhaps necessary option that needs to be considered in creating an efficient solver.

6 Discussion

This section will discuss the acquired results and suggest possible reasons for discrepancies found in the comparison between models and measurements. The structure of the discussion will follow the same gradual build up used throughout the thesis. It will start with the antenna models. The antennas are thereafter placed in the empty shielded chambers. The compared electric fields in these chambers will thus be discussed for both antenna models. As an extra step a dielectric object is added to these models to see the effect on the electric field in the chamber. This is added for physical interest and completeness and not as an intermediate step for the final reverberation chamber model. The results of the final reverberation chamber model with incorporated z-fold mode stirrer will be discussed in the end. Throughout the chapter, the models will be distinguished by situation and not by antenna used. The reasoning for this is that the errors in the antennas are discussed in the beginning and may resonate throughout all models that make use of the antennas. Further, since the models build on each other they will have the same possible errors as the model before.

6.1 Antennas

Figures 22 & 23 show the radiation patterns of the 3104c biconical antenna and the 3146a log-periodic dipole array antenna respectively. The biconical antenna shows an omni-directional field pattern. This means that "it radiates equal power in all directions perpendicular to an axis with power varying with angle to the axis" (Wikipedia, 2020). In 3D this is often shown as a donut-shape called a thorus. The model shows the expected field pattern. The log-periodic dipole array antenna is a directional antenna. It radiates more power in a specific direction. Figure 23a shows this behaviour for larger frequencies as the right lobe is bigger than the left lobe. The 2D radiation pattern is similar to that provided by (ETS-Lindgren, 2010). As the log-periodic dipole array antenna is based on the tutorial model created by Comsol Multiphysics, the model is considered to work correctly.

6.2 Shielded chamber with antennas

Even though the antenna models appear to behave as predicted by the theory, there is the possibility that they differ slightly from the workings of the real antennas. This error would resonate from the former models to all models used thereafter. That includes the models discussed now, the shielded chamber models with the respective biconical and log-periodic dipole array antennas.

The modelled electric field does not accurately predict the electric field measured in the shielded chamber at Comtest for low frequencies (< 60 MHz). This is shown in the comparison made at 30 and 60 MHz in figures 25 and 27. The poor prediction can possibly be due to a faulty excitation of the electric field by the biconical antenna. Where the log-periodic dipole array antenna is modelled after an example created by Comsol, the biconical antenna is not. There could be an issue with the excitation using a lumped port for lower frequencies, however the radiation pattern as shown in figure 22 does work as expected by theory.

The model is a simplification of the real chamber which had many more details, like a door, walls connected together and a setup to hold up the antenna and probe. However for low frequencies and thus larger wavelengths these details should be having a smaller effect. Adding more detail to the shielded chamber would increase accuracy at the cost of longer computation time and higher memory usage.

Additionally, the position and direction of the antennas in the measurement setup are not completely the same as the setup discussed in chapter 6. To protect the shielded chamber from scratches, a small plywood floor was placed in the chamber. This layer was neglected as it would neither absorb nor reflect the electromagnetic radiation, but it did influence the height of the antenna. The error was added in the uncertainty of the position measurements, however an error in the height may have a more detrimental effect when the model amplifies this error with a different field. Also the antenna was fixed in a certain position and levelled. Using a level is not very accurate so the setup will have differed slightly from the model.

The shielded chamber does predict the electric field pattern for frequencies above 60 MHz. The differences in amplitude can be explained by the data acquirement procedure. The measured data was normalised to the modelled data, this was done for comparison purposes. Tweaking the model to show the same electric field values as the measurements would be favourable, though time consuming. Changing the perfect electric conducting boundaries to an impedance boundary could also be an explanation for the amplitude differences.

To explain the discrepancies of the wave pattern in the model compared to the measurements for higher frequencies we could fall back to the sensitivity of the model to chamber details. It was found that small changes in the chamber dimensions could hugely change the electric field in the shielded chamber. To check this theory, the model was ran for a chamber with slightly different dimensions.

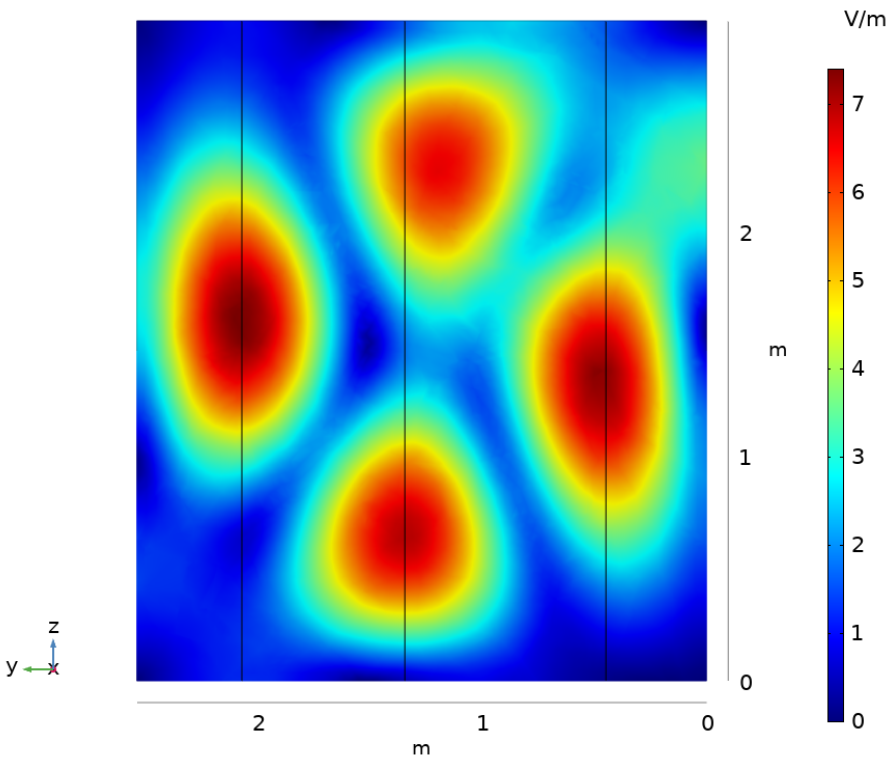

(a)

Figure 56 shows the effect of changing the shielded chamber height from $z = 2.925$ to $z = 2.9$. A height change of 2.5 cm can cause an entirely different electric field. This sensitivity could

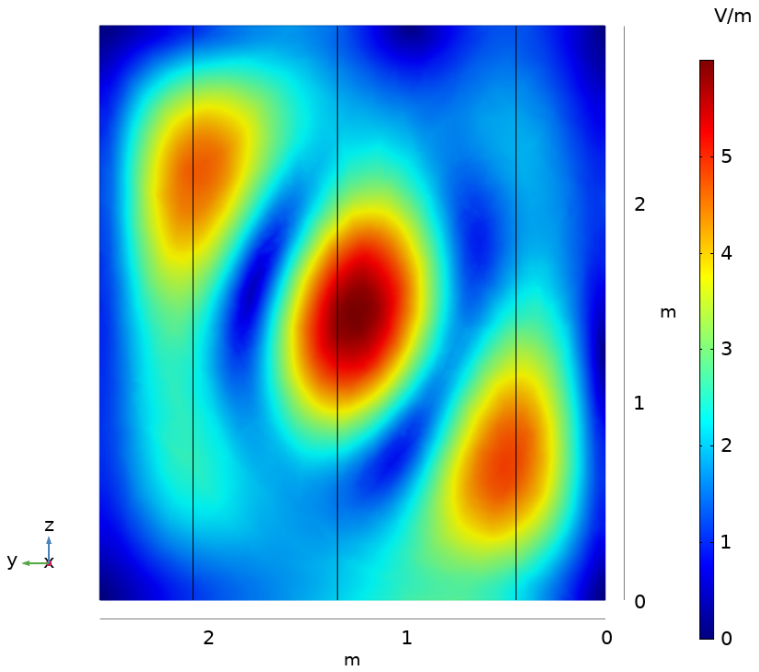

(b)

Figure 56: A comparison of the electric fields for different shielded room heights. Subfigure (a) shows The YZ-plane of the modelled electric field in the shielded chamber at 180 MHz with chamber height $z = 2.925$ m. Subfigure (b) shows The YZ-plane of the modelled electric field in the shielded chamber at 180MHz with chamber height $z = 2.90$ m

offer an explanation for the deviations of the model compared to the real chamber. If a two and a half centimeter difference can change the electric field in its entirety than a couple of millimeters could change the field slightly explaining the small deviations.

6.3 Shielded chamber with antennas and dielectric object

Like explained before, the same errors from earlier models will affect the later models due to the build up process. The current model is the same model as before but with an added dielectric object. The added dielectric object causes more uncertainties in the model.

To start of there will be a difference in the conductivity, permittivity and permeability used in the model and the real constants in nature for water. The constants that were used in the model were extrapolated from data used in (Kaatze, 1989). The extrapolation was done by a Comsol algorithm to the nearest function, in which it follows the same trend before and after the last data points as it does within the data points. This trend will not be the same as in reality and the further away from the nearest data point, the worse the estimation of the constants. As the data is known for relatively high frequencies only, GHz order of magnitude, the lowest frequencies will be expected to have the worst estimation.

The same errors caused in the previous antenna models and empty shielded chamber models are still true for the shielded chamber model with dielectric object. Therefore the excitation of the antennas may still be faulty for low frequencies, simplifications may still have caused the seen deviations, there are still errors due to the measuring setup and the model is still sensitive to dimension deviations. The dimension sensitivity of the model as shown in figure 56 is also found with the added dielectric object, though not everywhere it is as distinct as the field slice in the figure.
The shielded chamber with dielectric object shows that low frequencies, 30 and 60 MHz, are still poorly predicted by the model. This makes us expect that the error lies in the errors named before and not necessarily in the used conductivity, permittivity or permeability constants. Though, these may have added to the amplitude differences observed in figures 45a and 47b which show damping behaviour.

The model does shows the expected difference in behaviour of two dielectric objects. A ferrite tile was modelled which has properties to transmit as much radiation as possible to absorb this radiation inside the object. This is clearly shown as the radiation around the ferrite tile is not affected as much by the tile and the field goes to zero in the middle of the ferrite tile. There is a little reflectivity shown on the right side of figure 50a. A tank with water on the other side has higher reflectivity and lower absorption which is also shown by the model as the radiation is not zero inside the tank of water and there is an higher electric field near the corners of the domain as shown in figure 50b.

6.4 Reverberation chamber

At last we have the pre-characterization numerical model of the reverberation chamber with the incorporated z-fold mode stirrer. The model is an extension of the empty shielded chamber model with antennas with an added z-fold stirrer, so the same errors presented before may play a roll in this model. Thus, chamber dimension sensitivity may have affected the results, just like the uncertainty in the direction and position of the antenna. The reverberation chamber only used a log-periodic dipole array antenna, therefore a faulty excitation by the biconical antenna will not have caused the deviations in the results. Also there was no plywood floor in the reverberation chamber.

The electric field uniformity calculated using the model data did comply with the theory. Field uniformity improved for increasing frequency and the field uniformity was better in a situation with more stirrer rotation positions. The electric field uniformity of the model was worse than the field uniformity of the reverberation chamber at Comtest. The small deviations discussed previously may have caused one of the eight probes to lay in a maximum where it does not in reality. This would have caused the standard deviation to rise and would thereby create a peak in the uniformity plot. As shown in figure 51 the maxima and minima of the electric field are close together. A shift in maxima of 10 cm such as in figure 37b may therefore cause the probe to shift to a maximum or minimum causing spikes in the field uniformity like the spike at 240 MHz for the E_z field in figure 52a.

Changing the perfect electric conducting boundary conditions to impedance boundary conditions of steel at the exterior surfaces was tried to improve field uniformity. The electric field values were slightly lower as expected due to the absorption, however this does not fully explain the difference in field uniformity as shown by the plots below.

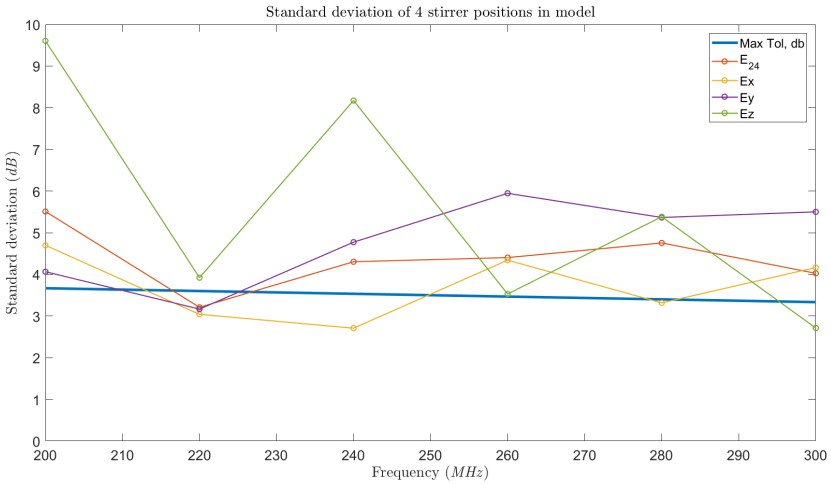

(a)

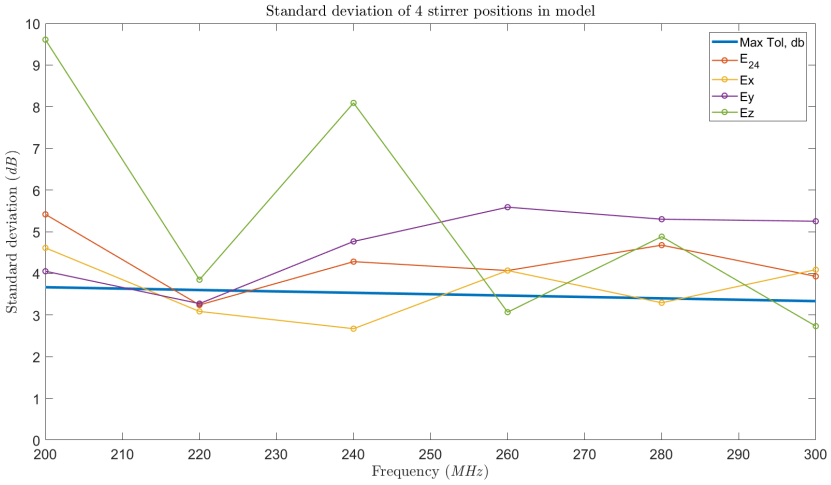

(b)

Figure 57: A comparison of the electric field uniformity in a reverberation chamber with perfect electric conductor boundary conditions and steel impedance boundaries. Subfigure (a) shows the electric field uniformity (dB) for the model using 4 stirrer rotation positions with perfect electric conductor boundary conditions and subfigure (b) shows the electric field uniformity (dB) for the the model with steel boundary surfaces

To better show the effect of changing from PEC boundaries to steel impedance boundaries, the data from figure 57 were used to calculate the error caused by the assumption of PEC boundaries. This error is shown in the plot below.

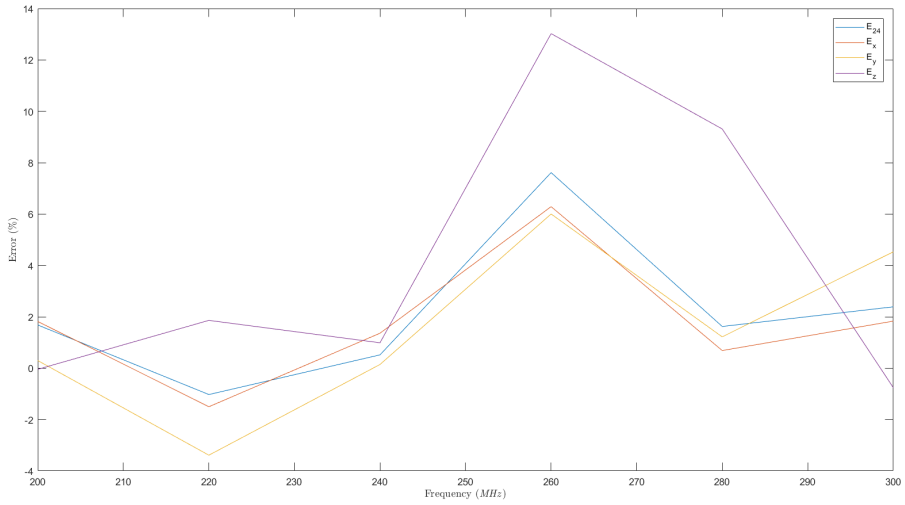

Figure 58: The error (%) of of the field uniformity by changing from perfect electrical conductor to steel impedance boundaries. A positive percentage is a lower field uniformity for steel boundaries compared to the perfect electrical conductor

The transition to steel boundaries changes the electric field with the percentage as shown in figure 58. A positive percentage means a smaller standard deviation so better uniformity. For the z-direction this even leads to a 13% improvement at 260 MHz. Still the standard deviation of the electric field is not as low as the standard deviation of the measurements in the Comtest reverberation chamber. Changing the perfect electric conductor boundaries to impedance boundaries also has an effect on the model with 12 stirrer rotation positions, though in a lesser effect with a maximum difference of 3%.

7 Conclusion

The main topic of this thesis, the comparison of pre-characterization model to measured results, has been discussed in detail in the previous chapters. The physical and mathematical theory was discussed in in chapters 2 and 3 to understand the steps that needed to be taken in the creation of a reliable model. The multiple models used as intermediate steps to create the complex reverberation chamber model are replicas of real life setups created at Comtest, Zoeterwoude. These setups were discussed in the chapter on the implementation together with the comparison procedure. All models and intermediate models were tested on reliability and accuracy. This was also done for the shielded chamber model with the added dielectric object, which was not added as intermediate step but to study the effect of a dielectric object on the electric field inside the chamber. Conclusions for the respective models will use the same development structure as the preceding chapters.

In the beginning stages of the modelling process, both the 3104c biconical antenna (25-200 MHz) and the 3146a LPDA antenna (200-1000 MHz) were found to qualitatively represent an omni-directional and directional antenna respectively. Both models showed radiation patterns with the same form as found in literature.

We then advanced to a more complex model in which the respective antennas were incorporated in a shielded chamber replicated from the shielded chamber with dimensions (4.05 m $\times$ 2.55 m $\times$ 2.925 m). The shielded chamber model was build after the shielded chamber located at Comtest, Zoeterwoude. The electric field calculated by the Comsol model was compared to the measurements in the shielded chamber using the same setup. The comparison is qualitative and not quantitative, so the general waveform is compared and not the electric field magnitudes. The comparison is not done quantitatively because multiple input powers were used in the measurements. Instead the electric field values of the measurements were normalised in such a way that the maximum electric field of the model and the measurements are the same. It was found that the model does not qualitatively predict the electric field in the shielded chamber for frequencies lower than 60 MHz. A possible explanation is a lumped port that does not work correctly at low frequencies. Above 60 MHz, the models predicted the electric field with reasonable certainty. This means that the general wave form with global maxima and minima was predicted, but local maxima and minima predicted by the model were not found in the measurements. These variations may have been caused by sensitivity to detail of the model, like the neglection of detail in the walls, door and probe and antenna setup. Additionally sensitivity to slight deviations in the replication of the measurement setup due to a plywood protection floor and manual levelling of the antenna could explain the errors in the wave form. At last it is shown that a deviation of the shielded chamber dimension of 2.5 cm could lead to a completely different electric field in the model. This shows that the model is sensitive to changes in the geometry.

The same model was made with an added dielectric object for both antennas. The dielectric object was chosen to be a tank of water with dimensions (0.37 m $\times$ 0.565 m $\times$ 0.27 m) for its reflecting properties. This was again compared qualitatively to measurements of the same setup at Comtest. The conclusion that the model does not predict the electric field pattern for frequencies below 60 MHz holds true for this model as well. The same sensitivity to detail and replication deviations of the former shielded chamber model with only the antenna is expected to be the cause of the discrepancy as the model only differ by an added dielectric object. Also the electric field pattern above 90 MHz is modelled with reasonable accuracy similar to the empty shielded chamber. The dielectric object may have brought additional uncertainties to

the model however they were found not to be significant as the qualitative behaviour of the model was similar to the shielded chamber without dielectric object.

Additionally the same model was created using a dielectric object of the same dimensions but with different properties. Instead of a tank of water the properties were used of an absorbing material designed by Comtest, a ferrite tile. The model showed that the tank of water showed higher reflectance than the ferrite tile but lower absorption. This is indeed the behaviour expected from theory.

The model was advanced to resemble the reverberation chamber ($5.03\ \text{m} \times 3.97\ \text{m} \times 2.85\ \text{m}$) with Z-fold stirrer as found at Comtest. To study the accuracy of the model, the field uniformity of the electric field from the model is quantitatively compared to the field uniformity of the electric field measured at Comtest. This field uniformity test was done for both 4 and 12 stirrer rotation positions. Both the measurements and the model showed increasing uniformity for increasing frequency, this is expected as higher frequencies have a more uniform electric field. This was also shown using the model. Additionally the field uniformity increases for increasing amount of stirrer positions this is also expected for standard deviation of a bigger sample size. Field uniformity requirements as specified by IEC 61000-4-21 were not met by the model whereas the Comtest reverberation chamber did comply with the requirements for 12 stirrer rotation positions. A possible explanation for the deviation of field uniformity are shifts in maxima and minima for the model as seen in the shielded chamber. Moreover, changing the PEC boundaries to a more realistic steel wall was observed to improve field uniformity of the 4 stirrer rotation model by up to 13% and the 12 stirrer rotation model by up to 3%.

At last, the shifted laplacian preconditioner was studied. First the effect of an added imaginary shift to the Helmholtz problem on the convergence rate of the GMRES solver with multigrid preconditioner was studied. The study found that the number of iterations to reach a tolerance smaller than 0.01 using this solver setup decreases for increasing values of the conductivity σ. The results are shown for a setup including a reverberation chamber model with log-periodic dipole array antenna but without Z-fold mode stirrer at 300 MHz. The convergence of the GMRES algorithm with multigrid preconditioning is shown to converge faster for increasing imaginary shifts in the Helmholtz equation. This is an important intermediate result in showing the effectiveness of using the imaginary shifted laplacian preconditioner for Helmholtz problems without damping. The faster convergence of the GMRES for a damped Helmholtz problem with increasing conductivity can be used in further research to optimize the shifted laplacian preconditioner for Helmholtz problems with little to no damping. Additionally, the effect of adding a shifted laplacian contribution to the multigrid preconditioning in solving a non-damped pressure acoustic Helmholtz problem was studied. It was that the added shifted laplacian contribution to the multigrid preconditioning increased the number of iterations needed to reach an error tolerance smaller than 0.01. Thus for the used model setup, the contribution made the solver less efficient. However the Comsol tutorial on pressure acoustics in a more complex domain ran efficiently with the shifted laplacian contribution to the multigrid preconditioning. Without the contribution, the used working computer could not solve the problem, probably due to a lack of processing power. This suggests that the shifted laplacian contribution increases solver efficiency only in more complex geometries with more degrees of freedom.

Modelling antennas in a shielded chamber environment using the FEM based Comsol Multiphysics software is observed to be sensitive to small changes in geometry. The current state of the models are shown to qualitatively predict the general wave pattern for frequencies higher

than 90MHz. Frequencies below 60 MHz were not accurately predicted by the model.

A pre-characterization numerical model capable of handling and calculating electric fields withing a rectangular reverberation chamber near its lowest usable frequency was created. The model assuming perfect electric conducting boundaries can only be used as a worst-case scenario model where the field uniformity from measurements cannot be higher than predicted by the model. Adding more detail to the model showed improvement in the accuracy. Future work could therefore consist of developing more accurate antenna models and creating a more detailed reverberation model to improve accuracy of the electromagnetic compatibility results. This can be done using the same gradual build up process as discussed in this thesis to filter out uncertainties before handling the most complex situation with Z-fold mode stirrer. Also, the possibility of using the shifted laplacian preconditioner could be researched to increase efficiency of the solver in more detailed and complex models.

References

Aksun, M. I. (2020). *Introduction to rectangular waveguides.* Engineers heaven. Retrieved from http://kilyos.ee.bilkent.edu.tr/~microwave/programs/magnetic/rect/info.htm

Arnaut, L. R., Serra, R., & West, P. D. (2016, September). Validating reverberation chamber performance based on assessment of field anisotropy. In *2016 international symposium on electromagnetic compatibility - EMC EUROPE* (pp. 205–210). IEEE. Retrieved 2020-07-03, from http://ieeexplore.ieee.org/document/7739171/ doi: 10.1109/EMCEurope.2016.7739171

Ayachour, E. (2003, October). A fast implementation for GMRES method. , *159*(2), 269–283. Retrieved 2020-07-03, from https://linkinghub.elsevier.com/retrieve/pii/S037704270300534X doi: 10.1016/S0377-0427(03)00534-X

Balanis, C. A., & Ioannides, P. I. (2007). Introduction to smart antennas. , *2*(1), 1–175. (Publisher: Morgan & Claypool Publishers)

Barakos, D., & Serra, R. (2017, September). Performance characterization of the oscillating wall stirrer. In *2017 international symposium on electromagnetic compatibility - EMC EUROPE* (pp. 1–4). IEEE. Retrieved 2020-06-16, from http://ieeexplore.ieee.org/document/8094726/ doi: 10.1109/EMCEurope.2017.8094726

Cangellaris, A. C. (1996, August). Frequency-domain finite element methods for electromagnetic field simulation: fundamentals, state of the art, and applications to emi/emc analysis. In *Proceedings of symposium on electromagnetic compatibility* (pp. 107–116).

Comsol. (2017, February). *The Finite Element Method (FEM) .* COMSOL Blog.

Comsol, M. (2020a). *Application gallery.* Comsol.com. Retrieved from Comsol.com/models

Comsol, M. (2020b). *Car cabin acoustics - frequency domain analysis.* Retrieved from https://www.comsol.com/model/car-cabin-acoustics-frequency-domain-analysis-15013

Comsol, M. (2020c, June). *Log-periodic antenna.* Retrieved from https://www.comsol.com/model/log-periodic-antenna-36111

Comsol, M. (2020d). *The multigrid solvers.* COMSOL Documentation.

Comsol, M. (2020e). *Rf module user's guide.* COMSOL Documentation.

Davidson, D. B. (n.d.). COMPUTATIONAL ELECTROMAGNETICS FOR RF AND MICROWAVE ENGINEERING. , 433.

Esmail, M. S. M. (2012). *BAND STRUCTURE OF SOME PHOTONIC CRYSTALS* (phdthesis).

ETS-Lindgren. (2010, March). Emco emc-3146 log periodic antenna [Computer software manual].

ETS-Lindgren. (2019, Augustus). 3104c biconical antenna [Computer software manual].

Frei, W. (2014, October). *How Much Memory Is Needed to Solve Large COMSOL Models?* COMSOL Blog.

Frei, W. (2015, May). *Modeling Metallic Objects in Wave Electromagnetics Problems.* COMSOL Blog.

Frei, W. (2016, February). *Keeping Track of Element Order in Multiphysics Models.* COMSOL Blog.

Gander, M. J., Graham, I. G., & Spence, E. A. (2015, November). Applying GMRES to the helmholtz equation with shifted laplacian preconditioning: what is the largest shift for which wavenumber-independent convergence is guaranteed? , *131*(3), 567–614. Retrieved 2020-07-08, from http://link.springer.com/10.1007/s00211-015-0700-2 doi: 10.1007/s00211-015-0700-2

Griffiths, D. J. (2013). *Introduction to electrodynamics; 4th ed.* Boston, MA: Pearson. (Republished by Cambridge University Press in 2017)

Haberman, R. (2013). *Applied partial differential equations: with fourier series and boundary value problems* (5th ed ed.). PEARSON.

Hill, D. (1994, November). Electronic mode stirring for reverberation chambers. , *36*(4), 294–299. Retrieved 2020-06-16, from http://ieeexplore.ieee.org/document/328858/ doi: 10.1109/15.328858

International Electrotechnical Commission, & Technical Committee 77. (2011). *Electromagnetic compatibility (EMC). compatibilité électromagnétique (CEM). part 4-21, partie 4-21, part 4-21, partie 4-21,*. International Electrotechnical Commission.

Jin, J.-M. (2011). *Theory and computation of electromagnetic fields.* John Wiley & Sons.

Jin, J.-M. (2015). *The finite element method in electromagnetics.* John Wiley & Sons.

Kaatze, U. (1989). Complex permittivity of water as a function of frequency and temperature. *Journal of Chemical and Engineering Data*, *34*(4), 371–374.

Kechroud, R., Soulaimani, A., Saad, Y., & Gowda, S. (2004, May,). Preconditioning techniques for the solution of the helmholtz equation by the finite element method. , *65*(4), 303–321. Retrieved 2020-07-08, from https://linkinghub.elsevier.com/retrieve/pii/S0378475404000199 doi: 10.1016/j.matcom.2004.01.004

Liu, B.-H., Chang, D. C., & Ma, M. T. (1983). Eigenmodes and the composite quality factor of a reverberating chamber. *National Bureau of Standards technical note*(1066).

Logan, D. L. (2012). *A first course in the finite element method* (5th ed ed.). Cengage Learning.

Log-periodic antenna. (n.d.). Retrieved 2020-06-24, from https://www.comsol.com/model/log-periodic-antenna-36111 (Library Catalog: www.comsol.com)

Mittra, R. (2016). *Computational electromagnetics.* Springer.

Nentchev, A. (2008). *Numerical analysis and simulation in microelectronics by vector finite elements.*

Nijenhuis, J. W. (n.d.). Characterization of a comtest 5 × 4 × 3 m3 reverberating chamber. , 6.

Oosterlee, C. W., Vuik, C., Mulder, W. A., & Plessix, R.-E. (2009). Shifted-laplacian preconditioners for heterogeneous helmholtz problems. In B. Koren & K. Vuik (Eds.), *Advanced computational methods in science and engineering* (Vol. 71, pp. 21–46). Springer Berlin Heidelberg. Retrieved 2020-07-08, from http://link.springer.com/10.1007/978-3-642-03344-5_2 (Series Title: Lecture Notes in Computational Science and Engineering) doi: 10.1007/978-3-642-03344-5_2

Orjubin, G., Richalot, E., Mengue, S., & Picon, O. (2006, February). Statistical model of an undermoded reverberation chamber. , *48*(1), 248–251. Retrieved 2020-07-03, from http://ieeexplore.ieee.org/document/1614059/ doi: 10.1109/TEMC.2006.870705

Saad, Y. (1993, March). A flexible inner-outer preconditioned GMRES algorithm. , *14*(2), 461–469. Retrieved 2020-06-23, from http://epubs.siam.org/doi/10.1137/0914028 doi: 10.1137/0914028

Saad, Y. (2003). *Iterative methods for sparse linear systems.* SIAM.

Saleh, M. (2017, February). *Band Structure of Some Photonic Crystals.*

Salon, S., & Chari, M. V. K. (1999). *Numerical methods in electromagnetism.* Elsevier.

SCHWARZBECK. (2020a). Biconical broadband antennas [Computer software manual]. Schönau, Germany.

SCHWARZBECK. (2020b). Log. - per. broadband antenna vuslp 9111 [Computer software manual]. Schönau, Germany.

Serra, R., Marvin, A. C., Moglie, F., Primiani, V. M., Cozza, A., Arnaut, L. R., ... Leferink, F. (2017). Reverberation chambers a la carte: An overview of the different mode-stirring

techniques. , *6*(1), 63–78. Retrieved 2020-06-22, from http://ieeexplore.ieee.org/document/7931986/ doi: 10.1109/MEMC.2017.7931986

Sheikh, A., Lahaye, D., & Vuik, C. (2011). A scalable helmholtz solver combining the shifted laplace preconditioner with multigrid deflation. *Reports of the Department of Applied Mathematical Analysis, 11-01*.

Trottenberg, U., Oosterlee, C. W., & Schuller, A. (2000). *Multigrid*. Elsevier.

Vandekerckhove, S. (n.d.). Simulation of wave propagation problems for automated characterisation of material parameters. , 190.

van Gijzen, M. B., Erlangga, Y. A., & Vuik, C. (2007, January). Spectral analysis of the discrete helmholtz operator preconditioned with a shifted laplacian. , *29*(5), 1942–1958. Retrieved 2020-07-08, from http://epubs.siam.org/doi/10.1137/060661491 doi: 10.1137/060661491

Vijay, R., Jain, R., & Sharma, K. S. (2015). Dielectric properties of water at microwave frequencies. , *3*(3), 3.

Vuik, C., Erlangga, Y. A., & Oosterlee, C. W. (n.d.). Shifted laplace preconditioners for the helmholtz equations. , 8.

Wikipedia. (2020, April). *Omnidirectional antenna.* Wikipedia.org. Retrieved from https://en.wikipedia.org/wiki/Omnidirectional_antenna

Xu, Q., & Huang, Y. (2018). *Anechoic and reverberation chambers: Theory, design, and measurements*. John Wiley & Sons, Ltd. Retrieved 2020-07-03, from http://doi.wiley.com/10.1002/9781119362050 doi: 10.1002/9781119362050

Zhang, H., Krooswyk, S., & Ou, J. (n.d.). *High speed digital design: Design of high speed interconnects and signaling*. Elsevier. (Google-Books-ID: qOlDBAAAQBAJ)

Zhang, K., & Li, D. (2008). *Electromagnetic theory for microwaves and optoelectronics*. Springer Science & Business Media. (Google-Books-ID: UxJPUxYnVqkC)

Zhang, Y.-S., & Chiang, H.-D. (2010, May). Fast newton-FGMRES solver for large-scale power flow study. , *25*(2), 769–776. (Conference Name: IEEE Transactions on Power Systems) doi: 10.1109/TPWRS.2009.2036018

Zhao, H., Shen, Z., & Li, E. (2012-05, May). Hybrid numerical modelling of reverberation chambers. In *2012 asia-pacific symposium on electromagnetic compatibility* (pp. 777–780). IEEE. Retrieved 2020-06-16, from http://ieeexplore.ieee.org/document/6237832/ doi: 10.1109/APEMC.2012.6237832

Appendix

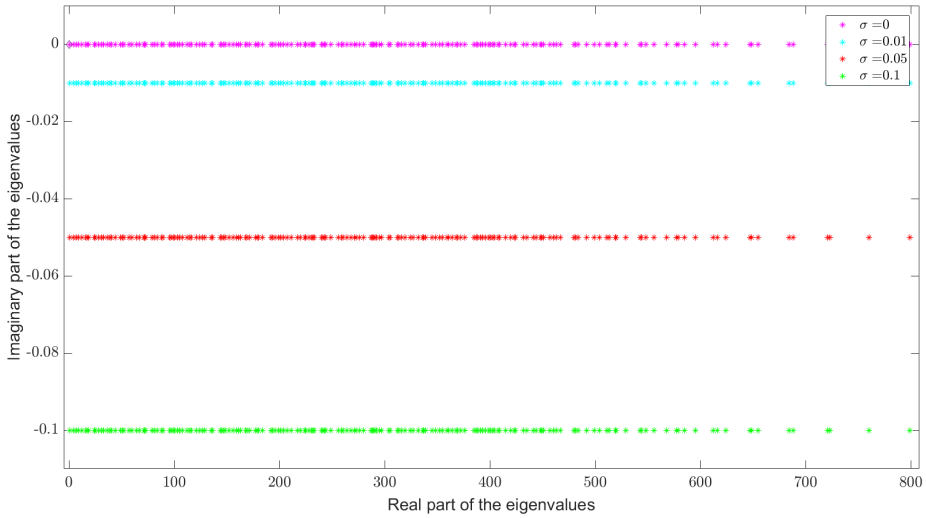

Figure 59: The eigenvalues for the analytic solution of the 2D problem as discussed in subsection 2.8 are plotted in the complex plane. $(a \times b) = (\pi, \pi)$ m and $\epsilon = \mu = \omega = 1$ were chosen for easy plotting. The values of n and m range from 1 to 10. Higher values would show the same trend with increasing real part of the eigenvalue. The plot is created for multiple values of the conductivity σ

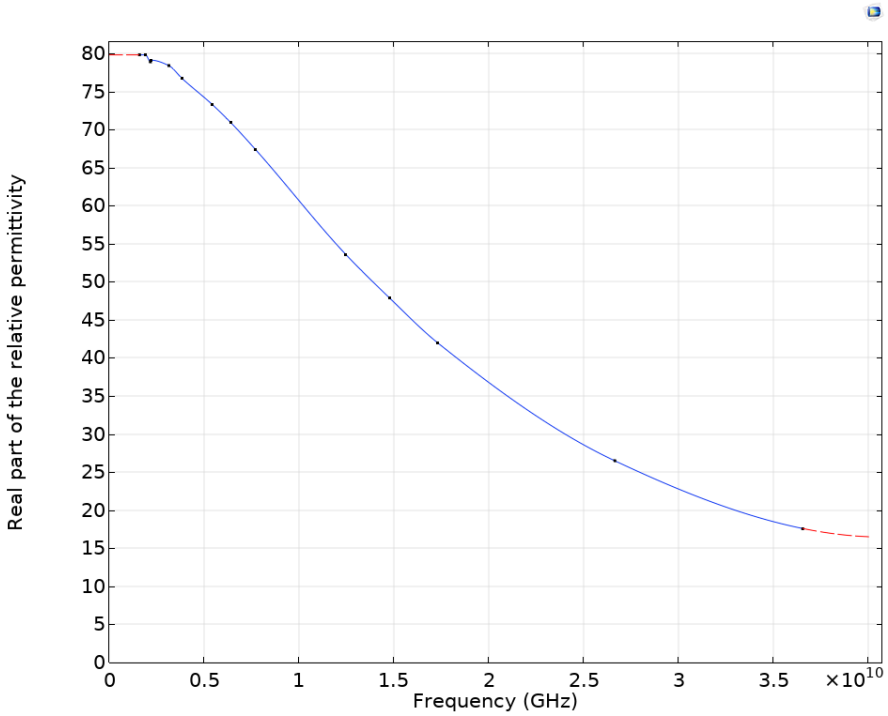

(a)

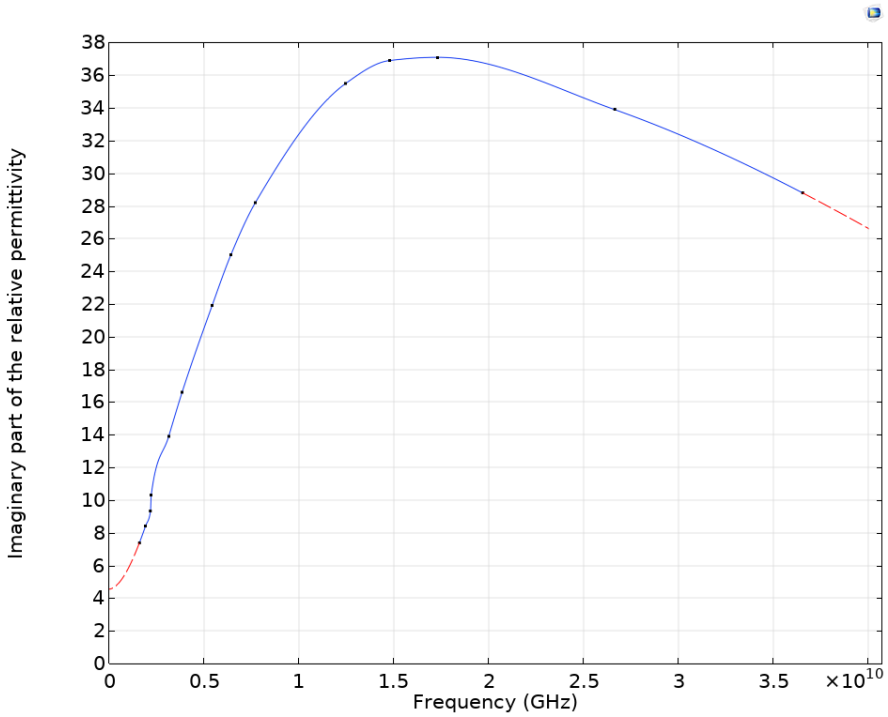

(b)

Figure 60: Plots of the used permittivity of tap water at 20°C. Subfigure (a) shows the real part of the relative permittivity and subfigure (b) shows the imaginary part of the relative permittivity. Both use piecwise cubic interpolation and nearest function extrapolation on data from (Kaatze, 1989)

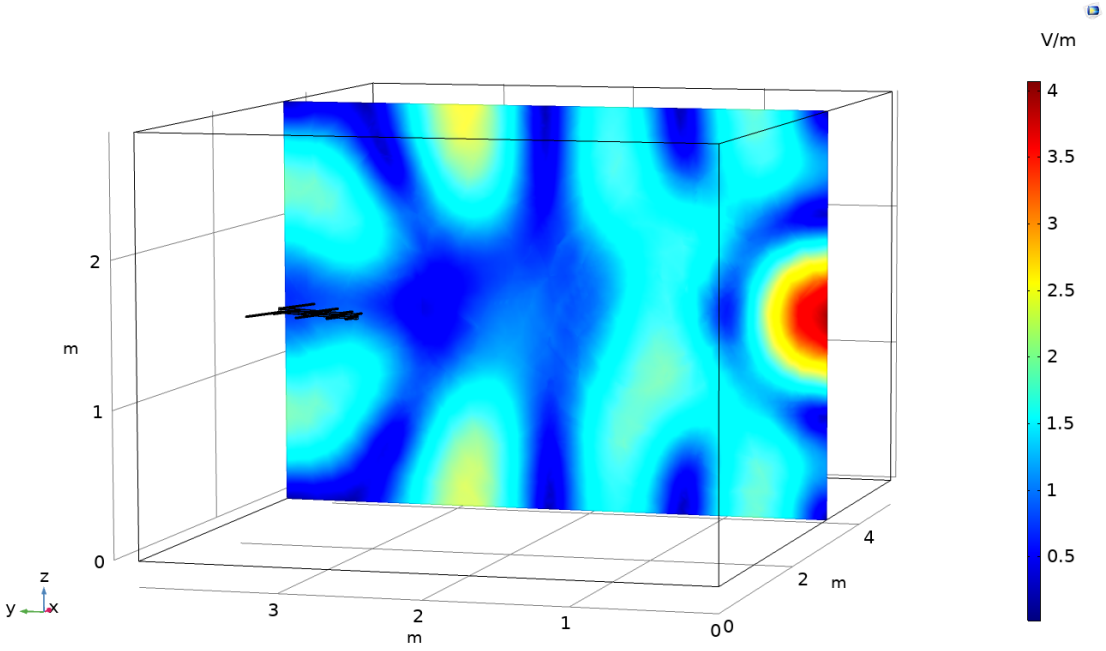

(a)

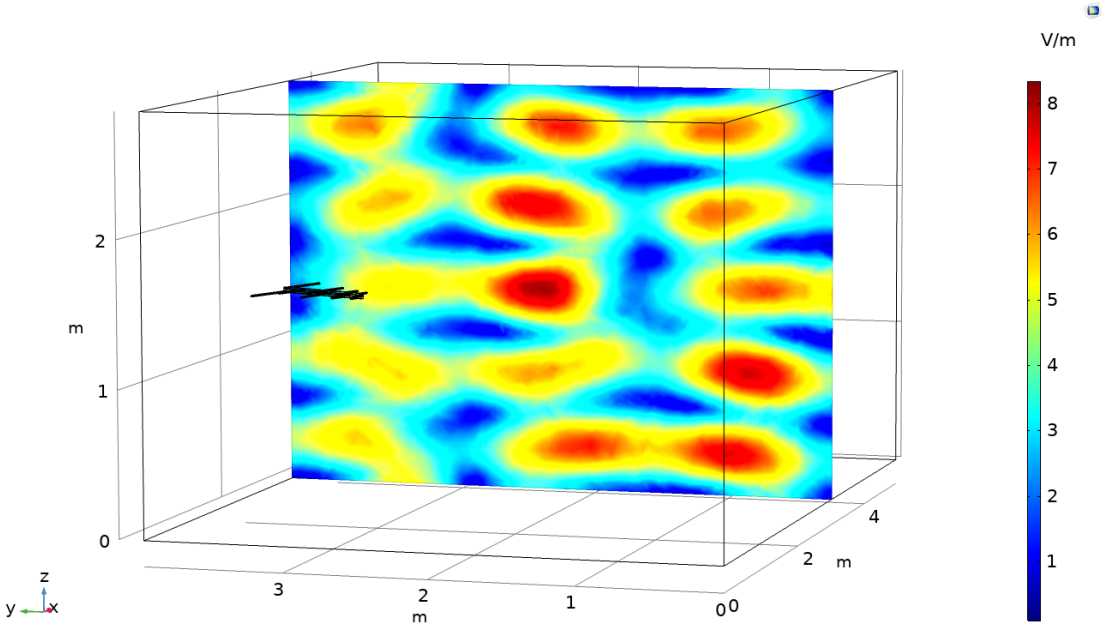

(b)

Figure 61: The electric field plotted at 200 MHz is less uniformly distributed than the electric field at 300 MHz in a reverberation chamber without Z-fold mode stirrer. This is in accordance with the theory. Subfigure (a) shows the electric field plotted in the YZ-plane of the reverberation chamber at 200 MHz. Subfigure (b) shows the electric field plotted in the YZ-plane of the reverberation chamber at 300 MHz